

# REVIEW

of the  
ELECTRICAL COMMUNICATION LABORATORY

NIPPON TELEGRAPH AND TELEPHONE PUBLIC CORPORATION

Former Reports of the Electrical Communication Laboratory  
Nippon Telegraph and Telephone Public Corporation  
from Vol.1, No.1, Sept. 1953 to Vol. 7, No. 12, Dec. 1959

*Published Bimonthly by*

THE ELECTRICAL COMMUNICATION LABORATORY  
NIPPON TELEGRAPH AND TELEPHONE PUBLIC CORPORATION  
1551, Kitizyôzi, Musasino-si, Tôkyô, Japan

VOLUME 8  
NUMBERS 7-8

July-August  
1960



# Review of the Electrical Communication Laboratory

## EDITORIAL COMMITTEE

Susumu OKAMURA *Chairman*

Tadasu FUKAMI	Giichi ITO	Hideo KAWASAKI
Yukio NAKAMURA	Tatsuya SHIMBORI	Takuzo SHINDO
Toyotaro SHIRAMATSU	Takakichi UZAWA	Ginsaku YASAKI
Koji MAEDA	Nobukazu NIIZEKI	Osamu TUKIZI

## EDITORIAL STAFF

Susumu HIRANO *Editor*

Tutomu SAITO *Assistant Editor*

Masao HIROSE //

The Review of the Electrical Communication Laboratory is published six times a year (bi-monthly) by the Electrical Communication Laboratory, Nippon Telegraph Telephone Public Corporation, 1551, Kitizyôzi, Musasino-si, Tôkyô, Japan. Telephone: Tôkyô (391) 2261 and 2271.

All rights of republication, including translation into foreign languages, are reserved by the Electrical Communication Laboratory, NTT.

Subscriptions are accepted at ¥1,200 per year. Single copy ¥300 each. Foreign postage is ¥300 per year or ¥50 per copy. Remittance should be made in check payable to the Electrical Communication Laboratory and mail to the Director.



# R E V I E W

## of the ELECTRICAL COMMUNICATION LABORATORY

NIPPON TELEGRAPH AND TELEPHONE PUBLIC CORPORATION

Volume 8, Numbers 7-8

July-August 1960

U.D.C. 621.318.56.001

# Analysis of Polar Relay

Yasuo TOMITA†

*The motional equations of a polar relay have been developed from the appropriate assumptions, and the coefficients of these equations have been determined from the measurement of the constants of resonant frequency, stability factor, force factor, inductance, etc. by applying the same method as that used for electroacoustic transducers. The performance; for example, the operating time of the relay, agrees well with the values calculated from the theoretical equations.*

## Introduction

In a paper published in 1958, the fundamental motional equations of ordinary relays were derived from Lagrange-Maxwell's equation, and several coefficients of the equations were expressed by such measurable constants as stability factor, force factor at the point of neutrally balance, resonant frequency of the vibrating member, the time constant of the circuit and etc. The experimental data for these ordinary relays agreed fairly well with the calculated values.

In the present research, polar relays were analyzed and satisfactory results were obtained, even though the analyses were made for the conditions that the magnetic pull was linear and the effects of eddy current were negligible.

## 1. Motional Equations

Fig. 1 shows a model of the structure of a polar relay, and Fig. 2 its equivalent circuits.

Fig. 2 (b) is the simplified version of Fig. 2 (a), and the main gap fluxes of these two circuits are equal. The fundamental motional equations are obtained from Fig. 2 (b) by the application of Lagrange-Maxwell's equation. That is:

$$\frac{u_0}{u_0 - u^2} \cdot \frac{di}{d\theta} + \frac{2uu_0i}{(u_0 - u^2)^2} \cdot \frac{du}{d\theta}$$

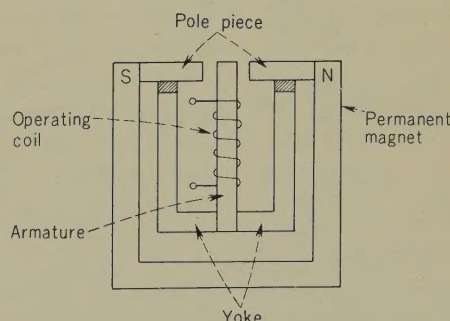
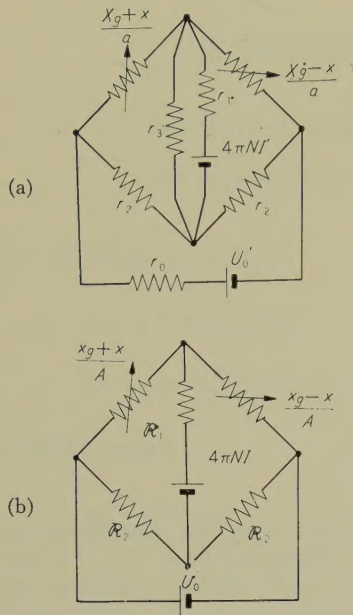


**Fig. 1—Model structure of polar relay.**

† Station Apparatus Research Section.



$r_0$ : Equivalent reluctance of the permanent magnet.  
 $r_1$ : Equivalent reluctance of the armature.  
 $r_2$ : Equivalent reluctance of the yoke.  
 $r_3$ : Equivalent leakage reluctance.  
 $X_g$ : Main gap length.  
 $x$ : Travel (newtral point=0).  
 $a$ : Effective pole face area.  
 $U_0'$ : Equivalent m.m.f. of the permanent magnet.  
 $4\pi NI'$ : m.m.f. of the operating coil.

$$\begin{aligned}
 A &= a, \quad U_0 = \frac{2r_2}{r_0 + 2r_2} U_0', \quad I = \frac{r_3}{r_1 + r_3} I', \\
 R_1 &= \frac{r_2}{2} + \frac{r_1 r_3}{r_1 + r_3} - \frac{r_0 r_2}{2(r_0 + 2r_2)} - \frac{1}{4} (r_0 + 2r_2)(r_1 + r_3), \\
 R_2 &= \frac{1}{2} (r_1 + r_3)(r_0 + 2r_2), \quad x_g = X_g + \frac{\sigma r_0 r_2}{r_0 + 2r_2}.
 \end{aligned}$$

Fig. 2—Equivalent circuit.

$$+ \frac{u_g + u^2}{(u_g - u^2)^2} \sigma' \frac{du}{d\theta} + \beta i - 1 = 0 \quad (1)$$

$$\begin{aligned}
 \frac{d^2 u}{d\theta^2} + 2\delta_0 \frac{du}{d\theta} + u &= \frac{1}{(u_g - u^2)^2} \\
 &\times \{ \Delta \beta^2 u i^2 + \Delta' (u_g + u^2) \beta i + \Delta'' u \} \quad (2)
 \end{aligned}$$

where

$$\begin{aligned}
 u &= \frac{x}{A(2\mathfrak{R}_1 + \mathfrak{R}_2) + x_g}, \quad \beta = \frac{R}{(L_1)_0 \omega_0}, \\
 I &= \frac{Ei}{(L_1)_0 \omega_0}, \quad \delta_0 = \frac{r}{2m\omega_0}, \quad \omega_0^2 = \frac{s}{m}, \\
 \theta &= \omega_0 t, \quad I_s = \frac{E}{R},
 \end{aligned}$$

$$\sigma = \frac{U_0 NA}{A(2\mathfrak{R}_1 + \mathfrak{R}_2) + x_g} = \frac{E}{\omega_0} \sigma',$$

$$\Delta = \frac{A(8\pi N)^2 u_g I_s^2}{s8\pi \{A(2\mathfrak{R}_1 + \mathfrak{R}_2) + x_g\}^3},$$

$$\Delta' = \frac{A8\pi N I_s U_0}{s8\pi \{A(2\mathfrak{R}_1 + \mathfrak{R}_2) + x_g\}^3},$$

$$\Delta'' = \frac{A U_0^2}{s8\pi \{A(2\mathfrak{R}_1 + \mathfrak{R}_2) + x_g\}^3},$$

$R$ : d.c. resistance of circuit

$(L_1)_0$ : inductance related to main gap flux only

$\omega_0$ : angular resonant frequency

$E$ : applied voltage

$r$ : damping resistance

$s$ : effective stiffness

$m$ : effective mass.

Even though the motional characteristics of the armature are obtained from Equations (1) and (2), a precise analysis is so difficult that it is better to develop these equations by  $u$  or  $\theta$  series as follows:

$$p = \sum_{n=0}^{\infty} A_n u^{n/3}, \quad i = \sum_{n=0}^{\infty} B_n u^{n/3}$$

where  $p = du/d\theta$ .

When these expressions are substituted into Equations (1) and (2),

$$\begin{aligned}
 P &= \sqrt[3]{\frac{9\Delta'\beta}{2u_g}} u^{2/3} - \frac{1}{2} (\beta + 2\delta_0) u \\
 &+ \frac{1}{20\sqrt[3]{9\Delta'\beta}} \left( \frac{11}{4} \beta^2 - 7\beta\alpha_0 + 11\delta_0^2 \right) u^{4/3} \\
 &+ \frac{1}{60\sqrt[3]{81\Delta'^2\beta^2}} \left( 18\delta_0 + 4\delta_0^3 + 6\beta\delta_0^2 - 9\beta \right. \\
 &\left. - \frac{17}{4} \beta^3 - 4\beta^2\delta_0 + \frac{18}{u_g^2} \Delta'' \beta \right) u^{5/3} + \dots \quad (4)
 \end{aligned}$$

$$\begin{aligned}
 i &= \sqrt[3]{\frac{6u_g}{\Delta'\beta}} u^{1/3} + \sqrt[3]{\frac{9u_g^2}{2\Delta'^2\beta^2}} \left( \frac{1}{3} \delta_0 + \frac{5}{6} \beta \right) u^{2/3} \\
 &+ \frac{\mu_g}{10\Delta'\beta} \left( \delta_0^2 + \frac{21}{4} \beta^2 - 7\beta\delta_0 \right. \\
 &\left. - \frac{9\Delta'\sigma'\beta + \Delta''}{u_g^2} + 10 \right) u
 \end{aligned}$$



$$\begin{aligned}
& + \frac{u_g}{\Delta' \beta^3 \sqrt{\frac{9\Delta' \beta}{2u_g}}} \left( 252\delta_0 - 126\beta - \frac{469}{4}\beta^3 \right. \\
& - 10\delta_0^3 + \frac{129}{2}\delta_0\beta^2 - 105\beta\delta_0^2 + \frac{189}{u_g^2}\beta^2\Delta'\sigma' \\
& + \frac{54}{u_g^2}\Delta'\sigma'\beta\delta_0 + \frac{252\Delta''\beta - 54\Delta''\delta_0}{u_g^2} \left. \right) u^{4/3} \\
& + \dots \dots \dots
\end{aligned} \quad (5)$$

from

$$\begin{aligned}
\theta &= \int p^{-1} du, \\
\theta &= \frac{3}{\sqrt[3]{\frac{9\Delta'\beta}{2u_g}}} u^{1/3} + \frac{3}{4} \cdot \frac{(\beta + 2\delta_0)}{\sqrt[3]{\left(\frac{9\Delta'\beta}{2u_g}\right)^2}} u^{2/3} \\
&+ \frac{1}{20\sqrt[3]{\left(\frac{9\Delta'\beta}{2u_g}\right)^3}} \left( \frac{9}{4}\beta^2 + 27\beta\delta_0 + 9\delta_0^2 \right) u \\
&+ \frac{1}{80\sqrt[3]{\left(\frac{9\Delta'\beta}{2u_g}\right)^4}} \left( 9\beta + \frac{17}{2}\beta^2\delta_0 + 23\beta\delta_0^2 \right. \\
&\left. - 18\delta_0 - 4\beta^3 - 70\delta_0^3 - \frac{18}{u_g^2}\Delta''\beta \right) u^{4/3} + \dots \dots \dots
\end{aligned} \quad (6)$$

when developed into a  $\theta$  series,

$$\begin{aligned}
u &= \Delta'\beta \left[ \frac{\theta^3}{6u_g} - \frac{\theta^4}{12u_g} \left( \frac{\beta}{2} + \delta_0 \right) + \left\{ \frac{1}{20u_g^2} \left( \frac{\Delta'u_g}{6} \beta^3 \right. \right. \right. \\
&\left. \left. - \frac{\Delta'^2\beta^2\sigma'}{6u_g} + \frac{\Delta'\Delta''\beta}{6u_g} \right) + \frac{\Delta'\beta\delta_0}{30u_g} \left( \frac{\beta}{2} + \delta_0 \right) \right. \\
&\left. \left. - \frac{\Delta'\beta}{120u_g} \right\} \theta^5 + \dots \dots \dots \right] \\
i &= \theta - \frac{\beta}{2} \theta^2 + \left( \frac{\beta^2}{6} - \frac{\Delta'\sigma'\beta}{6u_g^2} \right) \theta^3 + \frac{1}{12u_g} \left( \frac{\Delta'\sigma'\beta^2}{u_g} \right. \\
&\left. + \frac{\Delta'\alpha'\beta\delta_0}{u_g} - \frac{\beta^3u_g}{2} \right) \theta^4 + \dots \dots \dots
\end{aligned} \quad (7)$$

where Equations (7) are effective only when  $\theta < 1$ .

## 2. Relations between Constants

The constants of the magnetic circuit of relay are determined by the following procedure. At first, the expressions of force factor  $\Phi$  stability factor  $\mu$  and inductance  $L$  at the neutral point (where  $u=0$ ) are:

$$\begin{aligned}
(L_1)_0 &= \frac{8\pi N^2 A}{A(2\Re_1 + \Re_2) + x_g} \\
&= \frac{8\pi N^2 a}{a \left( r_2 + \frac{2r_1 r_3}{r_1 + r_3} \right) + X_g} = \frac{4\pi N^2}{\Re} \quad (8)
\end{aligned}$$

$$\Phi = \frac{NU_0 A}{\{A(2\Re_1 + \Re_2) + x_g\}^2 u_g} \quad (9)$$

$$\frac{1}{\mu_0} = \frac{AU_0^2}{s8\pi \{A(2\Re_1 + \Re_2) + x_g\}^3 u_g^2} \quad (10)$$

where  $4\pi NI_m \ll U_0$

and suffix 0 means the neutral point, while  $I_m$  means the small A.C. current used at the time of measurement.

The inductance actually measured is:

$$(L_0)_0 = \frac{4\pi N^2}{r_1 + \frac{r_3(r_2 + X_g/a)}{2r_3 + r_2 + X_g/a}} = \frac{4\pi N^2}{\Re'} \quad (11)$$

Secondary, each constant of the magnetic circuit is arranged as follows:

$$\frac{1}{\Phi_0^2 \mu_0} = \frac{1}{8\pi N^2 s} \left( r_2 + \frac{2r_1 r_3}{r_1 + r_3} \right) + \frac{X_g}{8\pi N^2 a s} \quad (12)$$

The relation between  $1/\Phi_0^2 \mu_0$  and  $X_g$  is linear, and the effective pole face area "a" can be computed if the values of "s" and "N" are known. (See Fig. 3) In the same way, from Equations (9) and (10)

$$\Phi_0 \mu_0 = \frac{8\pi N s}{U_0} \cdot \frac{ar_0 r_2}{r_0 + 2r_2} + \frac{8\pi N s}{U_0} X_g \quad (13)$$

Therefore the effective m.m.f. of the permanent magnet  $U_0$  is obtained from the slope of Fig. 4. The following function can be obtained from the intercept of the same graph. (See Fig. 4)

$$\frac{r_0 r_2}{r_0 + 2r_2}. \quad (14)$$

By measuring  $(L_0)_0$

$$\Re' = r_1 + \frac{r_3(r_2 + X_g/a)}{2r_3 + r_2 + X_g/a}.$$

Then if  $X_{gc}$  is the central reference value of  $X_g$ , and  $\Re'(X_{gc})$  the corresponding value of  $\Re'(X_g)$ , the expression  $\Re'(X_g) - \Re'(X_{gc})$  may be rewritten in the following form: (See Fig. 5)

$$\frac{X_g - X_{gc}}{\Re'(X_g) - \Re'(X_{gc})} = \frac{a(2r_3 + r_2 + X_{gc}/a)(2r_3 + r_2)}{2r_3^2} + \frac{2r_3 + r_2 + X_{gc}/a}{2r_3^2} X_{gc}. \quad (15)$$

From the ratio of the slope of this graph to the intercept, the next value is obtained.

$$r_2 + 2r_3 \quad (16)$$

and the second term which indicates the slope in the right side of Equation (15) is: (See Fig. 6)

$$y_1 = \frac{2r_3 + r_2}{2r_3^2} + \frac{X_{gc}}{2r_3^2 a} \quad (17)$$

From the slope of Equation (17) the value of  $r_3$  is determined. In the same way, by using the reciprocals  $\rho'(X_g)$  and  $\rho'(X_{gc})$  instead of  $\Re'(X_g)$  and  $\Re'(X_{gc})$ ,

$$\frac{X_{gc} - X_g}{\rho'(X_g) - \rho'(X_{gc})} = \frac{\{r_1(2r_3 + r_2) + r_2 r_3\} \{ar_1(2r_3 + r_2) + ar_2 r_3 + (r_1 + r_3)X_{gc}\}}{2ar_3^2} + \frac{(r_1 + r_3) \{ar_1(2r_3 + r_2) + ar_2 r_3 + (r_1 + r_3)X_{gc}\}}{2ar_3^2} X_{gc}. \quad (18)$$

The slope of Equation (18) is expressed as follows: (See Fig. 7)

$$y_2 = \frac{(r_1 + r_3) \{r_1(2r_3 + r_2) + r_2 r_3\}}{2r_3^2} + \frac{(r_1 + r_3)^2}{2ar_3^2} X_{gc}. \quad (19)$$

From the slope of Equation (19) the following values is obtained:

$$\frac{r_1 + r_3}{r_3}. \quad (20)$$

Thus the values of  $r_0$ ,  $r_1$ ,  $r_2$ ,  $r_3$ ,  $U_0$ , and " $a$ " are obtained from Equations (12) (13), (14), (16), (17), and (20).

### 3. Experimental Method

i) Measurement of effective mass " $m$ ," effective stiffness " $s$ " and resonant frequency " $f_0$ ." These constants are obtained from the change of resonant frequency, which is obtained by the additional mass method. (See Fig. 8)

$$\frac{1}{\omega_0'^2} = \frac{1}{s} (m + m') \quad (21)$$

where

$\omega_0'$ : resonant angular frequency

$m'$ : additional mass.

ii) Measurement of stability factor  $\mu_0$  (See Fig. 9)

From the change of resonant frequency, stability factor  $\mu_0$  can be obtained.

$$\mu_0 = \frac{f_0^2}{f_0'^2 - f_0'^2}. \quad (22)$$

iii) Measurement of force factor  $\Phi_0$ . (See Fig. 9)

Force factor  $\Phi_0$  can be obtained from the measurement of the motional impedance circle. That is;

$$D = \Phi_0^2 / r' \quad (23)$$

$$r' = 2\pi m(f_2 - f_1) \quad (24)$$



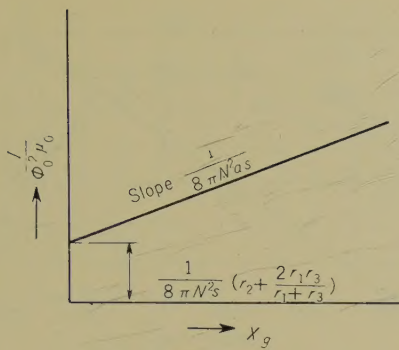


Fig. 3—Relations between  $X_g$  and  $1/\Phi_0^2\mu_0$ .

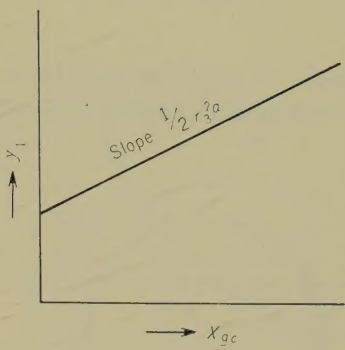


Fig. 6—Relations between  $X_{gc}$  and  $y_1$ .

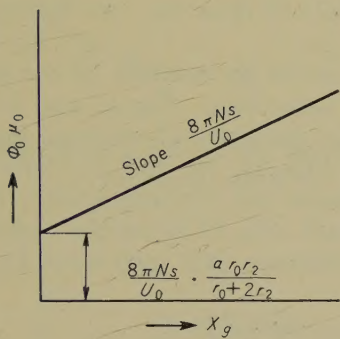


Fig. 4—Relations between  $X_g$  and  $\Phi_0\mu_0$ .

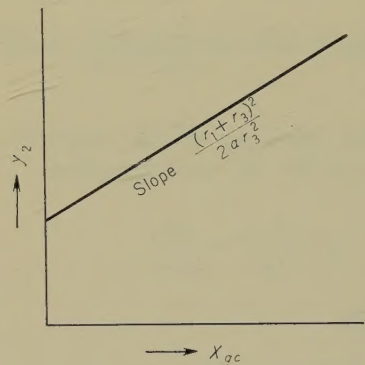


Fig. 7—Relations between  $X_{gc}$  and  $y_2$ .

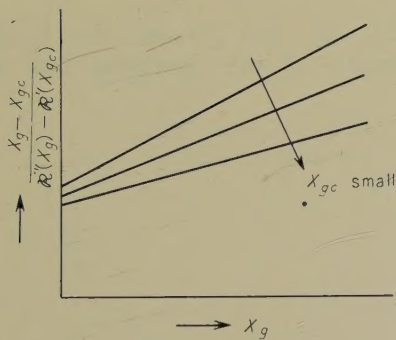


Fig. 5—Relations between  $X_g$  and  $(X_g - X_{gc}) / \{R'(X_g) - R'(X_{gc})\}$ .

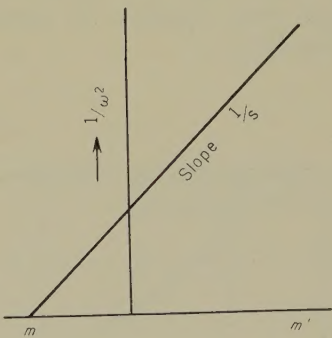


Fig. 8—Measurement of  $s$  and  $m$ .

$$\Phi_0 = \sqrt{2\pi m(f_2 - f_1)D} \quad (25)$$

where

$D$ : diameter of motional impedance circle  
 $r'$ : electromagnetic damping resistance.

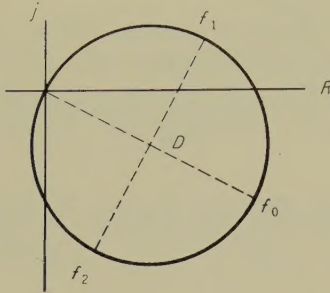


Fig. 9—Motional impedance circle.

And the efficiency of the magnetic circuit is expressed by the next equation.

$$\eta = \frac{(L_1)_0}{(L_0)_0} = \frac{\mu_0 \Phi_0^2}{s(L_0)_0} \quad (26)$$

### Results

The actual measurements were carried out for 450 types of polar relays. Fig. 10 shows the results of the additional mass method. The measurements were made under the conditions where only an armature and a discriminator were applied. At present time  $N=10^4$ , therefore,

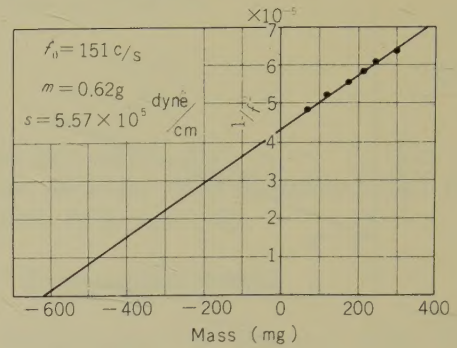


Fig. 10—Measurement values of the armature constant.

$$s = 5.57 \times 10^5 \text{ dyne/cm}, \quad m = 0.62 \text{ gr.}$$

Fig. 11 shows an example of the measured values of inductance. Fig. 12 and 13 show, respectively, examples of motional impedance circles. In Figs. 14, 15, and 16 force factor, stability factor and electromagnetic damping are illustrated. Fig. 17 shows the experimental result of Equation (12), and from its slope;

$$a = 0.213 \text{ cm}^2.$$

In the same way, the following results are obtained by the examination of Figs. 18–22. (See Table 1)

Fig. 23 shows the efficiency of the magnetic circuit.

Figs. 24, 25, and 26 are the results of measurements of the operating time of the

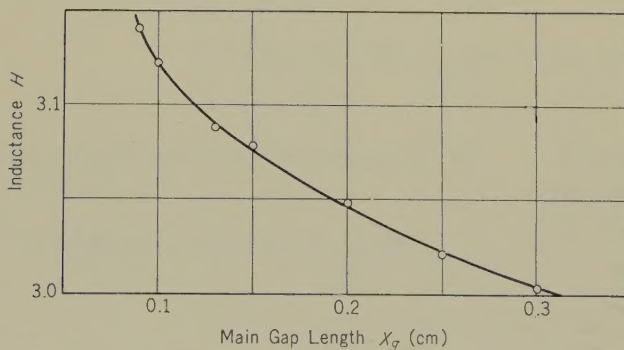


Fig. 11—Measurement values of inductance (at 1000 c/s).



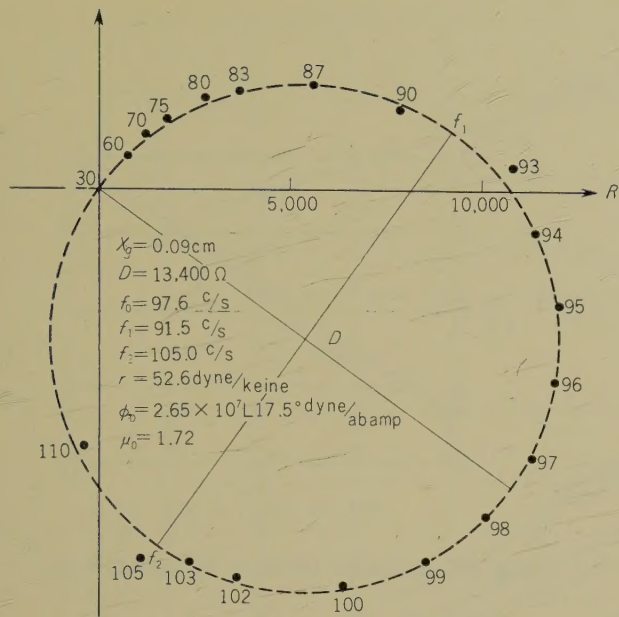


Fig. 12—Example of the motional impedance circle (1).

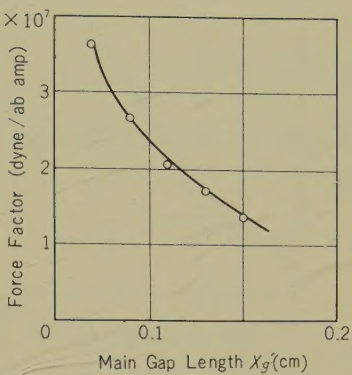


Fig. 14—Measurement values of the force factor.

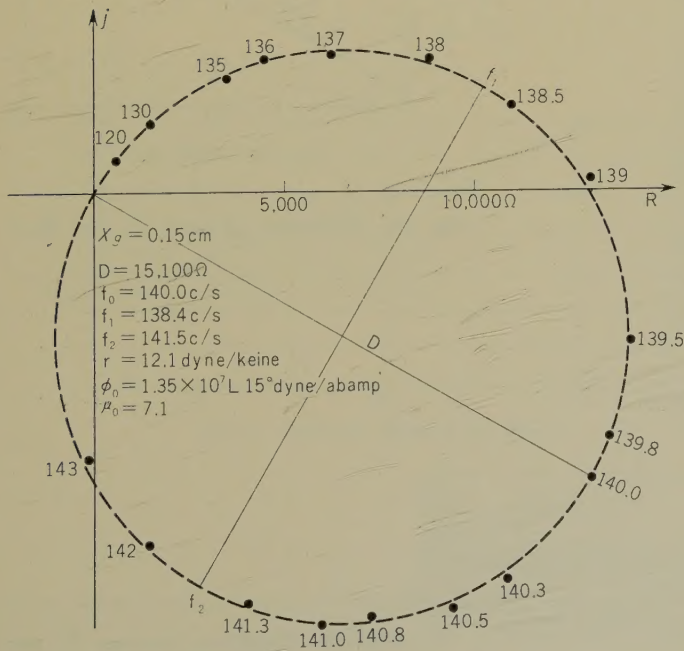


Fig. 13—Example of the motional impedance circle (2).

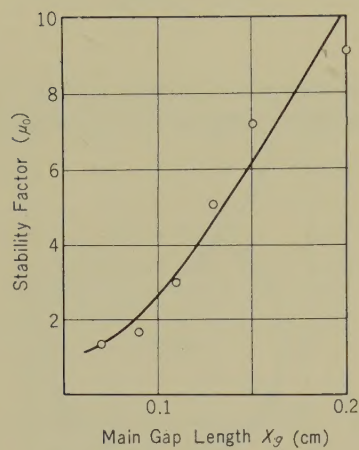


Fig. 15—Measurement values of the stability factor.

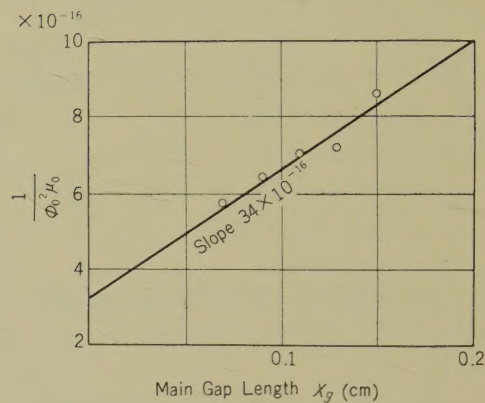


Fig. 17—Relations between  $X_g$  and  $1/\Phi_0^2 \mu_0$ .

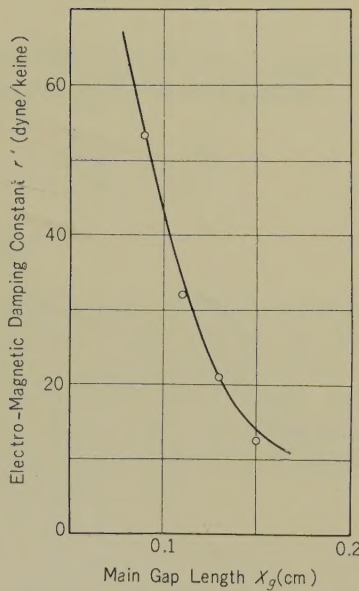


Fig. 16—Relations between  $X_g$  and  $r'$ .

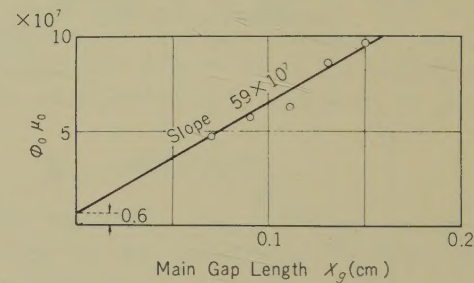


Fig. 18—Relations between  $X_g$  and  $\Phi_0 \mu_0$ .

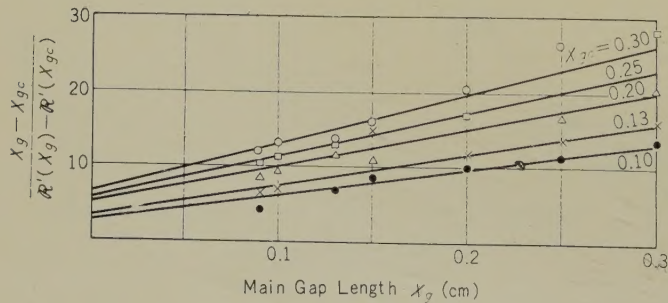


Fig. 19—Relations between  $X_g$  and  $(X_g - X_{gc}) / \{\Re'(X_g) - \Re'(X_{gc})\}$ .



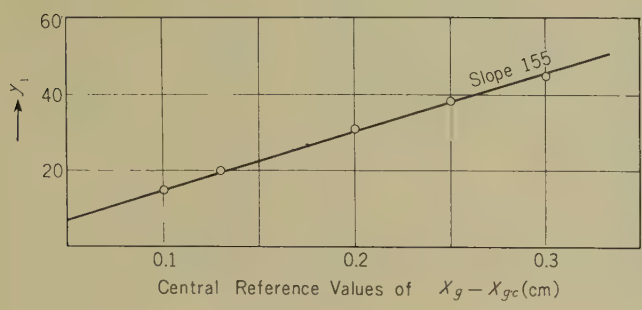


Fig. 20—Relations between  $X_{gc}$  and  $y_1$ .

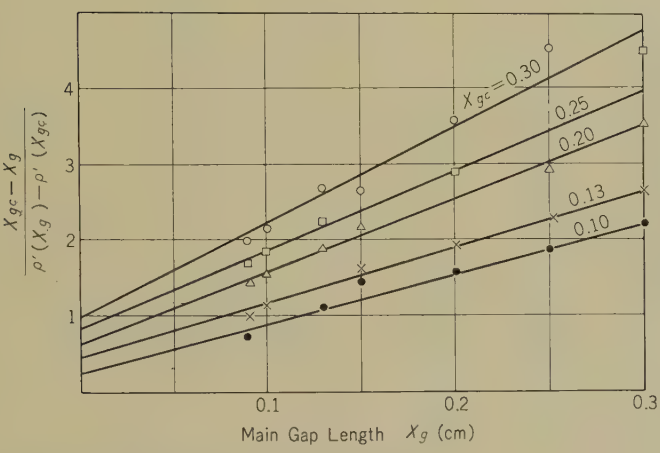


Fig. 21—Relations between  $X_g$  and  $(X_{gc} - X_g) / \{\rho'(X_g) - \rho'(X_{gc})\}$ .

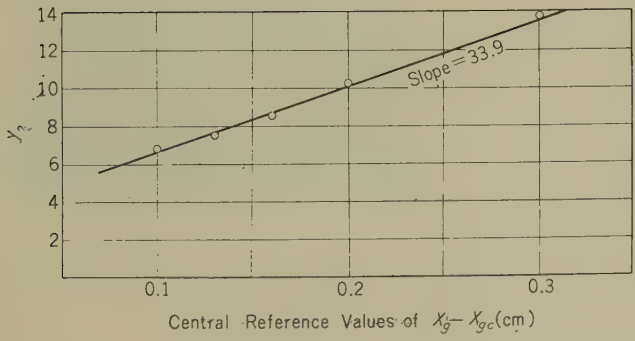


Fig. 22—Relations between  $X_{gc}$  and  $y_2$ .

Table 1

MEASUREMENT RESULTS

	$a$ (cm <sup>2</sup> )	$U_0/4\pi$ (A)	$U_0'/4\pi$ (A)	$r_0$ (cm <sup>-1</sup> )	$r_1$ (cm <sup>-1</sup> )	$r_2$ (cm <sup>-1</sup> )	$r_3$ (cm <sup>-1</sup> )
Result	0. 213	18. 6	24. 27	0. 123	0. 344	0. 204	0. 123

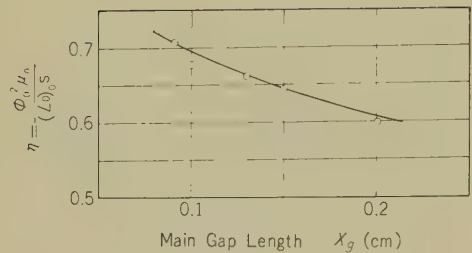


Fig. 23—Efficiency of the magnetic circuit.

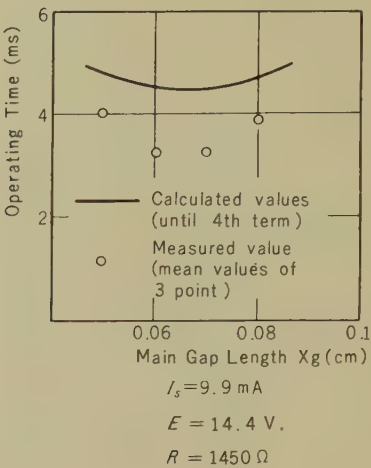


Fig. 26—Relations between gap length and operating time.

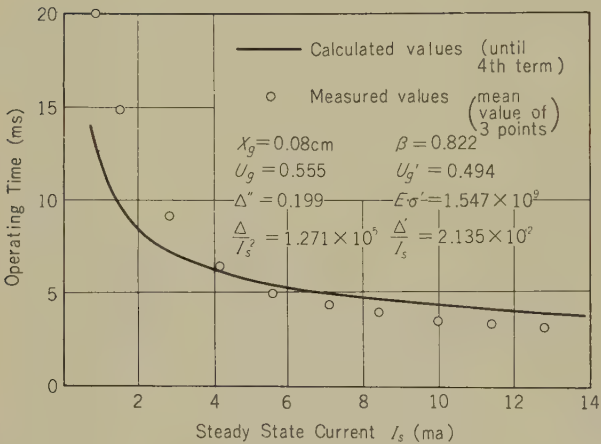


Fig. 24—Relations between current and operating time.

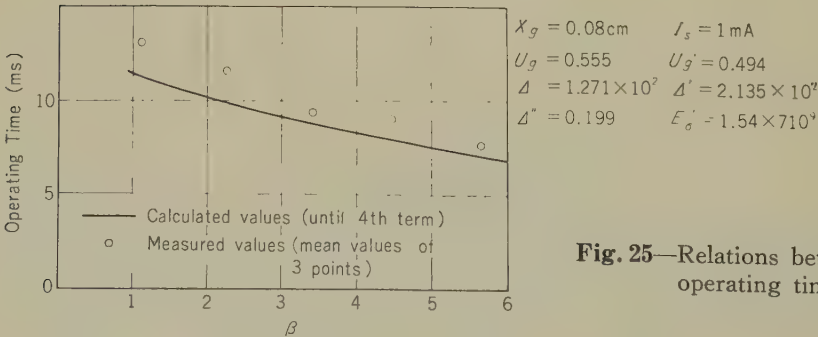
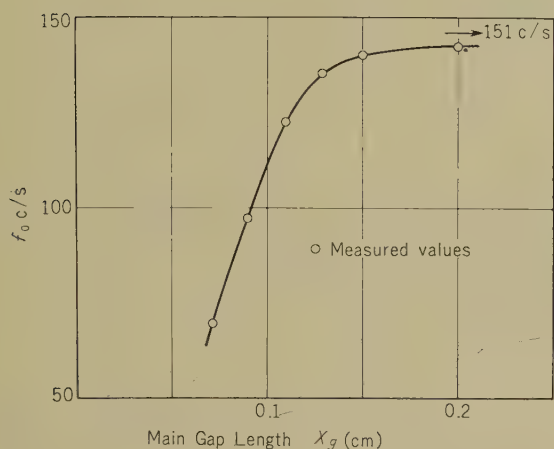


Fig. 25—Relations between  $\beta$  and operating time.

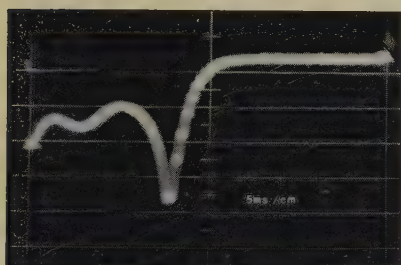


relays, and the calculated values are obtained from Equation (6), though  $\delta_0$  is omitted here.

Fig. 27 shows the change of resonant frequency, and Figs. 28-31 are photographs showing coil current.

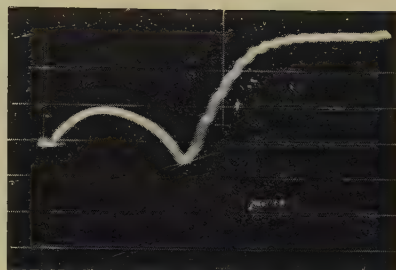


**Fig. 27**—Relations between main gap length and resonant frequency.



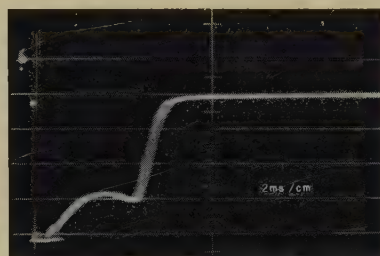
$E=2\text{ V}$   $I_s=1.4\text{ mA}$

**Fig. 28**—Coil current example 1.



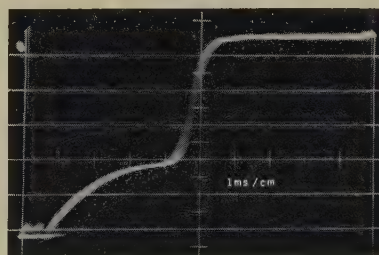
$E=4\text{ V}$   $I_s=2.8\text{ mA}$

**Fig. 29**—Coil current example 2.



$E=10\text{ V}$   $I_s=7.05\text{ mA}$

**Fig. 30**—Coil current example 3.



$E=14\text{ V}$   $I_s=10\text{ mA}$

**Fig. 31**—Coil current example 4.

## Conclusion

The method presented in this paper is also useful in the analysis of the operation of ordinary relays.

The measured operating and release time agree with the calculated values. It is concluded that force factor and stability factor, which have not been taken into consideration

in general analysis of relay operation, should be considered.

## Acknowledgement

The author is deeply grateful for helpful advice given by Dr. Hayasaka and Dr. Masuzawa who suggested him the present study.

**References**

- (1) Y. Tomita, "The Analysis of the Motional Characteristics of Relays," *Electr. Comm. Labor. Tech. Jouru.*, N.T.T., **7**, 3/4, p. 189, 1958:
- (2) K. Masuzawa and Y. Tomita, "Motional Equations of the Vibrating Parts of Electromagnetic Relays," *Journ. Inst. Electr. Comm. Engns. Japan*, **3**, 33, p. 244, 1958.

\* \* \* \*



# Dielectric-Coated Waveguide Construction and Characteristics\*

Ken'ichi NODA and Kazuo YAMAGUCHI†

*Techniques for applying linings to protect tubes, vessels etc. against chemical agents have been modified so as to be suitable for coating the inner surfaces of waveguides with polyethylene.*

*In addition, a new technique, the tube bonding method, has been developed. At present, use of this technique gives the best surface smoothness and also the best thickness uniformity.*

*The attenuation constant of waveguides made by this method increases approximately 20% at 50 Gigacycles per second when the waveguides are bent with a radius of 30 meters.*

*The attenuation increased due to the bonding material layer is theoretically calculated.*

## Introduction

It is well known that the  $TE_{01}$  mode in a circular waveguide is suitable for low-loss transmission, but on the other hand very strict tolerances are required of the dimensions and in the installation of the waveguide to obtain a low loss value near the theoretical value. Moreover, the mode conversion from the  $TE_{01}$  mode to the  $TM_{11}$  mode is serious problem to be overcome at bends. The function of the dielectric layer is to prevent the mode conversion from the  $TE_{01}$  to the  $TM_{11}$  at bends by removing the degeneration of the propagation constants between both modes.<sup>(1)</sup> By the choice of suitable thickness of the dielectric layer and suitable bending radius,  $TE_{01}$  power can be transmitted along the waveguide with only little attenuation increase over that of a straight guide. It is essentially very difficult to bond low loss dielectrics to a metal such as copper. Conventional techniques for lining acid-proof tubes are used for the construction of the

dielectric-coated waveguide. Six methods including conventional lining techniques have been developed. The flame spray method which is used to manufacture acid-proof vessels is very excellent method from the viewpoint of strong adhesive force, but it has the defect of increasing the dielectric loss. Dipping in dispersed solution, used for the same purpose, gives some difficulty in practical manufacturing processes. Moreover, the surface is too hard to be finished smoothly by this method. The whirl sinter method which is used for the polyethylene coating of electric wire is suitable only when the waveguide is short. By this method strong adhesive force is obtainable. The power dropping method, which is a modification of the whirl sinter method, can be used even for long waveguides. The tube bonding method is excellent from the viewpoint of good uniformity of the thickness in the axial direction. It is possible to bond polyethylene to the inner wall of the waveguide through the use of 'Hydropol,' made by Phillips Petroleum Company in the U.S.A. for the purpose of bonding polyethylene to brass in submarine cable repeaters. The above mentioned dispersed solution can also be used as a binding material.

Polytetrafluoroethylene or polystyrene is also

\* MS in Japanese received by the Electrical Communication Laboratory, April 18, 1960. Originally published in the *Kenkyū Zituyōka Hokoku (Electr. Comm. Labor. Techn. Journ.)*, NTT, Vol. 9, No. 6, p. 621, 1960.

Hyper-frequency Research Section.

a low loss material, but it is very difficult to coat metals with this material in the proper thickness.

Transmission loss due to the losses in the dielectric and the bonding material layers has been calculated theoretically. Dielectric constants of the materials used for the dielectric-coated waveguide have been measured. Transmission experiments of the  $TE_{01}$  mode through dielectric-coated curved waveguide manufactured by the tube bonding method have shown that this type of waveguide was promising for bends.

## 1. Problem of the Design of Dielectric-Coated Waveguides

### 1.1. Dielectric Losses

The transmission loss of a waveguide increases when the dielectric layer is bonded to its inner wall and increases still further when the waveguide is bent. The main causes of the attenuation increase are as follows:

- (1) Loss in the dielectric,
- (2) Mode pattern of electric and magnetic fields being changed by the dielectric layer,
- (3) Mode conversion at bends,
- (4) Increase of  $TE_{01}$  normal mode loss at bends.

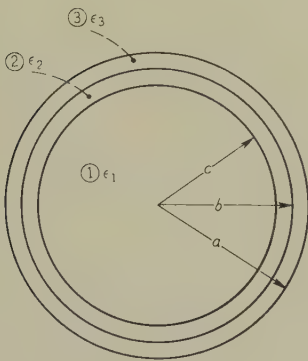


Fig. 1—Dielectric-coated waveguide with bonding agent layer.

Fig. 1 shows the cross sectional view of a waveguide with polyethylene and bonding material layers. In the practical case, although the layer thickness of the bonding material is very thin, it can not be neglected from the point of attenuation increase since the dielectric loss is very large compared with that of polyethylene. The thicknesses of two layers are assumed very thin compared with the radius of the waveguide.

Electromagnetic fields in waveguides containing inhomogeneous dielectrics inside represented by two scalar functions are as follows:

$$\left. \begin{aligned} E_t(u, v, z) &= \sum_i V_i(z) \mathbf{e}_{ti}(u, v), \\ H_t(u, v, z) &= \sum_i I_i(z) \mathbf{h}_{ti}(u, v), \\ E_z(u, v, z) &= \sum_i I_i(z) e_{zi}(u, v) \\ &= \sum_i I_i(z) \frac{\nabla_t \cdot \mathbf{h}_{ti} \times \mathbf{i}_z}{i\omega\epsilon}, \\ H_z(u, v, z) &= \sum_i V_i(z) h_{zi}(u, v) \\ &= \sum_i V_i(z) \frac{\nabla_t \cdot \mathbf{i}_z \times \mathbf{e}_{ti}}{i\omega\mu}, \end{aligned} \right\} \quad (1)$$

where

$$\left. \begin{aligned} \mathbf{e}_{ti}(u, v) &= \nabla_t T_i(u, v) \\ &+ \frac{\mu(u, v)}{\mu_0} \nabla_t T_i'(u, v) \times \mathbf{i}_z, \\ \mathbf{h}_{ti}(u, v) &= -\frac{\epsilon(u, v)}{\epsilon_0} \nabla_t T_i(u, v) \times \mathbf{i}_z \\ &+ \frac{h_i^2}{k_0^2} \nabla_t T_i'(u, v). \end{aligned} \right\} \quad (2)$$

$T_i$  and  $T_i'$  satisfy the following partial differential equations in each region:

$$\left. \begin{aligned} \nabla_i^2 T_i &= -\chi_{\lambda i}^2 T_i, \\ \nabla_i^2 T_i' &= -\chi_{\lambda i}^2 T_i', \end{aligned} \right\} \quad (3)$$

where  $\lambda$  denotes the respective region, one, two or three, and  $i$  represents the mode number which is usually denoted by the



double sign  $nm$ . The axial components of the fields are

$$\begin{aligned} e_{zi} &= i \frac{\chi_{1i}^2}{\omega \varepsilon_0} T_i, \\ h_{zi} &= i \frac{\chi_{1i}^2}{\omega \mu_0} T_i. \end{aligned} \quad (4)$$

If we use cylindrical coordinates  $(r, \varphi, z)$ ,  $T_i$  and  $T_i'$  are expressed in the following form.

$$T_i = \begin{cases} p_i J_n(\chi_{1i} r) \frac{\sin n\varphi}{\cos n\varphi}, & \text{in region ①} \\ p_i' \frac{\chi_{1i}^2}{\chi_{2i}^2} J_n(\chi_{1i} c) \left\{ J_n(\chi_{2i} r) - A N_n(\chi_{2i} r) \right\} \frac{\sin n\varphi}{\cos n\varphi}, & \text{in region ②} \\ p_i' \frac{\chi_{1i}^2}{\chi_{3i}^2} J_n(\chi_{1i} c) \left\{ J_n(\chi_{2i} b) - A N_n(\chi_{2i} b) \right\} \frac{N_n(\chi_{3i} a) J_n(\chi_{3i} r) - J_n(\chi_{3i} a) N_n(\chi_{3i} r)}{N_n(\chi_{3i} a) J_n(\chi_{3i} b) - J_n(\chi_{3i} a) N_n(\chi_{3i} b)} \frac{\sin n\varphi}{\cos n\varphi}, & \text{in region ③} \end{cases} \quad (5)$$

$$T_i' = \begin{cases} q_i J_n(\chi_{1i} r) \frac{\cos n\varphi}{-\sin n\varphi}, & \text{in region ①} \\ q_i' \frac{\chi_{1i}^2}{\chi_{2i}^2} J_n(\chi_{1i} c) \left\{ J_n(\chi_{2i} r) - B N_n(\chi_{2i} r) \right\} \frac{\cos n\varphi}{-\sin n\varphi}, & \text{in region ②} \\ q_i' \frac{\chi_{1i}^2}{\chi_{3i}^2} J_n(\chi_{1i} c) \left\{ J_n(\chi_{2i} b) - B N_n(\chi_{2i} b) \right\} \frac{N_n'(\chi_{3i} a) J_n(\chi_{3i} r) - J_n'(\chi_{3i} a) N_n(\chi_{3i} r)}{N_n'(\chi_{3i} a) J_n(\chi_{3i} b) - J_n'(\chi_{3i} a) N_n(\chi_{3i} b)} \frac{\cos n\varphi}{-\sin n\varphi}, & \text{in region ③} \end{cases} \quad (6)$$

where  $a$ ,  $b$ , and  $c$  are the radii shown in Fig. 1. Equations (5) and (6) satisfy the continuity condition of  $E_z$  and  $H_z$  at  $r=b$  and the boundary condition  $E_z = E_\varphi = 0$  at  $r=a$ . Moreover, if we put

$$\begin{aligned} p_i' &= \frac{p_i}{J_n(\chi_{2i} c) - A N_n(\chi_{2i} c)}, \\ q_i' &= \frac{q_i}{J_n(\chi_{2i} c) - B N_n(\chi_{2i} c)}, \end{aligned} \quad (7)$$

then, the continuity conditions of  $E_z$  and  $H_z$  at  $r=c$  are fulfilled. The characteristic equation from which the propagation constant should be determined is obtained from the continuity conditions of  $E_\varphi$  and  $H_\varphi$  at  $r=b$  and  $r=c$ , and also from (7). If we put

$$\frac{a-b}{a} = \delta_1, \quad \frac{b-c}{a} = \delta_2, \quad \delta_1 + \delta_2 = \delta, \quad (8)$$

the conditions  $\delta_1 \ll 1$  and  $\delta_2 \ll 1$  are satisfied in the practical case. Then the Bessel functions in the characteristic equation are expanded in a power series of  $\delta \chi a$ , and only the lowest order term is calculated. The mode, which is reduced to TE or TM mode when  $\delta_1$  and  $\delta_2$  are both reduced to zero, is called simply the TE or the TM mode although this is not

exact. In the case of the TM mode, we have used the following definition:

$$\chi_{1i} = \frac{k_i}{a} + \Delta \chi_i, \quad (9)$$

where  $J_n(k_i) = 0$ . Then, we can expand as

$$J_n(c \chi_{1i}) \doteq (\Delta \chi_i a - k_i \delta) J_n'(k_i). \quad (10)$$

The solution of the characteristic equation is

$$\Delta \chi_i = \frac{k_i}{a} \delta - \frac{\varepsilon_1}{\varepsilon_2} \frac{\chi_{2i}^2}{\chi_{1i}} \delta_2 - \frac{\varepsilon_1}{\varepsilon_3} \frac{\chi_{3i}^2}{\chi_{1i}} \delta_1. \quad (11)$$

For the  $TE_{nm}$  modes with  $n \neq 0$ , using (9) and  $J_n'(k_i) = 0$ , we can expand as

$$J_n'(c\chi_{1i}) \doteq -(\Delta\chi_i a - k_i \delta) \frac{k_i^2 - n^2}{k_i^2} J_n(k_i). \quad (12)$$

Then, we obtain

$$\Delta\chi_i = -\frac{n^2}{k_i(k_i^2 - n^2)} \frac{1}{a} \left\{ \frac{\varepsilon_1}{\varepsilon_2} (\chi_2^2 a^2 - k_i^2) \delta_2 + \frac{\varepsilon_1}{\varepsilon_3} (\chi_3^2 a^2 - k_i^2) \delta_1 \right\}. \quad (13)$$

For the  $TE_{0m}$  mode,

$$\Delta\chi_i = -\frac{k_{[0m]}}{3} \frac{1}{a} \{ \chi_2^2 a^2 \delta_2^3 + \chi_3^2 a^2 \delta_1^3 + 3\chi_2^2 a^2 (\delta_1^2 \delta_2 + \delta_1 \delta_2^2) - k_{[0m]}^2 \delta^3 \}. \quad (14)$$

$\alpha_D$  and  $\Delta\beta$  in following equations are the real and imaginary parts of the perturbation terms of the propagation constant  $\gamma$ .  $\varepsilon$  is represented as  $\varepsilon' - i\varepsilon''$  in each region, where  $\varepsilon' \gg \varepsilon''$  is assumed. Moreover,  $\varepsilon_1$  is assumed lossless. For the TM modes,

$$\frac{\Delta\beta}{\beta_i} = \frac{\varepsilon_2' - \varepsilon_1}{\varepsilon_2'} \delta_2 + \frac{\varepsilon_3' - \varepsilon_1}{\varepsilon_3'} \delta_1, \quad (15)$$

$$\frac{\alpha_D}{\beta_i} = \varepsilon_1 \left( \frac{\varepsilon_2''}{\varepsilon_2'^2} \delta_2 + \frac{\varepsilon_3''}{\varepsilon_3'^2} \delta_1 \right).$$

For the  $TE_{nm}$  modes with  $n \neq 0$

$$\frac{\Delta\beta}{\beta_i} = \frac{n^2}{k_i^2 - n^2} \frac{1}{1 - \nu_i^2} \left( \frac{\varepsilon_2' - \varepsilon_1}{\varepsilon_2'} \delta_2 + \frac{\varepsilon_3' - \varepsilon_1}{\varepsilon_3'} \delta_1 \right), \quad (16)$$

$$\frac{\alpha_D}{\beta_i} = \frac{n^2}{k_i^2 - n^2} \frac{1}{1 - \nu_i^2} \varepsilon_1 \left( \frac{\varepsilon_2''}{\varepsilon_2'^2} \delta_2 + \frac{\varepsilon_3''}{\varepsilon_3'^2} \delta_1 \right).$$

For the  $TE_{0m}$  modes,

$$\frac{\Delta\beta}{\beta_{[0m]}} = \frac{k_{[0m]}^2}{3} \frac{1}{1 - \nu_{[0m]}^2} \left\{ \frac{\varepsilon_2' - \varepsilon_1}{\varepsilon_1} (\delta_1 - \delta_1)^3 + \frac{\varepsilon_3' - \varepsilon_1}{\varepsilon_1} \delta_1^3 \right\}, \quad (17)$$

$$\frac{\alpha_D}{\beta_{[0m]}} = \frac{k_{[0m]}^2}{3} \frac{1}{1 - \nu_{[0m]}^2} \left\{ \frac{\varepsilon_2''}{\varepsilon_1} (\delta - \delta_1)^3 + \frac{\varepsilon_3''}{\varepsilon_1} \delta_1^3 \right\}.$$

In (15), (16), and (17)  $\nu = \lambda/\lambda_c$ , where  $\lambda_c$  is the cutoff wavelength of the waveguide without the dielectric layer. For the  $TE_{nm}$  with  $n \neq 0$  and TM, the attenuation constants increase in proportion to

$$\frac{\varepsilon_2''}{\varepsilon_2'^2} \delta_2 + \frac{\varepsilon_3''}{\varepsilon_3'^2} \delta_1, \quad (18)$$

then, if  $\varepsilon_2' = \varepsilon_3'$ , for example, bonding material of only one percent of the thickness of the polyethylene layer gives the same attenuation increase as that of the polyethylene, assuming that the bonding layer has one hundred times the  $\tan \delta$  of polyethylene. On the other hand, in case of the  $TE_{0m}$  mode the attenuation increase is very small.

Recently a waveguide with double layers has been calculated by Unger<sup>(2)</sup> for utilization as a mode filter. In a straight waveguide, bonding material having high loss is desirable because it gives mode filter action, but in a curved waveguide it is unfavorable because it makes the  $TE_{01}$  normal mode loss large. When  $\delta_2 = 0$ , equations (16) and (17) reduce to the perturbations of a single dielectric layer shown by Unger,<sup>(1)</sup> namely

$$\frac{\Delta\beta}{\beta_{(nm)}} = \frac{\varepsilon' - 1}{\varepsilon'} \delta, \quad \text{TM}$$

$$\frac{\alpha_D}{\beta_{(nm)}} = \frac{\varepsilon''}{\varepsilon'^2} \delta,$$

$$\frac{\Delta\beta}{\beta_{[nm]}} = \frac{n^2}{k_{[nm]}^2 - n^2} \frac{\varepsilon' - 1}{\varepsilon' (1 - \nu_{[nm]}^2)} \delta, \quad \text{TE}_{nm}$$

$$\frac{\alpha_D}{\beta_{[nm]}} = \frac{n^2}{k_{[nm]}^2 - n^2} \frac{\varepsilon''}{\varepsilon'^2 (1 - \nu_{[nm]}^2)} \delta, \quad n \neq 0$$

$$\frac{\Delta\beta}{\beta_{[0m]}} = \frac{k_{[0m]}^2}{3} \frac{\varepsilon''}{1 - \nu_{[0m]}^2} \delta^3, \quad \text{TE}_{0m}$$

$$\frac{\alpha_D}{\beta_{[0m]}} = \frac{k_{[0m]}^2}{3} \frac{\varepsilon''}{1 - \nu_{[0m]}^2} \delta^2.$$

Unfortunately, (19) is not a good approximation unless  $\delta$  is very small compared with one, but it has been used for rough estimation of the losses for simplicity.  $\alpha_D$  for the



TE<sub>01</sub> mode is shown in Fig. 2 when the waveguide diameter is 51 mm, the dielectric constant is 2.37, and  $\tan \delta$  is  $2.01 \times 10^{-4}$ .

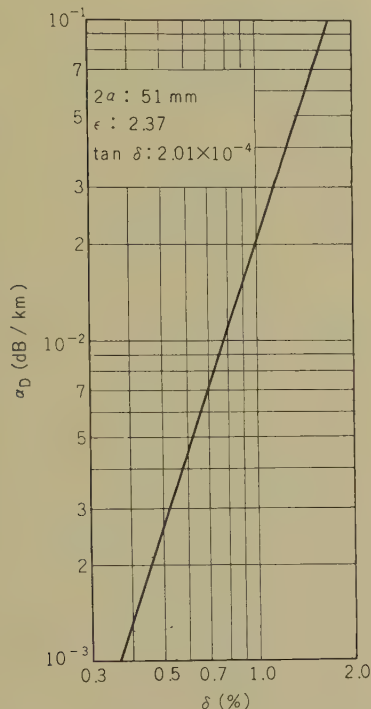


Fig. 2— $\alpha_D$  of TE<sub>01</sub> in case of  $2a=51$  mm,  $\epsilon=2.37$ , and  $\tan \delta=2.01 \times 10^{-4}$ .

$\Delta\alpha_M$  is the attenuation increase due to the increasing wall current caused by the existence of the dielectric layer, and is given also by Unger,<sup>(1)</sup> as follows:

$$\frac{\Delta\alpha_M}{\alpha_{[0m]}} = (\epsilon' - 1) \frac{k_{[0m]}^2}{\nu_{[0m]}^2} \delta^2. \quad (20)$$

The attenuation increase caused by bending the dielectric-coated waveguide consists of mode conversion loss and the increase of the TE<sub>01</sub> normal mode loss, as described above. We assume that the converted mode is only TM<sub>11</sub>, therefore the maximum conversion loss is

$$17.35 \frac{(c^+)^2}{\Delta\beta^2}, \quad (21)$$

where the coupling coefficient  $c$  between TE<sub>01</sub> and TM<sub>11</sub> is approximately<sup>(3)</sup>

$$c^+ = \frac{k_0 a}{\sqrt{2} k_{[01]} R} \left( 1 - \frac{1}{2} \frac{\epsilon_2' - 1}{\epsilon_2'} \delta \right). \quad (22)$$

The increase of TE<sub>01</sub> normal mode loss is

$$\frac{\Delta\alpha_c}{\alpha_1} = \frac{c^+}{\Delta\beta^2} \left( \frac{\alpha_2}{\alpha_1} - 1 \right), \quad (23)$$

where  $\alpha_1$  and  $\alpha_2$  are the attenuation constants of the TE<sub>01</sub> and the TM<sub>11</sub> modes, and approximation is good only when  $c \ll |\Delta\beta|$ . For waveguides of 51 mm diameter coated with a dielectric of  $\epsilon=2.37$ ,  $\tan \delta=2.01 \times 10^{-4}$  and  $\delta=0.8\%$ , then  $c^+=4.93/R$  and  $\Delta\beta=4.30$  rad/m from (22) and (19). And since for waveguides without a dielectric layer,  $\alpha_2/\alpha_1=48.6$ , then  $\Delta\alpha_c/\alpha_1=62.6/R^2$ , and it becomes 0.0696 for the bending radius of 30 m. In the case of the above mentioned numerical example,  $\alpha_D$  of the TM<sub>11</sub> mode is 6.22 dB/km which is a rather small value. But if  $\tan \delta$  is increased one-hundred times, then  $\alpha_D$  becomes 622 dB/km. Then adding the TM<sub>11</sub> loss of the waveguide without dielectric of 52 dB/km, the total attenuation reaches 674 dB/km. The TE<sub>01</sub> loss including dielectric loss is  $\alpha_1=3.37$  dB/km, then  $\alpha_2/\alpha_1=200$  and  $\Delta\alpha_c/\alpha_1=262/R^2$ . Therefore, the attenuation constant of the TE<sub>01</sub> mode is increased by 215% due to dielectric loss, moreover it further increases by 29.3% when the guide is bent with a bending radius of 30 m. This numerical example indicates that the dielectric material loss must be as low as possible in order to obtain a low loss dielectric-coated waveguide bend. Furthermore, we have the difficult problem of bonding the low loss dielectric to the metal.

## 1.2. Measurements of Dielectric Constants

Very familiar low loss dielectrics are polyethylene and polytetrafluoroethylene. The dielectric constants of these materials are essential values for the design of a dielectric-coated waveguide. Several workers have published measured values.<sup>(4)(5)</sup> Here we show the





**Table 1**  
 $\epsilon$  OF POLYETHYLENE AT 35 Gc/s

Frequency	Results			
34, 240 Gc/s	$l_1$ (mm)	4. 738	4. 564	Mean 2. 37
	$\epsilon$	2. 39	2. 34	
36. 538 Gc/s	$l_1$ (mm)	3. 388	3. 220	Mean 2. 37
	$\epsilon$	2. 40	2. 34	

depends on the piston position  $l_1$ . Table 1 and 2 show the measured values of  $\epsilon$  and  $\tan \delta$  of a polyethylene sample of 1.03 mm thickness. Deviations of the measured values were within 5% at 34,240 Gc/s, but they were very large at 36,538 Gc/s for large  $l_1$  because of undesired modes of the sample cavity. In Tables 1 and 2, only reliable results are adopted.

Table 3 shows the results with polytetrafluoroethylene. It is very difficult to bond this polymer to the metal in the required thickness range. Even so, it is a very important low loss material for the microwave region, and the measured values of  $\epsilon$  and  $\tan \delta$  should be useful. The thickness of the sample was

**Table 2**  
TAN  $\delta$  OF POLYETHYLENE AT 35 Gc/s

Frequency	Results							
34, 240 Gc/s	$l_1$ (mm)	2	3	4	4. 732	6	7	Mean (2. 01)
	( $\tan \delta \times 10^{-4}$ )	2. 11	1. 98	0. 98	2. 00	1. 92	2. 07	
36, 538 Gc/s	$l_1$ (mm)	1. 2	1. 5	1. 65	2	2. 5		Mean (2. 21)
	$\tan \delta (\times 10^{-4})$	2. 04	2. 18	2. 21	2. 21	2. 40		

**Table 3**  
 $\epsilon$  OF POLYTETRAFLUOROETHYLENE AT 35 Gc/s

Frequency	Results			
34, 229 Gc/s	$l_1$ (mm)	4. 739	3. 211	Mean (2. 07)
	$\epsilon$	2. 088	2. 058	
36, 536 Gc/s	$l_1$ (mm)	3. 690	3. 445	Mean (2. 10)
	$\epsilon$	2. 13	2. 07	

0.763 mm. The measured  $\tan \delta$ 's are shown in Table 4 only for the frequency of 34,536 Gc/s. The accuracy was not sufficient at the frequency of 36,536 Gc/s due to undesired modes.

2. Methods of Constructing Dielectric-Coated Waveguides

2.1. Problems of Construction

Plastic coating techniques are common in those industries which manufacture vessels for storing or tubes for transporting acids and alkalies. However low loss materials are indispensable for dielectric-coated waveguides, but they are not only hard to bond to metals

Table 4

TAN δ OF POLYTETRAFLUOROETHYLENE AT 35 GC/S

34, 229 Gc/s	$l_1$ (mm)	2.3	2.715	2.8	3.0	4.739	5.0	Mean (2.76)
	$\tau \delta (\times 10^{-4})$	2.53	2.67	2.82	2.49	2.83	3.23	

because of their non-polar characteristics, they also have many inconvenient characteristics, such as insolubleness in solvents, lack of flexibility, and unstableness of physical properties even when dissolved in a solvent.

First we used styrenated epoxy resin ester which is one of the thermosetting materials. Such materials have the defects that the dielectric loss is large and that smoothness of the surface is not easily obtainable.

Polytetrafluoroethylene is not only excellent electrically and stable chemically, but when it is heated and cast, the softening point and the resolving point are very close and it is very hard to obtain a thick layer. In general, a dispersed solution is used to coat a metal surface with this material. The desired thickness of the layer can be obtained with frequent repetition of dipping and baking. However a tortoise-shell shaped crack is apt to appear on the surface due to frequent coating.

Polyethylene is an electrically and chemically excellent material. It is very stable unless exposed to strong acid or ultraviolet rays; and further it is very cheap, has low losses and is very flexible. Its only defect is that it does not adhere to metals such as copper. But several methods have already been developed for the purpose of manufacturing acid-proof vessels, and moreover we developed other advanced methods for our own use. These methods are classified into the following; namely, flame spray method, whirl sinter method, powder dropping method, dispersed solution method, solution coating method and tube bonding method.

2.2. Flame Spray Method

A spray gun having three nozzles is used.

Oxygen sprays from the first, fuel gas from the second, and polyethylene powder spread in nitrogen from the third; and due to the high temperature, the polyethylene is in the molten state when it hits the metal part. By this method polyethylene is bonded with a very strong adhesive force, but the dielectric losses increase because the polyethylene is oxidized and is mixed with impurities. Moreover, the surface cannot easily be smoothly finished. It is usual practice in the manufacture of linings to sandblast the metal surface before applying the lining to remove oxides and to roughen the surface. Obviously such a technique cannot be used in waveguides where low attenuation is essential. Another defect of this technique is that a special spray gun must be developed.

2.3. Whirl Sinter Method

This method was developed for the purpose of coating small parts or electric wires with polyethylene. polyethylene powder in a vessel is floated on an air stream from the wire-netting at the bottom of the vessel, and pre-heated metal parts are inserted into the polyethylene cloud. Polyethylene powder touching the metal is melted by the high temperature and sticks to it. Next, the half-melted polyethylene covers the surface, and the surface looks like a doughnut covered with sugar. The metal part is picked out of the vessel and after cooling, it is heated again at a suitable temperature in an oven. Then the polyethylene layer melts again and the surface is finished smooth by surface tension. By this method, the polyethylene sticks to the metal with strong force because the part close to the metal is heated to a very high temperature, but the outside part is heated to a



comparatively low temperature, and this part of the polyethylene retains its low loss characteristics. This method gives a good compromise between good adhesion and good electrical characteristics. This method is not suitable for long waveguides because of practical difficulties in manufacturing.

2.4. Powder Dropping Method

The powder dropping method was developed from the method of the preceding section. Fig.5 explains this method schematically. The waveguide is heated to a temperature between 250°C and 350°C, and is set up vertically or obliquely. The vessel containing polyethylene powder is put on the waveguide, then the shutter is opened and polyethylene drops into the guide. In a few seconds, say 5 seconds, the shutter at the bottom of the waveguide is opened and then nearly all the polyethylene powder drops into the vessel put under the waveguide but a part of the powder sticks to the inner wall of the guide. The same processing as that mentioned in the preceding section continues after this process and a smooth surface can be obtained. Suitable reheating time and temperature are about 30 minutes and 140°C.

The thickness of the film can be controlled by the choice of the time interval between the opening of the upper and lower shutters,

and the temperature to which the waveguide is pre-heated. Polyethylene powder of about 50 meshes manufactured by the low pressure method was used, and the finished film thickness was about 0.2 mm at about 300°C and in 5 seconds.

By this method the polyethylene part near the guide wall is oxidized to a certain extent but has strong adhesion. The polyethylene part far from the waveguide wall holds its good electrical characteristics as in the preceding method. However, it is very difficult to bond two polyethylene layers separately, namely the first thin layer at high temperature and the second layer at comparatively low temperature. The first layer will adhere firmly but the second layer will fall off from the first polyethylene layer after cooling.

The uniformity of the layer depends on the surface tension and viscosity in the melted state. The viscosity of polyethylene is rather large, therefore some irregularity of the surface of the polyethylene is unavoidable. Fig.6 shows

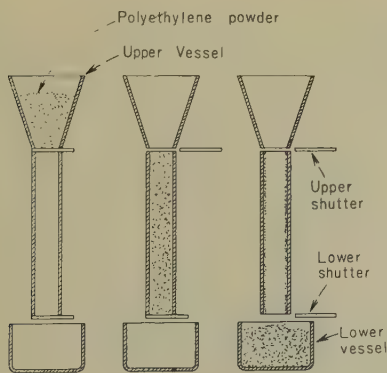
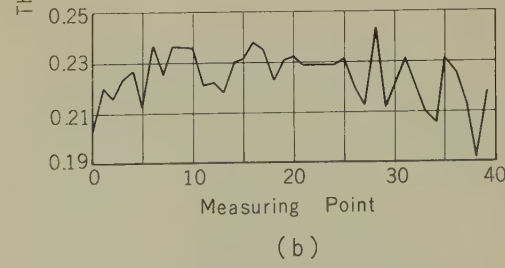
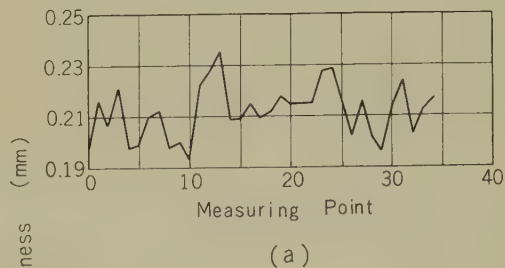


Fig. 5—Schematic diagram of the powder dropping method.



(a) in the axial direction.  
(b) in the circumferential direction.

Fig. 6—Thickness of the dielectric layer stripped from the dielectric-coated waveguide manufactured by the powder dropping method.

the thickness of the film of the dielectric-coated waveguide manufactured by the powder dropping method. The interval between two adjacent measurement points is 4 mm which is not small enough to follow the exact variation of the thickness. The roughnesses in the circumferential and longitudinal directions are fundamentally equal.

### 2.5. Dispersed Solution Method

Fine polyethylene powder of between 250 and 300 meshes is dispersed into trichloroethylene. A small part of the polyethylene dissolves into the trichloroethylene, but the viscosity is still poor. Then a small amount of toluene or xylene is added to the trichloroethylene. The dispersed solution is blown in to the inner surface of the waveguide by a spray-gun or by dipping, and then after volatilization of the solvent and dispersion solvent, the waveguide with polyethylene on the surface is heated, and a firm polyethylene film is formed on the surface. Dipping and heating must be repeated several times so that the desired thickness may be obtained. It is said that an excellent polyethylene layer whose molecular weight does not decrease can be formed by this method. Future developments are to be expected.

### 2.6. Solution Coating Method

Polyethylene can be dissolved into toluene and xylene at the temperature at which polyethylene melts. Such solutions are used to manufacture polyethylene-foamed wire. The wire is coated and then baked in an oven. A dense solution of polymer such as polystyrene dissolved into benzene or polyethylene dissolved into above mentioned solvents is apt to make bubbles while baking. Because the solvents near the surface volatilize rapidly, thin plastic films are formed immediately on the surface, and the solvent in the interior cannot volatilize; therefore bubbles are formed. Consequently, a dense solution must not be used, and the thickness formed by one baking must be very thin. Polyethylene formed by coating and drying is weaker than the

original polyethylene from the viewpoints of strength against the pulling and bending.

### 2.7. Tube Bonding Method

Polyethylene tube previously constructed is bonded to the inner surface of the waveguide with a bonding agent. Compared with the other methods this method yields excellent uniformity in thickness in the axial direction. The air is pulled out by a vacuum pump from the space between the waveguide and the polyethylene tube inserted into it as shown in Fig. 7 (a). The outer diameter of the tube is made a little smaller than the inner diameter of the waveguide.

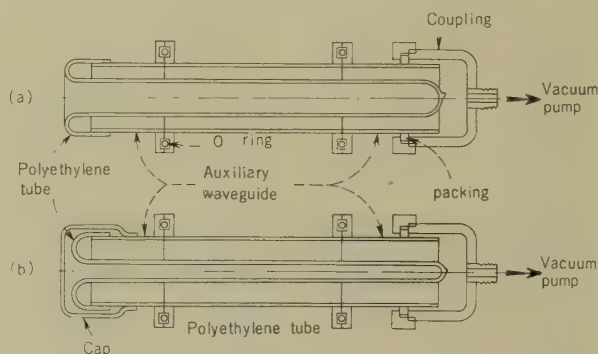


Fig. 7—Schematic diagram of tube bonding method.

“Cemedine 1200” made by the Cemedine Company and “Hydropol” made experimentally by the Phillips Petroleum Company are two typical bonding agents to bond polyethylene to metals. Fine powdered polyethylene dissolved in a solvent (see 3.5) is also useful as a bonding agent but the adhesion is not as good as that obtained when using the above two bonding agents. With Cemedine 1200, the dielectric-coated waveguide was completed when air is pulled out and the tube expands and sticks tightly to the inner surface. In the case of Hydropol or dispersed solution, the adhesive force appears by heating, under certain pressure. Hydropol, partly hydrogenated polybutadiene (8 per cent



unsaturation), is a white dry powder, and is dissolved in toluene. The procedure of the construction of the dielectric-coated waveguide is as follows: the waveguide is coated with Hydropol after its inner surface has been washed with trichloroethylene. One end of the polyethylene tube is folded out of the waveguide at one end of the guide as shown in Fig. 7 (a). Airtight sealing is completed by this simple process. The other end of the tube is sealed off, and the space between the tube and the waveguide is sealed with a coupling. Then the vacuum pump is started and the waveguide heated. The temperature of the waveguide is raised to between 150°C and 180°C. After cooling, both auxiliary waveguides are taken off and excess parts of the polyethylene tube are cut off.

The operation must be performed very carefully. Without preparation as described below, the tube will not expand uniformly by the action of the pump. Namely, if any part of the tube is even a little thinner than the remaining parts, this part expands rapidly and prevents the air from escaping past this part. To avoid such trouble, a cap is placed on the end of the waveguide as shown in Fig. 7 (b). Then the enclosing of air will never happen because the pressure in the tube is very low even under the action of the pump. The cap is removed after sufficient evacuation of air.

Polyethylene tube has been manufactured for a very long time by the inflation method. It is not tubular but rolled up on a reel continuously. It has two folds, but these can not be recognized in the completed dielectric-coated waveguide. The dimension of the tube is expressed not in diameter, but in rolled width. The accuracy of the rolled width is not very high. If the rolled width of the tube is too large for the guide, the completed waveguide is marked with a longitudinally raised stripe of polyethylene.

Next, the tube must be inserted into the waveguide carefully so as not to twist or loosen it, as otherwise wrinkles appear after the waveguide is gradually heated from one end to the other.

The polyethylene tube stretches in the

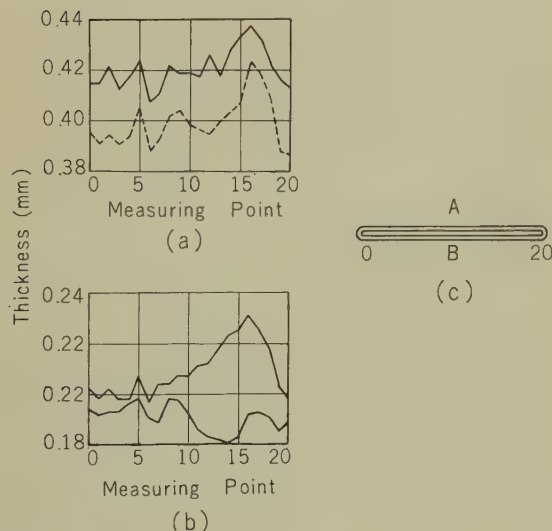
axial direction when the waveguide is heated from one end to the other due to the air pressure at the part just heated. Total extension is about 10 cm in the case of a 5 m long waveguide. The flanges cannot easily be raised to the same temperature as the inner part because the flanges have large heat capacities. Strong adhesion is necessary near the flange because especially strong shearing force acts on the polyethylene tube between the tube and the waveguide surface because of the shrinkage of the polyethylene due to temperature variations.

The preparatory processing to prevent gelling is explained in another paper.<sup>(7)</sup> This paper explains in detail suitable condition for bonding polyethylene to brass. The compound is made by mixing Hydropol and other several ingredients. Ten grams are dissolved in 100 cc of toluene, and applied with a spray gun or by brushing or dipping. The thickness of the dried film is approximately 0.08 mm, and the pressure applied to the polyethylene is about 7 km/cm<sup>2</sup>. In our experiments the situations were different. Namely, 100 per cent Hydropol was used at a pressure of about 1 kg/cm<sup>2</sup>, namely 1 atm, and the thickness of the dried Hydropol was very thin. Nevertheless, enough adhesive force has been obtained for our purpose.

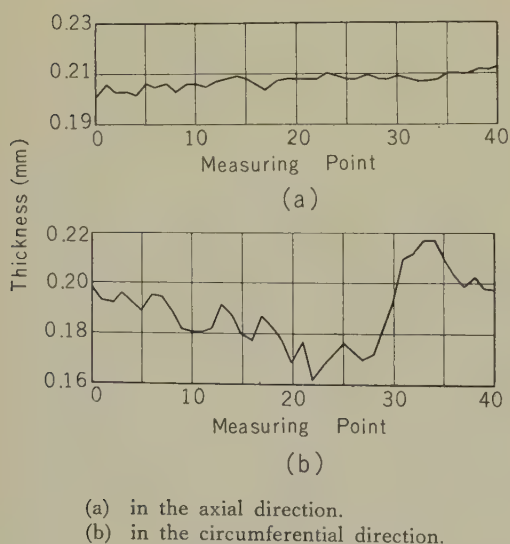
Fig. 8 shows the thickness of polyethylene layer manufactured by the tube bonding method, measured at intervals of 4 mm. The polyethylene tube has two folds as in Fig. 8 (c). Fig. 8 (a) shows the sum of the measured thickness of A and B sides, and the thickness of both sides measured together. The discrepancy between the two results in Fig. 8 (a) is due to deformation caused by the pressure of the micrometer. Two curves of Fig. 8 (b) show the thicknesses of the two sides, respectively.

Fig. 9 shows the thickness of the polyethylene tube stripped from the dielectric-coated waveguide manufactured by tube bonding method. The uniformity in thickness is very good in the axial direction, but not so good in the circumferential direction. The mode conversion will be small only if the uniformity is good in the axial direction, even though

not so good in the circumferential direction.<sup>(3)</sup> The tube bonding method is advantageous to construct such waveguide.



**Fig. 8**—Thickness of polyethylene tube made by infraction method. Interval between adjacent measuring points is 4 mm.



**Fig. 9**—Thickness of polyethylene layer by tube bonding method. Interval between adjoining measuring point is 4 mm.

### 3. Adhesive Force

The temperature at which polyethylene congeals is about 125°C. The temperature of the waveguide may be lowered to about -10°C in winter. The coefficient of expansion of polyethylene is larger than that of copper. At low temperatures, polyethylene is apt to be stripped from the waveguide due to shrinkage. In Fig. 10, shrinking force  $P$  is

$$P = E(\alpha_p - \alpha_c)T, \quad (25)$$

where  $E$  is modulus of elasticity,  $\alpha_p$  is coefficient of expansion of polyethylene,  $\alpha_c$  is coefficient of expansion of copper, and  $T$  is temperature difference. The adhesive force required to prevent stripping of the tube is

$$p = 2P \frac{t}{a} = 2E(\alpha_p - \alpha_c)T \frac{t}{a}, \quad (26)$$

where\*

$$\left. \begin{aligned} E &= (0.13 \sim 0.25) \times 10^4 \text{ kg/cm}^2, \\ \alpha_p &= (1.6 \sim 1.8) \times 10^{-14} / ^\circ\text{C}, \\ \alpha_c &= 1.7 \times 10^{-5} / ^\circ\text{C}. \end{aligned} \right\} \quad (27)$$

If  $t/a = 0.01$  and  $T = 135^\circ\text{C}$  are assumed, then

$$P = 25 \sim 55 \text{ kg/cm}^2. \quad (28)$$

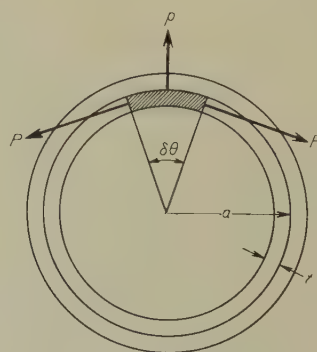


**Fig. 10**—Explanatory diagram of adhesive force.

\* Communication Handbook, Maruzen Book Co., Tokyo, Japan, 1957.

The maximum value in the above results is about half of ultimate tensile strength ( $110 \sim 130 \text{ kg/cm}^2$ ). The desired adhesive force is

$$p = 0.5 \sim 1.1 \text{ kg/cm}^2. \quad (29)$$

Even the highest value of (29) is only a little larger than 1 atm, thus only a small adhesive force is required in the middle part of the waveguide if there are no pinholes in the tube. The above estimate is based on the approximate coefficient of expansion of polyethylene, which is not constant in value but depends on the tensile force.

At the end of the waveguide, strong adhesive force is needed because the pressure of the atmosphere does not help in preventing stripping, and the shearing force due to the temperature variation or bending of the guide appear at the end part of the tube concentrically.

A heat cycle test was made using dry ice and alcohol. The temperature was varied three times between  $20^\circ \text{C}$  and  $-55^\circ \text{C}$ . It took about two hours for one cycle. A small part of the tube at the one end peeled off, but the greater part did not. By the way, at such low temperatures the adhesive force of polyvinyl tape and cellophane tape is lost but it recovers with temperature rise.

#### 4. Measurement of Electric Characteristics

As the first step, styrenated epoxy resin ester was used to make a dielectric-coated waveguide 15 m long. Measured attenuation constant before coating was  $5 \text{ dB/km}$  in the straight state at the frequency of  $24 \text{ Gc/s}$ . After coating the attenuation constant became  $15 \text{ dB/km}$ . Moreover, it became  $34 \text{ dB/km}$  when the waveguide was bent with a radius of 30 m. It is very difficult to coat this region uniformly on the inner surface of the guide due to the high viscosity of the solution. Moreover, because the thickness attainable by one coating is very small, coating must be repeated several times. Repeated cycles yielded coatings which were very irregular, and large lumps also appeared. When the waveguide is long, say 5 m, the difficulty is

large. Attenuation increase in the straight state is considered as due to the remarkable irregularity of the dielectric film. And the attenuation increase in the curved state is due not only to the loss and the irregularity of the dielectric but to incomplete junctions used in this measurement.

In the next step, a 23 m long dielectric-coated waveguide was manufactured by tube bonding method. This time, the frequency was  $51 \text{ Gc/s}$ . Fig. 11 shows that the attenuation constant in the straight state is about  $3.0 \text{ dB/km}$ , and Fig. 12 shows that it is about  $3.5 \text{ dB/km}$  in the curved state with the bending radius of 30 m. It was  $2.3 \text{ dB/km}$  before the tube had been bonded, thus the attenuation increase was about 30 per cent in the straight state, and 52 per cent in the curved state. Fig. 13 shows the schematic diagram of the measurement.

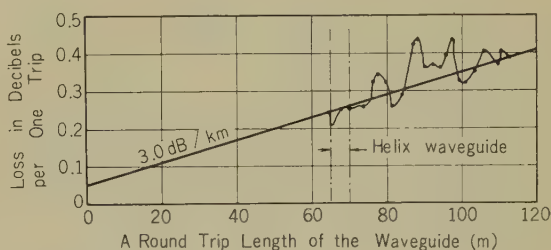


Fig. 11—The loss measurement of dielectric-coated waveguide manufactured by tube bonding method, by pulse reflection method. Inner diameter of waveguide is 51 mm, the thickness of dielectric is 0.22 mm, and the frequency is  $51 \text{ Gc/s}$ .

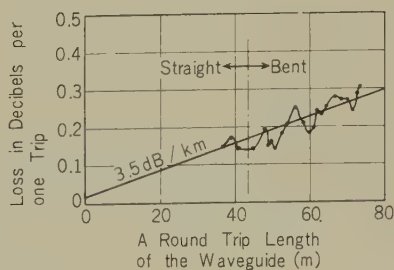


Fig. 12—The same as Fig. 11, except that the dielectric-coated waveguide is bent with a radius of 30 m.



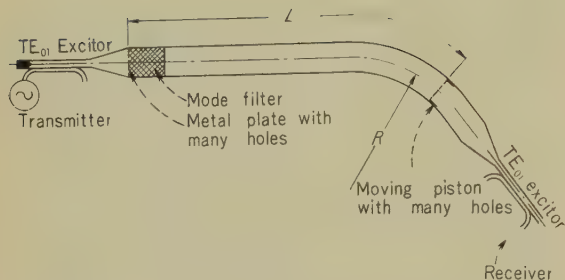


Fig. 13—Schematic diagram of the measurement of the attenuation of the dielectric-coated waveguide.

The height of the pulse on the cathode-ray tube is changed by the movement of a short piston at the end of the waveguide. Fig. 14 shows the variation of the pulse height for the movement of the piston. The period of the variation of the pulse is about 70 cm. The calculated deviation of the phase constant of  $TM_{11}$  from uncoated state is 4.46 radians per meter for this waveguide, with inner diameter of 51 mm, polyethylene layer of 0.22 mm ( $\delta=0.86$  per cent) and  $\epsilon=2.37$ . Half of the beat wavelength calculated from this phase constant deviation is 70.45 cm which coincides very well with the measured value.

### Conclusion

Attenuation increase due to the bonding agent layer is negligible for the  $TE_{01}$ , but appreciable for undesired modes. Thickness of the Hydropol used to bond the polyethylene tube in the waveguide is so thin that the low loss characteristics of this kind of waveguide will not be lost by dielectric loss in the Hydropol.

Six methods have been developed to construct polyethylene coated waveguides. The powder dropping method and the tube bonding method are the most promising. An especially smooth surface is obtained by the latter method. In this method a polyethylene tube is inserted into a waveguide coated with Hydropol, and after the air between the tube and the waveguide is pulled out by a vacuum pump, the waveguide is heated from the outside. The uniformity in the thickness of the film was excellent in the axial direction. Further developments to obtain stronger adhesive force and more uniform thickness of the film especially in the circumferential direction can be expected in the future.

The measured attenuation constants of the dielectric-coated waveguide by the tube bonding method were 3.0 dB/km in the straight state and 3.5 dB/km in the curved state with a bending radius of 30 m. Before coating it was 2.3 dB/km; therefore the attenuation increases are 30 and 52 per cent in the straight and curved states, respectively.

### Acknowledgment

The authors are indebted to the staff of the Electrical Communication Laboratory, especially to Messrs T. Miwa and M. Shimba, for their co-operation, assistance and valuable discussions. In addition to the Laboratory staff engineers, they wish to thank Messrs A. Konose and Y. Kubouchi, for their contribution to the success of the manufacturing methods.

### References

- (1) H. G. Unger, "Circular Electric Wave-Transmission in a Dielectric-Coated Waveguide,"

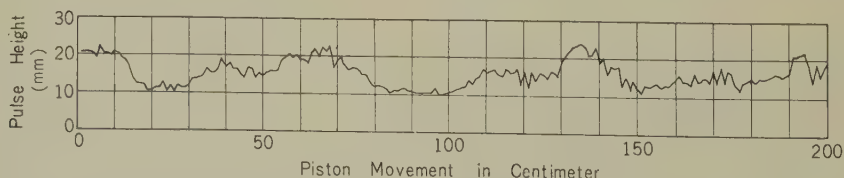


Fig. 14—The variation of the pulse height on the cathode-ray display caused by the piston movement.

- B.S.T.J.*, **36**, p. 1253, 1957.
- (2) H. G. Unger, "Round Waveguide with Double Lining," *B.S.T.J.*, **39**, p. 161, 1960.
- (3) K. Noda, "Circular Electric Wave Transmission through Hybrid Mode Waveguide," *Kenkyu Zituyoka Hokoku (Electr. Comm. Labor. Techn. Journ.)*, NTT, **9**, p. 585, 1960.
- (4) A. Von Hippel, "Dielectric Materials and Applications," J. Wiley, N. Y., p. 328, 1954.
- (5) S. Saito and K. Tanaka, "Measurements of the Dielectric Constants at the Band of 24 Gc/s," *Journ. Inst. Electr. Comm. Engrs. Japan*, **38**, p. 887, 1955.
- (6) M. Hoshiai and S. Saito, "Researches on Measurement of the Dielectric Constants at 4,000 Mc/s," *Electrical Communication Laboratory Internal Report*, **70**, 1951.
- (7) H. Peters and W. H. Lockwood, "Bonding Polyethylene to Rubber, Brass, and Brass-Plated Metals," Bell System Technical Paper, Monograph, 2932, 1958.

\* \* \* \*

U.D.C. 621.372.833  
621.372.822:621.372.823

# Mode Conversion in the Excitation of $TE_{01}$ Waves in a $TE_{01}$ Mode Transducer (Rectangular $\rightarrow$ Sector Portion $\rightarrow$ Circular)\*

Shin'ichi IIGUCHI†

Maxwell's equations expressed in oblique coordinates are obtained. The transverse fields in the cross sections of the transducer are expanded into a series of normal mode functions of sector waveguides; and by substituting this series expression into the Maxwell's equation obtained above, the author obtained a telegraphist's equation from which he derived inhomogeneous differential equations. By integrating numerically the solution of these equations, the magnitude of the unused mode is obtained.

The theoretical values of the magnitude of the unused  $TE_{11}$ ,  $TE_{21}$ ,  $TE_{31}$  and  $TM_{11}$  modes agree with the experimental results within about 1 dB.

## Introduction

The  $TE_{01}$  mode transducer employing gradual transition from a rectangular to a circular waveguide through sector sections has been widely known since 1949. Its transmission characteristics, however, are not known.

The author constructed three types of transducers of this kind in 1953, but since the mode analyzer used then was not good enough, the transducers were judged poor in transducing characteristics. Recently, it was felt necessary to re-examine the performance of these transducers, and theoretical calculations were made. The results obtained revealed a fairly high mode purity and it is concluded that this type has good enough wide-band and low-loss characteristics provided that electroforming is employed in their construction. Electroformed waveguides do not require soldering, which is the main cause of high losses.

## 1. Coordinate Systems

The central angle of the sector space surrounded by the metal surface is flared progressively and the edge helix curve of the space is expressed by

$$x = a \cos \phi, \quad y = a \sin \phi, \quad z = B\phi,$$

where  $B$  is the constant which is determined by the geometrical configuration of the transducer

$$B = \frac{z}{\phi} = \text{constant}.$$

The formulas of the inner helix curves are

$$x = r \cos \phi, \quad y = r \sin \phi, \quad z = z.$$

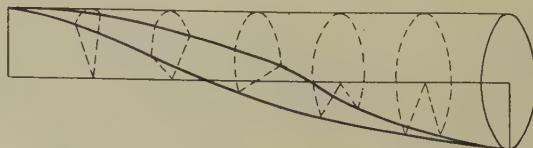


Fig. 1— $TE_{01}$  wave transducer.

\* Contributed to the *Symposium on Millimeter Waves*, Polytechnic Institute of Brooklyn, March 31 and April 1 and 2, 1959. Published in the *Institute of the Electrical Communication Engineers of Japan*, Vol. 42, No. 12, pp. 1213-1219, 1959.

† Hyper-frequency Research Section.



Defining

$$\tau = \frac{\phi}{\psi}$$

we have

$$x = r \cos \frac{\tau z}{B}, \quad y = r \sin \frac{\tau z}{B}, \quad z = z.$$

### Glossary of Symbols

- $x, y, z$  = right-handed cartesian coordinates  
 $r, \phi, z$  = right-handed cylindrical coordinates  
 $2\psi$  = flared angle of sector of metal surface  
 $a$  = inner radius of waveguide  
 $(mn), (MN)$  = subscripts of TM mode:  
 $(mn)$ , general wave  
 $(MN)$ , specific wave  
 $[mn], [MN]$  = subscripts of TE mode:  
 $[mn]$ , general wave  
 $[MN]$ , specific wave  
 $V_{mn}$  = amplitude of electric field  
 $I_{mn}$  = amplitude of magnetic field  
 $\beta_{pn}, \beta_{pN}$  = phase constant:  
 $pn$ , general wave  
 $pN$ , specific wave  
 $k_{(pn)}$  =  $n$ -th zero of  $J_p(X)$   
 $k_{[pn]}$  =  $n$ -th zero of  $J_p'(X)$

$$B = \phi/z, \quad \tau = \phi/\psi, \quad e_2 = rz/B,$$

$$\chi_{pn} = k_{pn}/a, \quad p = m\pi B/z.$$

### 2. Maxwell's Equations in Oblique Coordinates

The general theory for deriving Maxwell's equations in oblique coordinates is given in

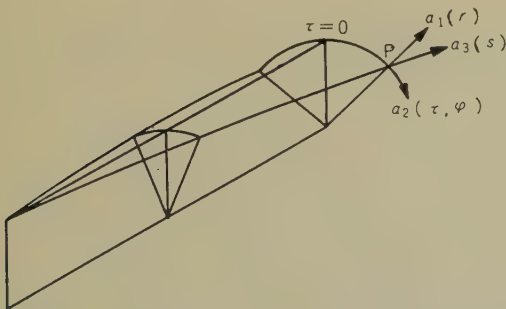


Fig. 2—Curvilinear coordinates of TE<sub>01</sub> wave transducer.

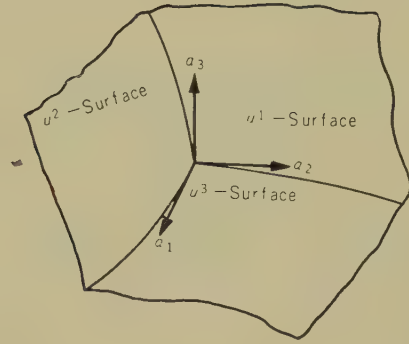


Fig. 3—Curvilinear coordinate system.

full detail in Reference (1), hence we can apply these equations to our transducer immediately without explaining them again in this paper.

The position vector  $\mathbf{r}$  from an arbitrary origin to a variable point P is expressed by

$$\mathbf{r} = \mathbf{i}_x \left( r \cos \frac{\tau z}{B} \right) + \mathbf{i}_y \left( r \sin \frac{\tau z}{B} \right) + \mathbf{i}_z (z).$$

For the symbols  $g_{ij}$ , which are the scalar products of unitary vectors, we obtain

$$\begin{pmatrix} g_{11} & g_{12} & g_{13} \\ g_{21} & g_{22} & g_{23} \\ g_{31} & g_{32} & g_{33} \end{pmatrix} = \begin{pmatrix} 1 & 0 & 0 \\ 0 & \left( \frac{rz}{B} \right)^2 & \frac{\tau r^2 z}{B^2} \\ 0 & \frac{\tau r^2 z}{B^2} & 1 + \left( \frac{\tau r}{B} \right)^2 \end{pmatrix}.$$

By using the symbols  $g_{ij}$  we express  $f_i$  by  $F_i$ , and we obtain the divergence and the curl of the vector  $\mathbf{F}$ . By substituting the notation  $F_r, F_\tau$ , and  $F_s$  for  $F_1, F_2$  and  $F_3$  respectively; and  $r, \tau$  and  $z$  for  $u^1, u^2$ , and  $u^3$ ; we obtain the following Maxwell's equations in the first order approximation of  $(\tau r/B)$ ; where  $g_{ij}, f_i, F_i$ , and  $u^i$  all have the same meaning as the corresponding symbols used in Reference (1).

$$B \left[ \frac{\partial E_s}{\partial \tau} + \frac{\partial \left( \frac{\tau r}{B} E_\tau \right)}{\partial \tau} - \frac{\partial \left( \frac{rz}{B} E_r \right)}{\partial z} \right]$$

$$\left. \begin{aligned}
 & -\frac{\partial\left(\frac{\tau r^2 z}{B^2} E_s\right)}{\partial z} = -j\omega\mu H_r. \\
 & \frac{\partial E_r}{\partial z} - \frac{\partial E_s}{\partial r} - \frac{\partial\left(\frac{\tau r}{B} E_r\right)}{\partial r} = -j\omega\mu H_r. \\
 & B \left[ \frac{\partial\left(\frac{rz}{B} E_r\right)}{\partial r} + \frac{\partial\left(\frac{\tau r^2 z}{B^2} E_s\right)}{\partial r} - \frac{\partial E_r}{\partial \tau} \right] \\
 & \quad = -j\omega\mu H_s. \\
 & B \left[ \frac{\partial H_s}{\partial \tau} + \frac{\partial\left(\frac{\tau r}{B} H_r\right)}{\partial \tau} - \frac{\partial\left(\frac{rz}{B} H_r\right)}{\partial z} \right] \\
 & \quad - \frac{\partial\left(\frac{\tau r^2 z}{B^2} H_s\right)}{\partial z} = j\omega\epsilon E_r. \\
 & \frac{\partial H_r}{\partial z} - \frac{\partial H_s}{\partial r} - \frac{\partial\left(\frac{\tau r}{B} H_r\right)}{\partial r} = j\omega\epsilon E_r. \\
 & B \left[ \frac{\partial\left(\frac{rz}{B} H_r\right)}{\partial r} + \frac{\partial\left(\frac{\tau r^2 z}{B^2} H_s\right)}{\partial r} - \frac{\partial H_r}{\partial \tau} \right] \\
 & \quad = j\omega\epsilon E_s. \\
 & \frac{\partial\left(\frac{rz}{B} E_r\right)}{\partial r} + \frac{\partial E_r}{\partial \tau} + \frac{\partial\left(\frac{rz}{B} E_s\right)}{\partial z} = 0 \\
 & \frac{\partial\left(\frac{rz}{B} H_r\right)}{\partial r} + \frac{\partial H_r}{\partial \tau} + \frac{\partial\left(\frac{rz}{B} H_s\right)}{\partial z} = 0.
 \end{aligned} \right\} (1)$$

### 3. Expansion of Transverse Electric and Magnetic Fields<sup>(2)</sup>

The transverse electric and magnetic fields in a cross section of the transducer can be expanded into the series of normal mode functions of sector waveguides.

$$\left. \begin{aligned}
 E_r &= V_{(mn)} \frac{\partial T_{(mn)}}{\partial r} + V_{[mn]} \frac{\partial T_{[mn]}}{e_2 \partial \tau} \\
 E_r &= V_{(mn)} \frac{\partial T_{(mn)}}{e_2 \partial \tau} - V_{[mn]} \frac{\partial T_{[mn]}}{\partial r}
 \end{aligned} \right\}$$

$$\left. \begin{aligned}
 H_r &= I_{(mn)} \frac{\partial T_{(mn)}}{\partial r} + I_{[mn]} \frac{\partial T_{[mn]}}{e_2 \partial \tau} \\
 H_r &= -I_{(mn)} \frac{\partial T_{(mn)}}{e_2 \partial \tau} + I_{[mn]} \frac{\partial T_{[mn]}}{\partial r} \\
 e_2 &= rz/B.
 \end{aligned} \right\} (3)$$

The  $T_{[mn]}$  and  $T_{(mn)}$  functions are expressed by the following equations: (See appendix).

$$T_{[mn]} = -\sqrt{\epsilon_m} \frac{1}{\sqrt{k_{[pn]}^2 - p^2}} \times \frac{J_p(\chi_{[pn]} r)}{J_p(\chi_{[pn]} a)} \cos m\pi\tau; \quad (4)$$

$$T_{(mn)} = -\sqrt{\epsilon_m} \frac{1}{k_{(pn)}} \frac{J_p(\chi_{(pn)} r)}{J_{p+1}(\chi_{(pn)} a)} \sin m\pi\tau \quad (5)$$

where

$$\epsilon_m = 2 \quad (m \neq 0), \quad \epsilon_m = 1 \quad (m = 0).$$

For  $T$  functions orthogonality relations hold,

$$\left. \begin{aligned}
 & \iint (\text{grad } T)(\text{grad } T) d\Omega = \chi^2 \iint T^2 d\Omega = 1 \\
 & \iint T_{(m_1 n_1)} T_{(m_2 n_2)} d\Omega \\
 & \quad = \iint T_{[m_1 n_1]} T_{[m_2 n_2]} d\Omega = 0 \\
 & \iint (\text{grad } T_{(m_1 n_1)})(\text{grad } T_{(m_2 n_2)}) d\Omega = 0 \\
 & \iint (\text{grad } T_{[m_1 n_1]})(\text{grad } T_{[m_2 n_2]}) d\Omega = 0
 \end{aligned} \right\} (6)$$

where  $m_1 n_1 \neq m_2 n_2$  and  $d\Omega = r dr d\tau$ .

For the power relation, we have:

$$\text{Power} = \text{Re} \iint (-E_r H_r^* + E_r H_r^*) r dr d\phi. \quad (7)$$

Substituting Eq. (3) in the right side of Eq. (7) and using the first formula of Eq. (6), we obtain:

$$\begin{aligned} \text{Power} &= \text{Re} \left\{ \psi V I^* \right\} \iint (\text{grad } T_{mn})^2 r dr d\tau \\ &= \text{Re} \{ \psi V I^* \} = \text{Re} \left\{ \frac{z}{B} V I^* \right\}. \quad (8) \end{aligned}$$

#### 4. Derivation of Telegraphist's Equations

Substituting (3) in the third and sixth formulas of (1), we have, neglecting the terms higher than  $(\tau r/B)$ ,

$$\begin{aligned} H_s &= I_{(mn)} \frac{\chi^2_{(pn)}}{-\omega^2 \mu \varepsilon} \frac{2\tau}{B} T_{(mn)} + I_{(mn)} \frac{\chi^2_{(pn)}}{-\omega^2 \mu \varepsilon} \\ &\times \frac{\tau r}{B} \frac{\partial T_{(mn)}}{\partial r} + V_{[mn]} \frac{\chi^2_{[pn]}}{-j\omega \mu} T_{[pn]}; \quad (9) \end{aligned}$$

$$\begin{aligned} E_s &= I_{(mn)} \frac{\chi^2_{(pn)}}{-j\omega \varepsilon} T_{(mn)} + V_{[mn]} \frac{\chi^2_{[pn]}}{\omega^2 \mu \varepsilon} \frac{2\tau}{B} T_{[mn]} \\ &+ V_{[mn]} \frac{\chi^2_{[pn]}}{\omega^2 \mu \varepsilon} \frac{\tau r}{B} \frac{\partial T_{[mn]}}{\partial r}. \quad (10) \end{aligned}$$

Then we try to rewrite the Maxwell's equations (1) into convenient forms. From the first formula of Eq. (2)

$$-\frac{\partial \left( \frac{rz}{B} E_s \right)}{\partial z} = -\frac{\partial \left( \frac{rz}{B} E_r \right)}{\partial r} + \frac{\partial E_\tau}{\partial \tau}. \quad (11)$$

After substituting Eq. (11) in the fourth term of the first formula of Eq. (1), then further substituting Eq. (3), the fourth term of the first formula of Eq. (1) becomes

$$\begin{aligned} &-\frac{B}{rz} \frac{\partial \left( \frac{\tau r^2 z}{B^2} E_s \right)}{\partial z} \\ &= \frac{\tau}{B} E_r + \frac{\tau r}{B} \frac{\partial E_r}{\partial r} + \frac{\tau}{z} \frac{\partial E_\tau}{\partial \tau} \\ &= \sum_{mn} \frac{\tau r}{B} [-\chi^2_{(pn)} T_{(mn)}] V_{(mn)}. \quad (12) \end{aligned}$$

Similarly, using the second formula of Eq. (2), the fourth term of the fourth formula of Eq. (1) becomes

$$\sum_{mn} \frac{\tau r}{B} [-\chi^2_{[pn]} T_{[mn]}] I_{[mn]}. \quad (13)$$

The first, second, fourth and fifth formulas of Eq. (1), which are modified by using Eq. (12), Eq. (13) and  $E_a = E_s + (\tau r/B) E_r$ , take the following forms:

$$\begin{aligned} &\frac{B}{rz} \frac{\partial E_a}{\partial \tau} - \frac{\partial E_\tau}{\partial z} - \frac{1}{z} E_\tau \\ &+ \sum_{mn} \frac{\tau r}{B} (-\chi^2_{(pn)} T_{(mn)}) V_{(mn)} = -j\omega \mu H_r \\ &\frac{\partial E_\tau}{\partial z} - \frac{\partial E_a}{\partial r} = -j\omega \mu H_\tau \\ &\frac{B}{rz} \frac{\partial H_s}{\partial \tau} + \frac{\tau}{z} \frac{\partial H_r}{\partial \tau} - \frac{\partial H_\tau}{\partial z} \\ &+ \sum_{mn} \frac{\tau r}{B} (-\chi^2_{[pn]} T_{[mn]}) I_{[mn]} = j\omega \varepsilon E_r \\ &\frac{\partial H_r}{\partial z} - \frac{\partial H_s}{\partial r} - \frac{\tau}{B} H_\tau - \frac{\tau r}{B} \frac{\partial H_\tau}{\partial \tau} = j\omega \varepsilon E_\tau. \quad (14) \end{aligned}$$

#### 4.1. Derivation of $dV_{[01]}/dz$

We substitute Eq. (3) in the first formula of Eq. (14), then multiply by  $[\partial T_{[01]}/\partial r] r dr d\tau$ , and integrate over the cross section. For the first term, we obtain

$$\begin{aligned} &\iint \frac{B}{rz} \frac{\partial E_a}{\partial \tau} \frac{\partial T_{[01]}}{\partial r} r dr d\tau \\ &= \frac{B}{z} \int_0^a \frac{\partial T_{[01]}}{\partial r} dr \int_{-1}^{+1} \frac{\partial E_a}{\partial \tau} d\tau \\ &= \frac{B}{z} \int_0^a \frac{\partial T_{[01]}}{\partial r} dr \left[ E_a \right]_{\tau=-1}^{\tau=1}. \end{aligned}$$

As  $[E_a]_{\tau=\pm 1}$  is the tangential component of electric field on the surface of the wall, it is zero. Then we get the following formula easily.

$$\frac{dV_{[01]}}{dz} + j\omega \mu I_{[01]} + \frac{1}{z} V_{[01]}$$



$$= V_{(MN)} \chi^2_{(\rho N)} \frac{1}{B} \iint \tau r T_{(MN)} \frac{\partial T_{[01]}}{\partial r} r dr d\tau. \quad (15)$$

#### 4.2. Derivation of $dV_{[MN]}/dz$

We substitute Eq. (3) into the first and second formulas of Eq. (14) and multiply them by  $[\partial T_{[MN]}/\partial r] r dr d\tau$  and  $[\partial T_{[MN]}/\partial \tau] r dr d\tau$ , respectively, then add and integrate over the cross section. For the term containing  $E_a$ , we have

$$\begin{aligned} & \iint \frac{B}{rz} \frac{\partial E_a}{\partial \tau} \frac{\partial T_{[MN]}}{\partial r} r dr d\tau - \iint \frac{\partial E_a}{\partial r} \frac{\partial T_{[MN]}}{\partial \tau} r dr d\tau \\ & \times r dr d\tau = \frac{B}{z} \left[ \int dr \left\{ \frac{\partial E_a}{\partial \tau} \frac{\partial T_{[MN]}}{\partial r} d\tau \right\} \right. \\ & \left. - \int d\tau \left\{ \frac{\partial E_a}{\partial r} \frac{\partial T_{[MN]}}{\partial \tau} dr \right\} \right] \quad (16) \end{aligned}$$

and

$$\left. \begin{aligned} & \int \frac{\partial E_a}{\partial \tau} \frac{\partial T_{[MN]}}{\partial r} d\tau = \left[ E_a \frac{\partial T_{[MN]}}{\partial r} \right]_{\tau=-1}^{\tau=1} \\ & - \int E_a \frac{\partial^2 T_{[MN]}}{\partial \tau \partial r} d\tau = - \int E_a \frac{\partial^2 T_{[MN]}}{\partial \tau \partial r} d\tau \\ & \int \frac{\partial E_a}{\partial r} \frac{\partial T_{[MN]}}{\partial \tau} dr = \left[ E_a \frac{\partial T_{[MN]}}{\partial \tau} \right]_{r=0}^{r=a} \\ & - \int E_a \frac{\partial^2 T_{[MN]}}{\partial r \partial \tau} dr = - \int E_a \frac{\partial^2 T_{[MN]}}{\partial r \partial \tau} dr. \end{aligned} \right\} \quad (17)$$

In view of Eq. (17), Eq. (16) reduces to zero. Taking account of this, we obtain

$$\begin{aligned} & \frac{dV_{[MN]}}{dz} + j\omega \mu I_{[MN]} \\ & + \frac{1}{z} V_{[MN]} \iint \left[ \frac{\partial T_{[MN]}}{\partial r} \right]^2 r dr d\tau = 0. \quad (18) \end{aligned}$$

#### 4.3. Derivation of $dV_{(MN)}/dz$

We substitute (3) in the first and second formulas of (14), multiply them by  $-\partial T_{(MN)}/\partial \tau r dr d\tau$  and  $[\partial T_{(MN)}/\partial r] r dr d\tau$ , respectively, then add and integrate over the cross section.

For the term containing  $E_a$ , we have

$$\begin{aligned} & - \iint \frac{B}{rz} \frac{\partial E_a}{\partial \tau} \frac{\partial T_{(MN)}}{\partial \tau} r dr d\tau \\ & - \iint \frac{\partial E_a}{\partial r} \frac{\partial T_{(MN)}}{\partial r} r dr d\tau \\ & = - \left( \frac{B}{rz} \right)^2 r dr \left[ \left\{ E_a \frac{\partial T_{(MN)}}{\partial \tau} \right\}_{\tau=-1}^{\tau=1} \right. \\ & \left. - \int_{-1}^1 E_a \frac{\partial^2 T_{(MN)}}{\partial \tau^2} d\tau \right], \\ & - \int d\tau \left\{ E_a \frac{\partial T_{(MN)}}{\partial r} r \right\}_{r=0}^{r=a} \\ & - \int_0^a E_a \left( \frac{\partial^2 T_{(MN)}}{\partial r^2} r + \frac{\partial T_{(MN)}}{\partial r} \right) dr \\ & = \iint E_a \left[ \left( \frac{B}{rz} \right)^2 \frac{\partial^2 T_{(MN)}}{\partial \tau^2} + \frac{\partial^2 T_{(MN)}}{\partial r^2} \right. \\ & \left. + \frac{1}{r} \frac{\partial T_{(MN)}}{\partial r} \right] r dr d\tau \\ & = - \iint \left\{ E_a (\chi^2_{(\rho N)} T_{(MN)}) r dr d\tau. \right. \end{aligned}$$

From this result, we can obtain

$$\begin{aligned} & \frac{dV_{(MN)}}{dz} - \frac{\beta^2_{(\rho N)}}{j\omega \epsilon} I_{(MN)} \\ & + \frac{1}{z} V_{(MN)} \iint \left[ \frac{\partial T_{(MN)}}{\partial \tau} \right]^2 r dr d\tau \\ & = - V_{[01]} \frac{\beta^2_{[01]}}{\omega^2 \mu \epsilon} \frac{1}{B} \iint \tau r \frac{\partial T_{[01]}}{\partial r} \\ & \times (\chi^2_{(\rho N)} T_{(MN)}) r dr d\tau + V_{[01]} \frac{\chi^2_{[01]}}{\omega^2 \mu \epsilon} \frac{2}{B} \\ & \times \iint \tau T_{[01]} (\chi^2_{(\rho N)} T_{(MN)}) r dr d\tau. \quad (19) \end{aligned}$$

#### 4.4. Derivation of $dI_{[01]}/dz$

Substituting Eqs. (3) and (9) into the third formula of Eq. (14), multiplying it by  $[dT_{[01]}/\partial r] r dr d\tau$ , and integrating over the cross section, we obtain

$$\begin{aligned}
\frac{dI_{[01]}}{dz} - \frac{\beta_{[01]}^2}{j\omega\mu} V_{[01]} &= I_{[MN]} \frac{1}{B} \left[ \iint \tau \frac{\partial T_{[MN]}}{e_2 \partial \tau} \right. \\
&\times \frac{\partial T_{[01]}}{\partial r} r dr d\tau + \iint \tau r \frac{\partial^2 T_{[MN]}}{\partial r e_2 \partial \tau} \frac{\partial T_{[01]}}{\partial r} r dr d\tau \Big] \\
&+ I_{(MN)} \frac{1}{B} \iint \tau \frac{\partial T_{(MN)}}{\partial r} \frac{\partial T_{[01]}}{\partial r} r dr d\tau \left[ 1 - \frac{3\chi_{(\rho N)}^2}{\omega^2 \mu \varepsilon} \right] \\
&+ I_{(MN)} \frac{1}{B} \iint \tau r \frac{\partial^2 T_{(MN)}}{\partial r^2} \frac{\partial T_{[01]}}{\partial r} r dr d\tau \\
&\times \left[ 1 - \frac{\chi_{(\rho N)}^2}{\omega^2 \mu \varepsilon} \right]. \quad (20)
\end{aligned}$$

#### 4.5. Derivation of $dI_{[MN]}/dz$

Substituting Eqs. (3) and (9) into the third and fourth formulas of Eq. (14), multiplying them by  $[-\partial T_{[MN]}/e_2 \partial \tau] r dr d\tau$  and  $[\partial T_{[MN]}/\partial r] \times r dr d\tau$ , respectively, adding integrating over the cross section, we get Eq. (22) in view of Eq. (21).

$$\begin{aligned}
&\iint \left[ -\frac{\tau r}{B} \frac{\partial^2 T_{[MN]}}{\partial r e_2 \partial \tau} \frac{\partial T_{[MN]}}{\partial r} - \frac{\tau}{B} \frac{\partial T_{[MN]}}{e_2 \partial \tau} \right. \\
&\times \frac{\partial T_{[MN]}}{\partial r} + \frac{\tau r}{B} (\chi_{(\rho N)}^2 T_{[MN]}) \frac{\partial T_{[MN]}}{e_2 \partial \tau} \Big] r dr d\tau \\
&= - \iint \frac{\tau}{z} \frac{\partial^2 T_{[MN]}}{\partial \tau e_2 \partial \tau} \frac{\partial T_{[MN]}}{e_2 \partial \tau} r dr d\tau; \quad (21)
\end{aligned}$$

$$\begin{aligned}
\frac{dI_{[MN]}}{dz} - \frac{\beta_{[MN]}^2}{j\omega\mu} V_{[MN]} - 2I_{[MN]} \\
\times \iint \frac{\tau}{z} \frac{\partial^2 T_{[MN]}}{\partial \tau e_2 \partial \tau} \frac{\partial T_{[MN]}}{e_2 \partial \tau} r dr d\tau \\
= -I_{[01]} \chi_{[01]}^2 \frac{1}{B} \iint \tau r T_{[01]} \frac{\partial T_{[MN]}}{e_2 \partial \tau} r dr d\tau. \quad (22)
\end{aligned}$$

#### 4.6. Derivation of $dI_{(MN)}/dz$

Substituting Eqs. (3) and (9) in the third and fourth formulas of Eq. (14), multiplying them by  $[dI_{(MN)}/dz] r dr d\tau$  and  $[\partial T_{(MN)}/e_2 \partial \tau] r dr d\tau$ , respectively, adding and integrating over the cross section, we get Eq. (24) in view of Eq. (23).

$$\begin{aligned}
&\iint \left[ \frac{\tau}{z} \frac{\partial^2 T_{(MN)}}{\partial \tau \partial r} \frac{\partial T_{(MN)}}{\partial r} + \frac{1}{z} \frac{\partial T_{(MN)}}{\partial r} \frac{\partial T_{(MN)}}{\partial r} \right. \\
&- \frac{\tau}{B} \frac{\partial T_{(MN)}}{\partial r} \frac{\partial T_{(MN)}}{e_2 \partial \tau} - \frac{\tau r}{B} \frac{\partial^2 T_{(MN)}}{\partial r^2} \\
&\times \frac{\partial T_{(MN)}}{e_2 \partial \tau} \Big] r dr d\tau = 0, \\
&\iint \left[ \frac{1}{r} T_{(MN)} \frac{\partial T_{(MN)}}{\partial r} \right] r dr d\tau = 0, \\
&- \iint \left\{ \frac{\tau}{B} \frac{\partial T_{(MN)}}{\partial r} \frac{\partial T_{(MN)}}{e_2 \partial \tau} \right. \\
&+ \frac{\tau r}{B} \frac{\partial^2 T_{(MN)}}{\partial r^2} \frac{\partial T_{(MN)}}{e_2 \partial \tau} \Big\} r dr d\tau \\
&= \iint \frac{\tau}{z} \frac{\partial^2 T_{(MN)}}{\partial \tau \partial r} \frac{\partial T_{(MN)}}{\partial r} r dr d\tau. \quad (23)
\end{aligned}$$

$$\begin{aligned}
\frac{dI_{(MN)}}{dz} + j\omega\varepsilon V_{(MN)} - \frac{1}{z} I_{(MN)} \\
\times \iint 2\tau \frac{\partial^2 T_{(MN)}}{\partial \tau \partial r} \frac{\partial T_{(MN)}}{\partial r} r dr d\tau \\
= -I_{[01]} \chi_{[01]}^2 \frac{1}{B} \iint \tau r T_{[01]} \frac{\partial T_{(MN)}}{\partial r} r dr d\tau. \quad (24)
\end{aligned}$$

#### 5. Integral Forms of Magnitudes of Generated Unused Modes

The  $TE_{01}$  mode is excited at the entrance of a sector waveguide by the  $TE_{10}$  mode of rectangular waveguide. This sector  $TE_{01}$  mode is modified gradually to the circular  $TE_{01}$  mode through the transducer section. The circular modes excited at this section are, however, not limited to the  $TE_{01}$  mode; there are also suprious  $TE_{MN}$  and  $TM_{MN}$  modes. To calculate these latter modes excited continually in the course of propagation through the transducer section, a reciprocal method based on the reciprocal theorem is applied here.

The magnitude of the  $TE_{01}$  mode that is generated from  $TE_{MN}$  or  $TM_{MN}$  modes coming from the circular waveguide to the transducer section and propagating through

this section is calculated. Exactly speaking, the energy of the primary  $TE_{MN}$  or  $TM_{MN}$  mode must decrease due to the conversion to the  $TE_{01}$  mode, but it is assumed here that the primary wave remains constant because the secondary waves generated are very weak. Also, the generated  $TE_{MN}$  or  $TM_{MN}$  modes (tertiary waves) due to the reconversion from the  $TE_{01}$  wave generated are neglected.

### $TE_{01}$ Mode Generated from $TE_{MN}$ Mode

Combining the terms relating to  $TE_{MN}$  in the right sides of Eqs. (15) and (20), we derive a second-order linear inhomogeneous differential equation concerning  $V_{[01]}$ :

$$\frac{d^2 V_{[01]}}{dz^2} + \frac{1}{z} \frac{dV_{[01]}}{dz} + \left( \beta_{[01]}^2 - \frac{1}{z^2} \right) V_{[01]} = -j\omega\mu g(z) I_{[MN]} \quad (25)$$

where

$$\begin{aligned} g(z) &= \frac{1}{B} \left[ \iint \tau \frac{\partial T_{[MN]}}{\partial z \partial \tau} \frac{\partial T_{[01]}}{\partial r} r dr d\tau \right. \\ &\quad \left. + \iint \tau r \frac{\partial^2 T_{[MN]}}{\partial r \partial z \partial \tau} \frac{\partial T_{[01]}}{\partial r} r dr d\tau \right], \\ I_{[MN]} &= -\sqrt{\frac{B}{z}} \sqrt{\frac{\beta_{[\rho N]}}{\omega\mu}} e^{j\beta_{[\rho N]}z} dz \\ V_{[01]} &= S_{[01]} \sqrt{\frac{B}{z}} \sqrt{\frac{\omega\mu}{\beta_{[01]}}} e^{j\beta_{[01]}z}. \end{aligned} \quad \left. \begin{array}{l} \\ \\ \end{array} \right\} \text{(See Appendix)}$$

Solving Eq. (25), we obtain

$$\begin{aligned} V_{[01]} &= \sqrt{\frac{B}{z}} \sqrt{\frac{\omega\mu}{\beta_{[01]}}} e^{j\beta_{[01]}(z_0-l)} \left[ \frac{1}{2\sqrt{\beta_{[01]}}} \right. \\ &\quad \left. \times \int_l^{z_0} \sqrt{\beta_{[\rho N]}} g(z) e^{j\int_l^z (\beta_{[\rho N]} - \beta_{[01]}) d\zeta} dz \right], \\ \therefore S_{[01]}^{[MN]} &= e^{j\beta_{[01]}(z_0-l)} \frac{1}{2\sqrt{\beta_{[01]}}} \\ &\quad \times \int_l^{z_0} \sqrt{\beta_{[\rho N]}} g(z) e^{j\int_l^z (\beta_{[\rho N]} - \beta_{[01]}) d\zeta} dz. \end{aligned} \quad (26)$$

$\{S_{[01]}^{[MN]}\}^2$  is the power of the  $TE_{01}$  mode which is generated while the  $TE_{MN}$  mode of unit power passes through the transducer from the circular guide to the rectangular guide.

### $TE_{01}$ Mode Generated from $TM_{MN}$ Mode

In a manner similar to that shown in the previous section, we get an inhomogeneous differential equation concerning  $I_{[01]}$ :

$$\frac{d^2 I_{[01]}}{dz^2} + \frac{1}{z} \frac{dI_{[01]}}{dz} + \beta_{[01]}^2 I_{[01]} = V_{(MN)} H \quad (27)$$

where

$$\begin{aligned} H &= \frac{1}{j\omega\mu} \left[ \beta_{[01]}^2 h_1 + \omega^2 \mu \varepsilon h_2 \right], \\ h_1 &= \chi_{(\rho N)}^2 \frac{1}{B} \iint \tau r T_{(MN)} \frac{\partial T_{[01]}}{\partial r} r dr d\tau, \\ h_2 &= \frac{1}{B} \iint \tau \frac{\partial T_{(MN)}}{\partial r} \frac{\partial T_{[01]}}{\partial r} r dr d\tau \left[ 1 - \frac{3\chi_{(\rho N)}^2}{\omega^2 \mu \varepsilon} \right] \\ &\quad + \frac{1}{B} \iint \tau r \frac{\partial^2 T_{(MN)}}{\partial r^2} \frac{\partial T_{[01]}}{\partial r} r dr d\tau \left[ 1 - \frac{\chi_{(\rho N)}^2}{\omega^2 \mu \varepsilon} \right], \\ V_{(MN)} &= \sqrt{\frac{B}{z}} \sqrt{\frac{\beta_{(\rho N)}}{\omega\varepsilon}} e^{j\beta_{(\rho N)}z} dz \\ I_{[01]} &= -S_{[01]} \sqrt{\frac{B}{z}} \sqrt{\frac{\beta_{[01]}}{\omega\mu}} e^{j\beta_{[01]}z}. \end{aligned} \quad \left. \begin{array}{l} \\ \\ \\ \end{array} \right\} \text{(See Appendix)}$$

Solving Eq. (27), we obtain

$$\begin{aligned} I_{[01]} &= \sqrt{\frac{B}{z}} \sqrt{\frac{\beta_{[01]}}{\omega\mu}} e^{j\beta_{[01]}(z_0-l)} \left[ \frac{1}{j2\beta_{[01]}^{3/2} \sqrt{\omega^2 \mu \varepsilon}} \right. \\ &\quad \left. \times \int_l^{z_0} \sqrt{\beta_{(\rho N)}} (\omega\mu H) e^{j\int_l^z (\beta_{(\rho N)} - \beta_{[01]}) d\zeta} dz \right] \\ S_{[01]}^{(MN)} &= e^{j\beta_{[01]}(z_0-l)} \frac{1}{2\beta_{[01]}^{3/2} \sqrt{\omega^2 \mu \varepsilon}} \\ &\quad \times \int_l^{z_0} \sqrt{\beta_{(\rho N)}} [\beta_{[01]}^2 h_1 \\ &\quad + \omega^2 \mu \varepsilon h_2] e^{j\int_l^z (\beta_{(\rho N)} - \beta_{[01]}) d\zeta} dz. \end{aligned} \quad (28)$$



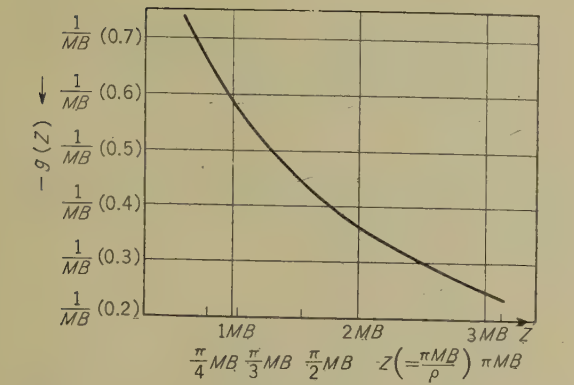


Fig. 4—Universal curve of  $g(z)$  for  $TE_{M1}$  wave.

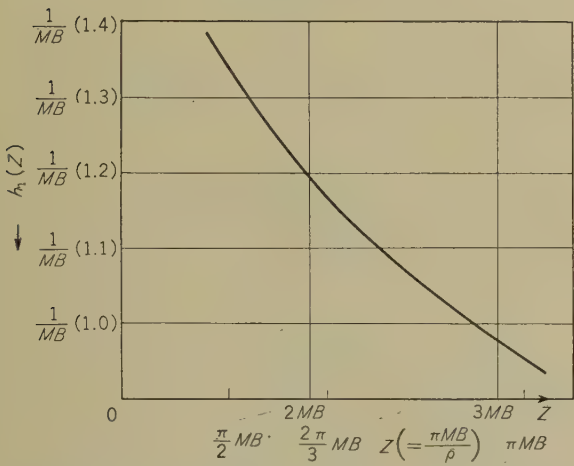


Fig. 5—Universal curve of  $h_1(z)$  for  $TM_{M1}$  wave.

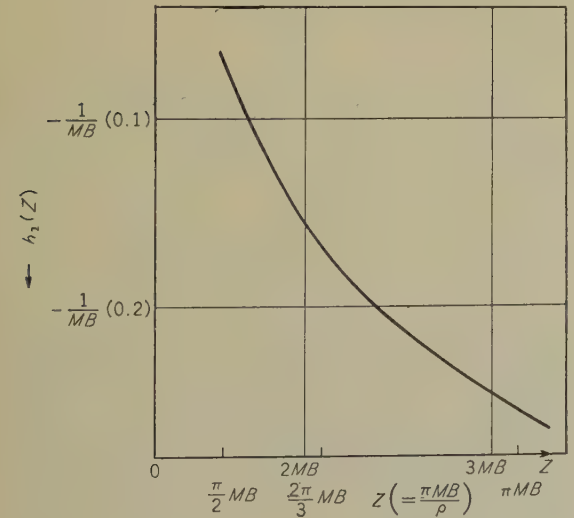


Fig. 6—Universal curve of  $h_2(z)$  for  $TM_{M1}$  wave.

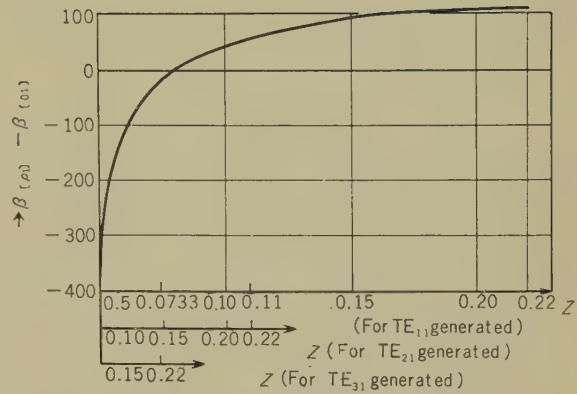


Fig. 7— $\beta_{[\rho]} - \beta_{[01]}$ :  $z$  for 22.2 mm inside diameter 220 mm length transducer (24 kMc).

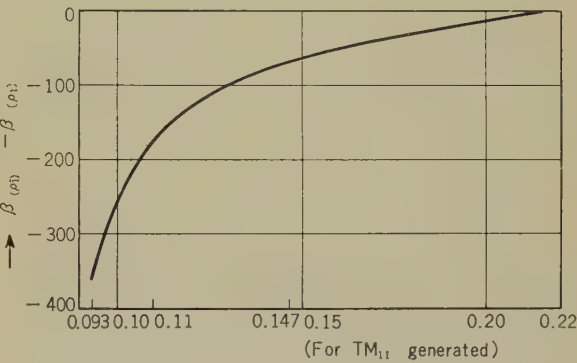


Fig. 8— $\beta_{[\rho]} - \beta_{[01]}$ :  $z$  for 22.2 mm inside diameter 220 mm length transducer (24 kMc).

$\{S^{(MN)}_{[01]}\}^2$  is the power of the  $TE_{01}$  wave which is generated while the  $TM_{MN}$  wave of unit power passes through the transducer from the circular guide to the rectangular guide.

6. Numerical Calculation of Integral Form

Calculations are made of the magnitudes of the unused  $TE_{11}$ ,  $TE_{21}$ ,  $TE_{31}$ , and  $TM_{11}$  waves which are generated at 24 kMc in our transducer whose inside diameter is 22.2 mm and whose length is 220 mm. Integrations

are made numerically by the Simpson method. The results obtained are shown in Table 1.

Table 1

	TE <sub>11</sub>	TE <sub>21</sub>	TE <sub>31</sub>	TM <sub>11</sub>
Generated Power (dB)	-15	-17.5	-33	-17

### 7. Comparison with Measured Magnitudes

The magnitudes of unused modes in the 24 kMc band are measured with Miller's coupled wave transducers.<sup>(3)</sup> Though the transducers used for the measurement were fairly good, the error of this measurement cannot be reduced below 1 dB for the unused modes at a level of about -20 dB. Measured magnitudes of unused TE<sub>11</sub>, TE<sub>21</sub>, TE<sub>31</sub>, and TM<sub>11</sub> waves agree with calculated values almost within 1 dB.

### Conclusion

It is experimentally known even when it is made with precision and has good conduction, the TE<sub>01</sub> mode transducer of this type generates unused modes.

The author accounted for the cause of mode conversion, which had not yet been known.

### Acknowledgement

The author is indebted to I. Someya, Y. Nakamura, T. Miwa, and B. Oguchi of the Laboratory for helpful suggestions relating to this work.

### References

- (1) J. A. Stratton, *Electromagnetic Theory*, McGraw Hill, New York, pp. 38-47, 1941.
- (2) S. A. Schelkunoff, "Generalized Telegraphist's Equations for Waveguides," *Bell Syst. Tech. J.*, **31**, 4, pp. 784-801, July 1952.
- (3) S. E. Miller, "Coupled Wave Theory and Waveguide Applications," *Bell Syst. Tech. J.*, **33**, 3, pp. 661-719, May 1954.

## Appendix

### 1. Electric and Magnetic Fields in Sector Waveguide

#### 1.1 TE Wave

Only the waves coupled with the TE<sub>01</sub> wave are described here.

$$T = J_p(\chi r) \cos p\phi$$

$$E_r = \frac{\partial T}{r \partial \phi} = -\frac{1}{r} J_p(\chi r) (\sin p\phi) p$$

$$E_\phi = \frac{\partial T}{\partial r} = -\chi J_p'(\chi r) (\cos p\phi)$$

$$E_r = 0 \quad \text{in} \quad \phi = \pm \psi \quad \therefore \sin p\phi = 0.$$

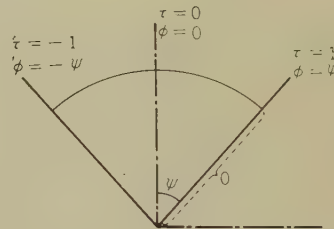


Fig. 9—Cross-section of a sector waveguide.

Hence

$$p = m\pi/\psi. \quad (m=0, 1, 2, \dots) \quad (\text{A-1})$$

Next

$$E_\phi = 0 \quad \text{in} \quad r=a, \quad \therefore J_p'(\chi a) = 0.$$

Hence  $\chi a$  is the zero of  $J_p'$ . Here

$$\left. \begin{aligned} p &= m\pi/\psi = m\pi B/z \\ p\phi &= m\pi\tau. \end{aligned} \right\} \quad (\text{A-2})$$

Normalizing  $T_{[mn]}$  by the factor determined from

$$\chi^2_{[pn]} \int_{-1}^1 \int_0^a T^2_{[mn]} r dr d\tau = 1,$$

we obtain Eq. (4).

#### 1.2 TM Wave

Only the waves coupled with the  $TE_{01}$  wave are described here.

$$T = J_p(\chi_{(pn)}y) \sin p\phi.$$

Here  $\chi_{(pn)}a$  is the  $n$ -th zero of  $J_p$ . In this case, we also obtain the following formulas.

$$p = m\pi/\phi = m\pi B/z, \quad p\phi = m\pi\tau.$$

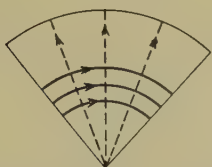


Fig. 10— $T_{[01]} = J_0(\chi_{[01]}r)$ .



Fig. 11— $T_{[11]} = J_p(\chi_{[p1]}r) \cos \pi\tau$ .



Fig. 12— $T_{(11)} = J_p(\chi_{(p1)}r) \sin \pi\tau$ .

Normalizing  $T_{(mn)}$  by the factor determined from

$$\chi_{(pn)}^2 \int_{-1}^1 \int_0^a T_{(mn)}^2 r dr d\tau = 1,$$

we obtain Eq. (5). Figs. 10, 11, and 12 are the patterns of the electric and magnetic fields, which show  $T_{[01]} = J_0(\chi_{[01]}r)$ ,  $T_{[11]} = J_p(\chi_{[p1]}r) \times \cos \pi\tau$ , and  $T_{(11)} = J_p(\chi_{(p1)}r) \sin \pi\tau$  respectively.

## 2. V and I

### 2.1 TE Wave

Rewriting Eqs. (18) and (22) of Section 4, omitting subscripts  $[MN]$  and  $[\rho N]$ , we obtain

$$\left. \begin{aligned} \frac{dV}{dz} + j\omega\mu I + b(z)V &= 0 \\ \frac{dI}{dz} - \frac{\beta^2}{j\omega\mu} V + f(z)I &= Fe^{\pm j\beta_{[01]}z}, \end{aligned} \right\} \quad (A-3)$$

where

$$\left. \begin{aligned} b(z) &= \frac{1}{z} \iint \left[ \frac{\partial T}{\partial r} \right]^2 r dr d\tau \\ f(z) &= -\frac{2}{z} \iint \tau \frac{\partial^2 T}{\partial \tau \partial z} \frac{\partial T}{\partial z} r dr d\tau \\ &= -\frac{1}{\chi_{[p1]}} \frac{d\chi_{[p1]}}{dz} \\ b(z) + f(z) &= \frac{1}{z} - {}^2\chi_{[01]} I_{[01]} \frac{1}{B} \\ &\times \iint \tau r T_{[01]} \frac{\partial T}{\partial z} r dr d\tau = Fe^{\pm j\beta_{[01]}z}. \end{aligned} \right\} \quad (A-4)$$

Substituting  $I$ , which is obtained from the first equation of (A-3), in the second equation, we get

$$\begin{aligned} \frac{d^2 V}{dz^2} + \frac{1}{z} \frac{dV}{dz} + \left\{ \beta^2 + f(z)b(z) + \frac{db}{dz} \right\} V &= \frac{Fe^{j\beta_{[01]}z}}{Fe^{-j\beta_{[01]}z}}. \end{aligned} \quad (A-5)$$

The homogeneous equation of (A-5) is

$$\frac{d^2 V}{dz^2} + \frac{1}{z} \frac{dV}{dz} + \left\{ \beta^2 + f(z)b(z) + \frac{db}{dz} \right\} V = 0. \quad (A-6)$$

### Electric Field

Changing the form of (A-6), we get

$$\frac{d^2 V}{dz^2} + \frac{1}{z} \frac{dV}{dz} + Q(z)V = d(z)V, \quad (A-7)$$



where

$$\left. \begin{aligned} Q(z) &= \beta^2 + \frac{1}{2} \frac{1}{\beta} \frac{d^2 \beta}{dz^2} \\ &\quad - \frac{3}{4} \frac{1}{\beta^2} \left( \frac{d\beta}{dz} \right)^2 - \frac{1}{4} \frac{1}{z^2} \\ d(z) &= \frac{1}{2} \frac{1}{\beta} \frac{d^2 \beta}{dz^2} - \frac{3}{4} \frac{1}{\beta^2} \left( \frac{d\beta}{dz} \right)^2 \\ &\quad - \frac{1}{4} \frac{1}{z^2} - f(z)b(z) - \frac{db}{dz} \end{aligned} \right\} \quad (\text{A-8})$$

The solutions  $V_0$  of the homogeneous equation of (A-7) are  $\beta^{-1/2} z^{-1/2} e^{\pm j f \beta dz}$ . We can solve (A-7) by approximation when  $d(z)$  in the right side is very much smaller than  $Q(z)$  in the left side. At first we write (A-7) in the following form:

$$\frac{d^2 V}{dz^2} + \frac{1}{z} \frac{dV}{dz} + Q(z)V = \varepsilon d(z)V.$$

Substituting  $V = V_0 + \varepsilon V_1$  in the above equation, we get

$$\begin{aligned} \frac{d^2 V_0}{dz^2} + \frac{1}{z} \frac{dV_0}{dz} + Q(z)V_0 + \varepsilon \left[ \frac{d^2 V_1}{dz^2} \right. \\ \left. + \frac{1}{z} \frac{dV_1}{dz} + Q(z)V_1 \right] = \varepsilon d(z)[V_0 + \varepsilon V_1]. \end{aligned}$$

Therefore:

$$\frac{d^2 V_1}{dz^2} + \frac{1}{z} \frac{dV_1}{dz} + Q(z)V_1 = d(z)V_0.$$

We get  $V_1$  from the above equation, and the approximate solutions of (A-7) are

$$V \approx \beta^{-1/2} z^{-1/2} e^{\pm j f \beta dz} \left[ 1 \mp \frac{j}{2} \int \frac{d(z)}{\beta} dz \right]. \quad (\text{A-9})$$

Hence, in the area where  $\left| \frac{j}{2} \int \frac{d(z)}{\beta} dz \right| \ll 1$ , we

have

$$V \approx \beta^{-1/2} z^{-1/2} e^{\pm j f \beta dz}. \quad (\text{A-10})$$

Wave Admittance

From the first equation of (A-3),

$$I = -\frac{1}{j\omega\mu} \left\{ \frac{dV}{dz} + b(z)V \right\}. \quad (\text{A-11})$$

Substituting (A-10) in (A-11), we get

$$\left. \begin{aligned} Y = \frac{I}{V} &= \mp \frac{\beta}{\omega\mu} [1 \pm j\delta_1] \\ \text{where} \\ \delta_1 &= \frac{1}{2} \frac{1}{\beta z} + \frac{1}{2} \frac{1}{\beta^2} \frac{d\beta}{dz} - \frac{b(z)}{\beta} \end{aligned} \right\}$$

In the area where  $\delta_1 \ll 1$ , we obtain

$$Y \approx \mp \frac{\beta}{\omega\mu}$$

therefore:

$$I = \mp \frac{\beta}{\omega\mu} V = \mp \frac{1}{\omega\mu} \beta^{1/2} z^{-1/2} e^{\pm j f \beta dz}.$$

$V$  and  $I$  of unit power:

$$\left. \begin{aligned} V &= \sqrt{\frac{B}{z}} \sqrt{\frac{\omega\mu}{\beta}} e^{\pm j f \beta dz} \\ I &= \mp \sqrt{\frac{B}{z}} \sqrt{\frac{\beta}{\omega\mu}} e^{\pm j f \beta dz} \end{aligned} \right\} \quad (\text{A-12})$$

## 2.2 TM Wave

In the same manner as with the TE wave, we get

$$\left. \begin{aligned} V &= \sqrt{\frac{B}{z}} \sqrt{\frac{\beta}{\omega\varepsilon}} e^{\pm j f \beta dz} \\ I &= \mp \sqrt{\frac{B}{z}} \sqrt{\frac{\omega\varepsilon}{\beta}} e^{\pm j f \beta dz} \end{aligned} \right\} \quad (\text{A-13})$$

\* \* \* \*

# Magnetic Gate Circuits Controlled by High Frequency Signals\*

Ichiro ENDO† and Kikunobu KUSUNOKI‡

*In a transformer in which a magnetic core is used, the relation between the output voltage and the input current is not linear. By arranging three or four cores having such nonlinear properties, and by choosing the number of turns and the direction of each core winding properly, a gate circuit controlled by high frequency signals is obtained. The gate circuits are inserted between parametron circuits for the purpose of economizing the circuit elements.*

*The principles and the experimental results of a three-core gate circuit, a four-core gate circuit (or triple balance modulator), and their applications are described in this paper.*

## Introduction

Recently, the parametron in which nonlinear magnetic cores are used is being widely applied in the logical circuits of electronic computers and in electronic telephone exchanges. The input and output currents of the parametron are high frequency signals, but it is often desirable to obtain ON-OFF output signals. In this case, the method of superposing the output signal of the parametron itself, or of using a special type of parametron (a flip-flop parametron) is often adopted. The gate circuit described here is another type of ON-OFF circuit. By using nonlinear cores, the input signal is gated by a high frequency signal or by a parametron signal. The features of the circuit are low power consumption, high speed, and simplicity.

## 1. Core Characteristics

### 1.1. Analysis

The relation between the magnetic flux

density ( $B$ ) and the magnetic field intensity ( $H$ ) of the ferromagnetic core in the unsaturated region is well-known as Rayleigh's formula. It is required, however, to generalize the formula for application to all types of magnetic cores.

If the maximum magnetic field intensity ( $H_m$ ) is small, the flux density is not saturated. The magnetization curve is as shown in Fig. 1. Here, the inclination of the curve ( $\tan \theta$ ) tends to increase as  $H_m$  increases, and the relation between  $B$  and  $H$  is given in the following relation.

$$B = (\alpha_1 + \alpha_2 H_m + \alpha_3 H_m^2 + \dots) H \pm \gamma (H_m^p - |H|^p) \quad (1)$$

where,  $\alpha_1, \alpha_2, \dots$  and  $\gamma$  are coefficients related to the material of the core. As usual,  $p$  is approximately 2. Now assume  $H = H_m \cos \omega t$ , and the flux densities, for  $t = 0 \sim \pi/\omega$ , are given from Eq. (1);

$$B(t) = (\alpha_1 + \alpha_2 H_m + \alpha_3 H_m^2 + \dots) H_m \cos \omega t + \gamma H_m^2 (1 - \cos^2 \omega t),$$

and for  $t = \pi/\omega \sim 2\pi/\omega$ ,

$$B(t) = (\alpha_1 + \alpha_2 H_m + \alpha_3 H_m^2 + \dots) H_m \cos \omega t$$

\* MS in Japanese received by the Electrical Communication Laboratory, Feb. 28, 1959. Originally published in the *Kenkyū Zituyōka Hōkoku (Electrical Communication Laboratory Technical Journal)*, N.T.T., Vol. 8, No. 7, pp. 1079-1087.

† Electronics Research Section.

‡ Switching Research Section.

$$-\gamma H_m^2(1 - \cos^2 \omega t).$$

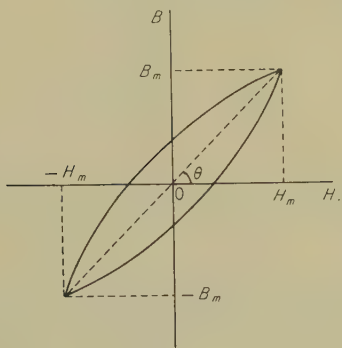


Fig. 1—Magnetization curve of a ferromagnetic core in the unsaturated region.

Expanding these functions into a Fourier series, we may write

$$B(t) = (\alpha_1 + \alpha_2 H_m + \alpha_3 H_m^2 + \dots) H_m \cos \omega t + (8\gamma H_m^2 / \pi) (\sin \omega t / 3 - \sin 3\omega t / 1.5 - \sin 5\omega t / 3.5 - \dots).$$
 (2)

Then, the electromotive force (e.m.f.) induced across the secondary winding shown in Fig. 2 is given by

$$e = kn \, dB/dt,$$

where *k* is constant; hence, from Eq. (2), the following equation can be obtained:

$$e = -kn\omega \{ (\alpha_1 + \alpha_2 H_m + \alpha_3 H_m^2 + \dots) H_m \sin \omega t - (8\gamma H_m^2 / \pi) (\cos \omega t / 3 - \cos 3\omega t / 1.5 - \cos 5\omega t / 3.5 - \dots) \}.$$

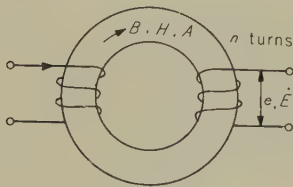


Fig. 2—Core winding.

If the higher harmonics are neglected, the next relation can be found:

$$e \doteq -kn\omega \{ (\alpha_1 + \alpha_2 H_m + \alpha_3 H_m^2 + \dots) H_m \sin \omega t - 8\gamma H_m^2 \cos \omega t / 3\pi \} = -kn\omega \{ (\alpha_1 + \alpha_2 H_m + \alpha_3 H_m^2 + \dots)^2 + (8\gamma H_m / 3\pi)^2 \}^{1/2} H_m \cos \{ \pi/2 - (\omega t - \varphi) \},$$
 (3)

where

$$\varphi = \tan^{-1} 8\gamma H_m / 3\pi (\alpha_1 + \alpha_2 H_m + \alpha_3 H_m^2 + \dots)$$

and  $\varphi$  is the phase delay of the e.m.f. due to the hysteresis loss.

Since the shape of the hysteresis loop is determined by the value of *H<sub>m</sub>*,  $\gamma$  of a given core is also found as a function relating to *H<sub>m</sub>*. The amplitude and the phase of *e* in Eq. (3), therefore, are decided uniquely by *H<sub>m</sub>*.

In the above description, it is assumed that *p*=2 for simplification, but even for other values of *p* the fundamental component of *e* is given as a function of *H<sub>m</sub>* only.

Thus, on the assumption that  $\dot{E}$  is the vector indication for the fundamental component of the e.m.f. induced in the secondary winding per unit turn (see Fig. 2.),  $\dot{E}$  can be expressed generally as follows for the arbitrary value of the input ampere-turns *A* (root mean square value: r.m.s.):

$$\dot{E}(A) = E_m(|A|) \exp [j \{ \pi/2 - \varphi(|A|) \}] A/|A|$$
 (4)

Here, *E<sub>m</sub>* and  $\varphi$  are functions of the absolute value of *A*, the former being the amplitude (r.m.s.) and the latter being the phase delay due to the hysteresis loss. Moreover, the coefficient *A*/*|A|* means that  $\dot{E}$  is reversed by inverting the polarity of *A*. Thus, Eq. (4) is the function characterizing the properties of the core.

1.2. Characteristics of Ferrite-core Type *L<sub>2</sub>D<sub>4</sub>* (a toroidal core whose outer diameter is 4 mm, whose inner diameter is 2 mm, and whose thickness is 1 mm)



Some non-uniformity is found in the characteristics of  $E_m$  and  $\varphi$  among cores of the same type. Representative values which were measured in the circuit of Fig. 2 are shown in Fig. 3. The frequency of measurement was 1 Mc/s.

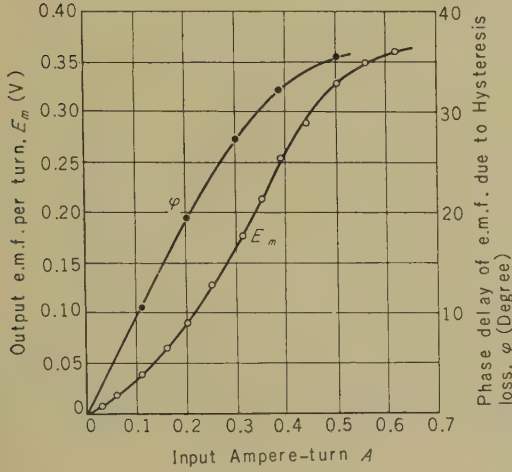


Fig. 3—Characteristics of ferrite-core type L<sub>2</sub>D<sub>4</sub>.

## 2. Gate Circuit with Three Cores

### 2.1. Principle

In Fig. 4, on the assumption that  $\dot{E}_1$ ,  $\dot{E}_2$  and  $\dot{E}_3$  are respectively the vectors of the fundamental component of the e.m.f. per number of turns  $T_i$  for each core, the following equations are obtained:

$$\dot{E}_1 = E_m(|A_i + A_g|) \exp[j\{\pi/2 - \varphi(|A_i + A_g|)\}] (A_i + A_g) / |A_i + A_g|,$$

$$\dot{E}_2 = E_m(|A_i - A_g|) \exp[j\{\pi/2 - \varphi(|A_i - A_g|)\}] (A_i - A_g) / |A_i - A_g|,$$

$$\dot{E}_3 = E_m(|A_i|) \exp[j\{\pi/2 - \varphi(|A_i|)\}] A_i / |A_i|.$$

Then the total e.m.f.  $\dot{E}_0$  is given as

$$\dot{E}_0(A_i, A_g) = \dot{E}_1 + \dot{E}_2 - 2\dot{E}_3$$

$$\begin{aligned} &= E_m(|A_i + A_g|) \exp[j\{\pi/2 - \varphi(|A_i + A_g|)\}] (A_i + A_g) / |A_i + A_g| \\ &+ E_m(|A_i - A_g|) \exp[j\{\pi/2 - \varphi(|A_i - A_g|)\}] (A_i - A_g) / |A_i - A_g| \\ &- 2E_m(|A_i|) \exp[j\{\pi/2 - \varphi(|A_i|)\}] A_i / |A_i|. \end{aligned}$$

From the above equations, the following relations are obtained:

1) Inverting the sign of  $A_i$ , we have

$$\begin{aligned} \dot{E}_0(-A_i, A_g) &= E_m(|-A_i + A_g|) \exp[j\{\pi/2 - \varphi(|-A_i + A_g|)\}] (-A_i + A_g) / |-A_i + A_g| \\ &+ E_m(|-A_i - A_g|) \exp[j\{\pi/2 - \varphi(|-A_i - A_g|)\}] (-A_i - A_g) / |-A_i - A_g| \\ &- 2E_m(|-A_i|) \exp[j\{\pi/2 - \varphi(|-A_i|)\}] \times (-A_i) / |-A_i| = -\dot{E}_0(A_i, A_g). \end{aligned}$$

2) Assuming  $A_i = 0$ , we get

$$\begin{aligned} \dot{E}_0(0, A_g) &= E_m(|A_g|) \exp[j\{\pi/2 - \varphi(|A_g|)\}] A_g / |A_g| + E_m(|-A_g|) \exp[j\{\pi/2 - \varphi(|-A_g|)\}] (-A_g) / |-A_g| = 0. \end{aligned}$$

3) Inverting the sign of  $A_g$ , we have

$$\begin{aligned} \dot{E}_0(A_i, -A_g) &= E_m(|A_i - A_g|) \exp[j\{\pi/2 - \varphi(|A_i - A_g|)\}] (A_i - A_g) / |A_i - A_g| \\ &+ E_m(|A_i + A_g|) \exp[j\{\pi/2 - \varphi(|A_i + A_g|)\}] \times (A_i + A_g) / |A_i + A_g| - 2E_m(|A_i|) \exp[j\{\pi/2 - \varphi(|A_i|)\}] A_i / |A_i| = \dot{E}_0(A_i, A_g). \end{aligned}$$

4) Assuming  $A_g = 0$ , we get

$$\begin{aligned} \dot{E}_0(A_i, 0) &= E_m(|A_i|) \exp[j\{\pi/2 - \varphi(|A_i|)\}] A_i / |A_i| + E_m(|A_i|) \exp[j\{\pi/2 - \varphi(|A_i|)\}] A_i / |A_i| - 2E_m(|A_i|) \exp[j\{\pi/2 - \varphi(|A_i|)\}] A_i / |A_i| = 0. \end{aligned}$$

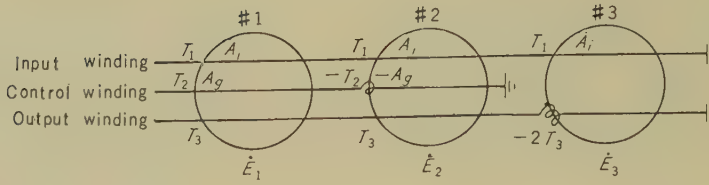


**Fig. 4**—Gate circuit in which three cores are used. ( $T$ : number of turns; minus signs meaning reverse winding direction.)

$$-\varphi(|A_i|) \} A_i/|A_i| - 2E_m(A_i) \exp[j\{\pi/2$$

$$-\varphi(|A_i|) \} A_i/A_i = 0.$$

It is found that when  $A_g \neq 0$ , the sign of  $\dot{E}$  varies according to that of  $A_i$ , whatever value the sign  $A_g$  takes, and that when  $A_g = 0$ ,  $\dot{E}_0$  becomes zero.

Thus, the input current ( $A_i$ ) can be gated by the amplitude of the controlling current ( $A_g$ ).

As shown in the above analysis, for the realization of the gate circuit it is required only that each core must have the uniform characteristics shown in Fig. (4), and that the function form about  $E_m$  and  $\varphi$  may be arbitrary.

However, as high output voltage is desirable, the nonlinearity of  $E_m$  against  $A$  should be great.

Now assume that  $A$  is small and  $\varphi$  is negligible (as the case when  $A$  is less than 0.15 AT for the core shown in Fig. 3). For convenience, we consider cores a characteristic of which is that  $E_m(|A|)A/|A|$  can be approximated by the first and the third order terms on  $A$ , and let  $A_i$  and  $A_g$  be a signal of the same or of the opposite phase.

Then

$$\dot{E}(A) = j(\beta_1 A + \beta_3 A^3),$$

where  $\beta_1$  and  $\beta_3$  are coefficients, and the second order coefficient  $\beta_2$  is negligible.

And we have

$$\dot{E}_1 = j\{\beta_1(A_i + A_g) + \beta_3(A_i + A_g)^3\},$$

$$\dot{E}_2 = j\{\beta_1(A_i - A_g) + \beta_3(A_i - A_g)^3\},$$

$$\dot{E}_3 = j(\beta_1 A_i + \beta_3 A_i^3).$$

Since these are all same-phase signals, the total e.m.f. per turn is written as

$$\dot{E}_0 = \dot{E}_1 + \dot{E}_2 - 2\dot{E}_3 = j6\beta_3 A_i A_g^2. \quad (5)$$

## 2.2. Experimental Results

In the circuit of Fig. 4, three  $L_2D_4$  cores are used, and the number of turns  $T_1 = T_2 = T_3 = 2$ . The frequency of measurement is 1 Mc/s.

The non-uniformity of the characteristics of cores are approximately within 10 %, and the mean values of  $\beta_1$  and  $\beta_3$  are 0.32 and 26.7 respectively. The phases of the input current and the control current are held either at 0 or at  $\pi$  phase. The output load impedance is 2 k $\Omega$ . If the load impedance is larger than several hundred ohms, the output voltage is almost constant.

From Eq. (5), the calculated output e.m.f. is obtained as

$$\begin{aligned} V_0 &= -j\dot{E}_0 \times 2 = 6\beta_3 A_i A_g^2 \times 2 \\ &= 6 \times 26.7 \times 2 A_i A_g^2 = 32 A_i A_g^2. \end{aligned} \quad (6)$$

The results of measurements are shown in Fig. 5. Here S/N is the ratio of output voltage when  $A_g \neq 0$  to  $A_g = 0$  for a constant value of  $A_i$ .

It is found that the relation of phases between  $A_i$ ,  $A_g$ , and  $V_0$  is shown precisely by Eq. (6).

The difference between measured and calculated values in Fig. 5 seems to occur due to the non-uniformity of  $\beta_3$  of the cores, and the omission of the  $\beta_2$  term. And the larger

difference in the region of small  $A_g$  seems due to the comparatively larger leakage in the unbalance of the characteristics of cores.

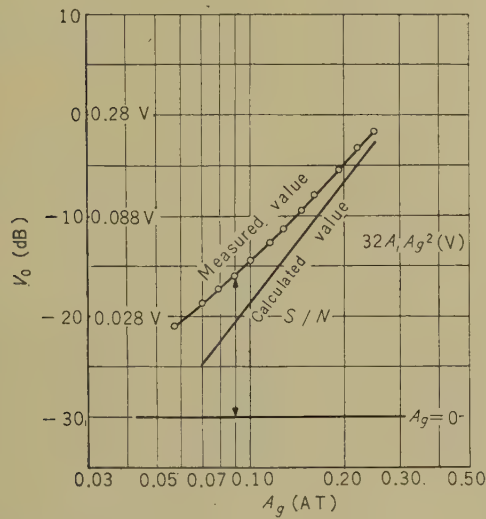


Fig. 5—Characteristics of gate circuit in which three cores are used.  $A_i=0.100$  AT.

3. Triple Balance Modulator (T.B.M.)

3.1. Principle

On the assumption that the vector of the fundamental component of each core e.m.f. per turn in Fig. 6 is  $\dot{E}_1, \dot{E}_2, \dot{E}_3$  and  $\dot{E}_4$ , the total e.m.f.  $\dot{E}_0$  is calculated as

$$\begin{aligned} \dot{E}_0(A_1, A_2, A_3) &= \dot{E}_1 + \dot{E}_2 + \dot{E}_3 + \dot{E}_4 \\ &= E_m(|A_1 + A_2 + A_3|) \exp\left\{j\left\{\frac{\pi}{2} - \varphi(|A_1 + A_2 + A_3|)\right\}\right\} \frac{(A_1 + A_2 + A_3)}{|A_1 + A_2 + A_3|} \\ &\quad + E_m(|A_1 - A_2 - A_3|) \exp\left\{j\left\{\frac{\pi}{2} - \varphi(|A_1 - A_2 - A_3|)\right\}\right\} \frac{(A_1 - A_2 - A_3)}{|A_1 - A_2 - A_3|} \\ &\quad + E_m(|-A_1 + A_2 + A_3|) \exp\left\{j\left\{\frac{\pi}{2} - \varphi(|-A_1 + A_2 + A_3|)\right\}\right\} \frac{(-A_1 + A_2 + A_3)}{|-A_1 + A_2 + A_3|} \\ &\quad + E_m(|-A_1 - A_2 + A_3|) \exp\left\{j\left\{\frac{\pi}{2} - \varphi(|-A_1 - A_2 + A_3|)\right\}\right\} \frac{(-A_1 - A_2 + A_3)}{|-A_1 - A_2 + A_3|} \end{aligned}$$

Now

- 1) Suppose either  $A_1, A_2$ , or  $A_3$  is zero as before. Then the following relation is obtained:

$$\begin{aligned} \dot{E}_0(0, A_2, A_3) &= \dot{E}_0(A_1, 0, A_3) \\ &= \dot{E}_0(A_1, A_2, 0) = 0. \end{aligned}$$

- 2) Suppose the sign of either  $A_1, A_2$  or  $A_3$  is inverted. Then the following relation is obtained:

$$\begin{aligned} \dot{E}_0(-A_1, A_2, A_3) &= \dot{E}_0(A_1, -A_2, A_3) \\ &= \dot{E}_0(A_1, A_2, -A_3) \\ &= -\dot{E}_0(A_1, A_2, A_3). \end{aligned}$$

Thus, in this case, too, one signal can be gated by another signal, and this relation may be utilized as a full adder.

If the above 4 cores are used, and  $A_1, A_2$  and  $A_3$  are held in the same or the opposite phase, then the output e.m.f. per turn for each core is

$$\begin{aligned} \dot{E}_1 &= j\{\beta_1(A_1 + A_2 + A_3) + \beta_3(A_1 + A_2 + A_3)^3\}, \\ \dot{E}_2 &= j\{\beta_1(A_1 - A_2 - A_3) + \beta_3(A_1 - A_2 - A_3)^3\}, \\ \dot{E}_3 &= j\{\beta_1(-A_1 + A_2 - A_3) + \beta_3(-A_1 + A_2 - A_3)^3\}, \\ \dot{E}_4 &= j\{\beta_1(-A_1 - A_2 + A_3) + \beta_3(-A_1 - A_2 + A_3)^3\}. \end{aligned}$$

Therefore

$$\dot{E}_0 = \dot{E}_1 + \dot{E}_2 + \dot{E}_3 + \dot{E}_4 = j24\beta_3 A_1 A_2 A_3.$$

3.2. Experimental Results

Let  $T_1 = T_2 = T_3 = 2$  and  $T_4 = 6$ . Then the output voltage



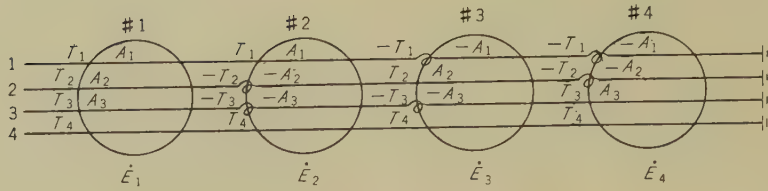


Fig. 6—Triple balance modulator.

$$V_0 = -j\dot{E}_0 = 24 \beta_3 A_1 A_2 A_3 \times 6$$

$$= 385 A_1 A_2 A_3.$$

And on the assumption  $|A_1|=|A_2|=|A_3|$ , the following relation is obtained:

$$V_0 = 385 A_1^3.$$

The result of measurements is shown in Fig. 7. Here  $V_0$  is the output voltage across the load impedance of 2 kΩ.

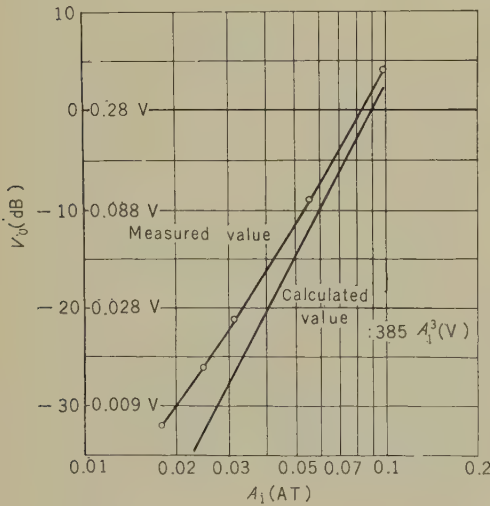


Fig. 7—Characteristics of triple balance modulator ( $|A_1|=|A_2|=|A_3|$ ).

When  $|A_1|=|A_3|=0.1$  AT, S/N in  $A_2=0$  is 15.6 dB; when  $|A_1|=0.1$  AT, S/N in  $A_2, A_3=0$  is 29.0 dB.

It was found that if the phase of either of  $A_1, A_2$  or  $A_3$  was inverted, the phase of the output voltage was also inverted.

## 4. Full Adder

### 4.1. Principle

By using 3 cores, as shown in Fig. 8, and holding the phase of  $A_1, A_2$  and  $A_3$  in the same or the opposite phase, the fundamental component of each core e.m.f. per turn;  $\dot{E}_1, \dot{E}_2$  and  $\dot{E}_3$ ; may be obtained as follows:

$$\dot{E}_1 = j\{\beta_1(A_1 + A_2 + A_3) + \beta_3(A_1 + A_2 + A_3)^3\},$$

$$\dot{E}_2 = j\{\beta_1(A_1 - A_2 - A_3) + \beta_3(A_1 - A_2 - A_3)^3\},$$

$$\dot{E}_3 = j\{\beta_1(-2A_1) + \beta_3(-2A_1)^3\}.$$

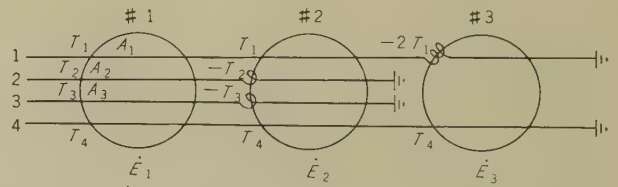


Fig. 8—Full adder.

As a result,

$$\dot{E}_0 = \dot{E}_1 + \dot{E}_2 + \dot{E}_3$$

$$= j6\beta_3 A_1 \{(A_2 + A_3)^2 - A_1^2\}.$$

In the above equation,

when  $A_2 = -A_3$ ,  $\dot{E}_0 = -j6\beta_3 A_1^3$  is obtained;

when  $A_2 = A_3$ ,  $\dot{E}_0 = j6\beta_3 A_1 (4A_2^2 - A_1^2)$ .

Consequently if  $|2A_2| > |A_1|$ , then

$$6\beta_3 (4A_2^2 - A_1^2) > 0.$$

Thus, when  $|A_2|=|A_3|$ , the phase relations between  $A_1, A_2$  and  $A_3$  and the output voltage  $\dot{E}_0$  become as shown in Table 1, and it is found that this relation can be used as a full adder.

Table 1

PHASE RELATION OF FULL ADDER

$A_1$	$A_2$	$A_3$	$-j\dot{E}_0$
0	0	0	0
0	0	$\pi$	$\pi$
0	$\pi$	0	$\pi$
0	$\pi$	$\pi$	0
$\pi$	0	0	$\pi$
$\pi$	0	$\pi$	0
$\pi$	$\pi$	0	0
$\pi$	$\pi$	$\pi$	$\pi$

If  $|A_2|=|A_1|\sqrt{2}$ , the output voltage is  $\dot{E}_0=j6\beta_3A_1^3$  when  $A_2=A_3$ , and it is found that this value has the same amplitude and the opposite phase compared with the above value when  $A_2=-A_3$ .

4.2. Experimental Results

Let  $T_1=3, T_2=T_3=T_4=2$  in Fig. 8 and make each of the input currents equal. Then,

$$A_1=1.5 A_2 .$$

When  $A_2=-A_3$ , therefore, the output voltage becomes

$$V_0 = -j\dot{E}_0 \times 2 = -6\beta_3 A_1^3 \times 2 = -32.0 A_1^3,$$

and when  $A_2=A_3$ , the following relation is obtained:

$$\begin{aligned} V_0 &= 6\beta_3 A_1 \{4 \times (A_1/1.5)^2 - A_1^2\} \times 2 \\ &= 24.8 A_1^3. \end{aligned}$$

The results of measurements are shown in Fig. 9 and Fig. 10. Here  $V_0$  is the output voltage in a load impedance of  $2\text{ k}\Omega$ .

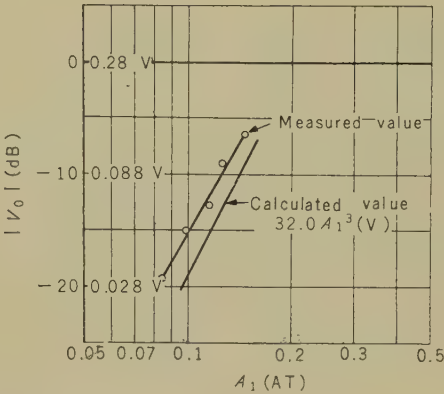


Fig. 9—Characteristics of adder ( $A_2=-A_3$ ).

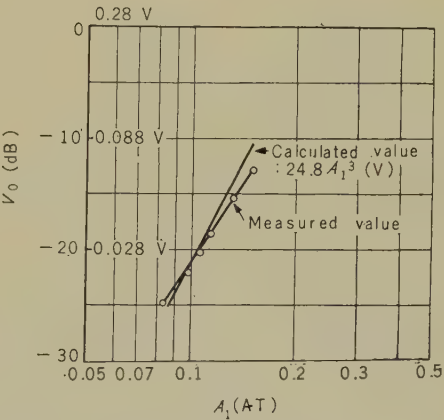


Fig. 10—Characteristics of adder ( $A_2=A_3$ ).

As noted above, if the total ampere-turns in a core are held within 0.15 AT, and the phase delay is almost negligible, then the phase relations were found to be related precisely as shown in Table 1.

Conclusion

Gate circuits in which nonlinear cores are used are described.

The quality of these circuits depend upon the uniformity of the characteristics of cores,

and it is desirable to develop cores with larger nonlinearity and better uniformity.

By using the same cores used for the parametron circuits, we found that gate cir-

cuits having a signal-to-noise ratio of 20 dB were obtained and that their output voltage was sufficient to control the parametrons in the following stage.

\* \* \* \*



# Distributed Amplifier Tube\*

Takuya KOJIMA†

*The distributed amplifier tube, a new type wide band amplifier tube, has been developed. The anode and the grid of this tube are helical lines, and the velocity of propagation of electromagnetic wave on the anode line is equal to that on the grid line. The signal is amplified during its travel from the input of the grid line to the output of the anode line. The theory of amplification and the measured characteristics of two experimental tubes are described. The amplification band of one of the tubes is from zero to 150 Mc.*

## Introduction

Distributed amplifiers make it possible to amplify an extremely wide band signal and many works on distributed amplifiers composed with several ordinary tubes have been carried out.

Distributed amplification in a signal tube is also realizable by arranging transmission-line type electrodes in the tube. Several tubes of this type have been proposed.<sup>(1)(2)</sup> In such a tube the amplification of signal is realized in the same manner as in distributed amplifiers. It is quite possible to construct a tube which has the same gain-band characteristics as that of an amplifier made with many ordinary tubes. Furthermore, as the electrodes of these tubes are made of perfectly distributed lines, there is no limit to the frequency band that can be amplified. A comparison between these special tubes and common distributed amplifiers will be discussed in the Appendix.

In this paper, the theory of the distributed amplifier tube and a method of calculating the characteristics of these tubes which will be useful for designing the tubes are described; and also the experimental results of two experimental tubes are presented.

MKS units are employed throughout this paper.

## 1. Theory of the Distributed Amplifier Tube

The discussion of the principles of this tube, which are identical with that of the common distributed amplifier, will be omitted in this paper. These principles have been presented in reference.<sup>(3)</sup>

The general theory is first described and an analysis of the effects of various factors, line loss, difference of velocities of the two lines, etc.; on tube characteristics is carried out by applying general theory. In the succeeding paragraph, a method for calculating the characteristics of the helical-transmission-line electrode is shown.

### 1.1. General Theory of Amplification

The basic mechanism of amplification of this tube is shown in Fig. 1. A long cathode, a grid line, and an anode line are all parallel from  $z=0$  to  $z=l$ . The electrons leaving the cathode go across the grid line and arrive at the anode line as in the case of the common triode. Now, we consider that the electron path from the cathode to the anode is perpendicular to the axis of electrode lines. The constants of the two lines, grid and anode, are defined as follows:

Series impedance of anode line  $Z_a$

\* MS in Japanese received by the Electrical Communication Laboratory Jan. 14, 1960. Published in the *Kenkyū Zituyōka Hōkoku (Electrical Communication Laboratory Technical Journal)*, N.T.T., Vol. 9, No. 3, pp. 201-244, 1960.

† Electronic Parts Research Section.

Shunt admittance of anode line	$Y_a$
Series impedance of grid line	$Z_g$
Shunt admittance of grid line	$Y_g$
Characteristic impedance of anode line	$Z_{0a} = \sqrt{Z_a/Y_a}$
Characteristic impedance of grid line	$Z_{0g} = \sqrt{Y_g/Z_g}$
Propagation constant of anode line	$\Gamma = \sqrt{Z_a Y_a}$
Propagation constant of grid line	$\gamma = \sqrt{Z_g Y_g}$
Attenuation constant of anode line	$\alpha_a$
Phase constant of anode line	$B_a$
Attenuation constant of grid line	$\alpha_g$
Phase constant of grid line	$B_g$
Density of mutual conductance per unit length of the cathode	$g_m$

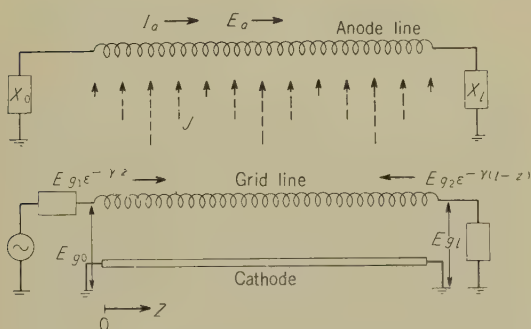


Fig. 1—Principle of amplification.

If an ac signal of amplitude  $E_{g0}$  is applied at the input of the grid line, it will travel on the line in the same manner as on an ordinary transmission line. In general, as the matching of the output termination is not perfect, there will appear two traveling waves, a forward wave and a backward wave. We denote the forward wave and the backward wave as  $E_{g1}\epsilon^{-\gamma z}$  and  $E_{g2}\epsilon^{-\gamma(l-z)}$  respectively, where  $z$  is the distance measured from the input along the line and  $l$  is the total length of the line.

The voltage on the grid line  $E_g$  is:

$$E_g = E_{g1}\epsilon^{-\gamma z} + E_{g2}\epsilon^{-\gamma(l-z)}, \quad (1)$$

and the amplitudes of the input signal  $E_{g0}$

and the output signal  $E_{gl}$  are:

$$\left. \begin{aligned} E_{g0} &= E_{g1} + E_{g2}\epsilon^{-\gamma l} \\ E_{gl} &= E_{g1}\epsilon^{-\gamma l} + E_{g2} \end{aligned} \right\} \quad (2)$$

As the electron currents emitted from the cathode are modulated by the grid-line voltage as in a common triode, the a-c current density per unit length of cathode  $J$  is given by:

$$\begin{aligned} J &= g_m E_g = g_m \{E_{g1}\epsilon^{-\gamma z} + E_{g2}\epsilon^{-\gamma(l-z)}\} \\ &= J_1\epsilon^{-\gamma z} + J_2\epsilon^{\gamma z} \end{aligned} \quad (3)$$

where

$$\left. \begin{aligned} J_1 &= g_m E_{g1} \\ J_2 &= g_m E_{g2}\epsilon^{-\gamma l} \end{aligned} \right\} \quad (4)$$

The anode line of this tube absorbs the modulated electron current throughout its length. In Fig. 1 this current distribution along the anode line is shown. The current-voltage equations of this active transmission line are given by

$$\left. \begin{aligned} -dE_a &= Z_a I_a dz \\ -dI_a &= Y_a E_a dz - J_1\epsilon^{-\gamma z} dz - J_2\epsilon^{\gamma z} dz \end{aligned} \right\} \quad (5)$$

where  $E_a$ : anode line voltage  
 $I_a$ : anode line current.

From Eq. (5), we obtain

$$\left. \begin{aligned} \frac{d^2 E_a}{dz^2} &= \Gamma^2 E_a - \Gamma Z_{0a} J_1 \epsilon^{-\gamma z} - \Gamma Z_{0a} J_2 \epsilon^{\gamma z} \\ \frac{d^2 I_a}{dz^2} &= \Gamma^2 I_a - J_1 \gamma \epsilon^{-\gamma z} + J_2 \gamma \epsilon^{\gamma z} \end{aligned} \right\} \quad (6)$$

The solutions of Eqs. (6) are given by

$$\left. \begin{aligned} E_a &= A_1 \epsilon^{-\Gamma z} + A_2 \epsilon^{\Gamma z} + J_1 \Gamma Z_{0a} \frac{\epsilon^{-\gamma z}}{\Gamma^2 - \gamma^2} \\ &\quad + J_2 \Gamma Z_{0a} \frac{\epsilon^{\gamma z}}{\Gamma^2 - \gamma^2} \end{aligned} \right\} \quad (7)$$

$$I_a = \left. \begin{aligned} & \frac{A_1}{Z_{0a}} \varepsilon^{-\Gamma z} - \frac{A_2}{Z_{0a}} \varepsilon^{\Gamma z} + J_1 \gamma \frac{\varepsilon^{-\Gamma z}}{\Gamma^2 - \gamma^2} \\ & - J_2 \gamma \frac{\varepsilon^{\Gamma z}}{\Gamma^2 - \gamma^2} \end{aligned} \right\}$$

where

$$\Gamma = \sqrt{Z_a Y_a}, \quad Z_{0a} = \sqrt{\frac{Z_a}{Y_a}} \quad (8)$$

$A_1, A_2$  are arbitrary constants.

Let us consider now that the ends of the anode line are terminated with the impedance  $X_0$  at the input and  $X_l$  at the output. With these boundary conditions  $A_1$  and  $A_2$  will be determined. The relations between voltage and current at the ends of the anode line are given by

$$\left. \begin{aligned} -E_a &= X_0 I_a \quad \text{at } z=0 \\ E_a &= X_l I_a \quad \text{at } z=l. \end{aligned} \right\} \quad (9)$$

Substituting Eqs. (9) into (7), we have

$$\left. \begin{aligned} A_1 &= \frac{J_1 \frac{\Gamma Z_{0a}}{\Gamma^2 - \gamma^2} \left\{ \left( 1 + \frac{\gamma X_0}{\Gamma Z_{0a}} \right) \left( 1 + \frac{X_l}{Z_{0a}} \right) \varepsilon^{\Gamma l} - \left( 1 - \frac{\gamma X_l}{\Gamma Z_{0a}} \right) \left( 1 - \frac{X_0}{Z_{0a}} \right) \varepsilon^{\Gamma l} \right\} + J_2 \frac{\Gamma Z_{0a}}{\Gamma^2 - \gamma^2} \left\{ \left( 1 - \frac{\gamma X_0}{\Gamma Z_{0a}} \right) \left( 1 + \frac{X_l}{\Gamma Z_{0a}} \right) \varepsilon^{\Gamma l} - \left( 1 + \frac{\gamma X_l}{\Gamma Z_{0a}} \right) \left( 1 - \frac{X_0}{Z_{0a}} \right) \varepsilon^{\Gamma l} \right\}}{\left( 1 - \frac{X_0}{Z_{0a}} \right) \left( 1 - \frac{X_l}{Z_{0a}} \right) \varepsilon^{-\Gamma l} - \left( 1 + \frac{X_0}{Z_{0a}} \right) \left( 1 + \frac{X_l}{Z_{0a}} \right) \varepsilon^{\Gamma l}} \\ A_2 &= \frac{J_1 \frac{\Gamma Z_{0a}}{\Gamma^2 - \gamma^2} \left\{ \left( 1 + \frac{\gamma X_0}{\Gamma Z_{0a}} \right) \left( 1 - \frac{X_l}{Z_{0a}} \right) \varepsilon^{-\Gamma l} - \left( 1 - \frac{\gamma X_l}{\Gamma Z_{0a}} \right) \left( 1 + \frac{X_0}{Z_{0a}} \right) \varepsilon^{-\Gamma l} \right\} + J_2 \frac{\Gamma Z_{0a}}{\Gamma^2 - \gamma^2} \left\{ \left( 1 - \frac{\gamma X_0}{\Gamma Z_{0a}} \right) \left( 1 - \frac{X_l}{Z_{0a}} \right) \varepsilon^{-\Gamma l} - \left( 1 + \frac{\gamma X_l}{\Gamma Z_{0a}} \right) \left( 1 + \frac{X_0}{Z_{0a}} \right) \varepsilon^{\Gamma l} \right\}}{\left( 1 + \frac{X_0}{Z_{0a}} \right) \left( 1 + \frac{X_l}{Z_{0a}} \right) \varepsilon^{\Gamma l} - \left( 1 - \frac{X_0}{Z_{0a}} \right) \left( 1 - \frac{X_l}{Z_{0a}} \right) \varepsilon^{-\Gamma l}} \end{aligned} \right\} \quad (10)$$

By substituting these values of  $A_1$  and  $A_2$  into Eqs. (7), we can obtain the solutions of the voltage and the current of the anode line. Let us now calculate the ideal output and the ideal gain of this tube. We postulate the following four conditions.

1) Grid line is terminated with matched impedance and there is no reflected wave on the line.

2) Termination impedances of both ends

of anode line are equal to its characteristic impedance  $Z_{0a}$ .

3) Propagation constants of grid and anode lines are identical.

4) Both grid and anode lines have no loss.

From condition 1,

$$J_2 = 0$$

and from 2), 3), and 4), we have

$$X_0 = X_l = Z_{0a}$$

$$\Gamma = \gamma = j\beta_a = j\beta_a$$

Substituting these relations into Eqs. (7) we have

$$\left. \begin{aligned} E_a &= \frac{J_1 Z_{0a}}{2} \left\{ \left( z - j \frac{1}{2\beta_a} \right) \varepsilon^{-j\beta_a z} \right. \\ & \quad \left. + j \frac{1}{2\beta_a} \varepsilon^{-j\beta_a(2l-z)} \right\} \\ I_a &= \frac{J_1}{2} \left\{ \left( z + j \frac{1}{2\beta_a} \right) \varepsilon^{-j\beta_a z} \right. \end{aligned} \right\} \quad (11)$$

$$\left. \begin{aligned} & -j \frac{1}{2\beta_a} \varepsilon^{-j\beta_a(2l-z)} \end{aligned} \right\}.$$

If we write the voltage at  $z=0$  and  $z=l$  as  $E_{a0}$  and  $E_{al}$  respectively, we have

$$\left. \begin{aligned} E_{a0} &= -j \frac{J_1 Z_{0a} l}{2} \cdot \frac{1}{2\beta_a l} (1 - \varepsilon^{-j2\beta_a l}) \\ E_{al} &= \frac{J_1 Z_{0a} l}{2} \varepsilon^{-j\beta_a l} = E_{aln}. \end{aligned} \right\} \quad (12)$$



As Eqs. (12) show, the amplitude of voltage  $E_{al}$  is independent of frequency and will be the output voltage of this tube. On the contrary, the amplitude of voltage  $E_{a0}$  depends on frequency and it diminishes rapidly as frequency increases.

In Fig. 2, the frequency response of the amplitude and of the phase angle of  $E_{a0}$  and  $E_{al}$  are shown. The abscissa represents the wave number on the anode line (or the grid line) instead frequency.

The output voltage  $E_{aln}$  of Eqs. (12) will be used in the following discussion as a standard output and the output in various

cases will be compared with  $E_{aln}$ .

From Eqs. (12) the ideal gain  $N_0$  will be calculated as follows:

The input voltage of grid line is obtained from Eq. (2),

$$E_{g0} = E_{g1},$$

the gain  $N_0$  can then be written as follows:

$$\begin{aligned} N_0 &= \frac{E_{aln}}{E_{g0}} = \frac{(1/2)g_m E_{g1} Z_{0a} l}{E_{g1}} \epsilon^{-j\beta_a l} \\ &= \frac{1}{2} g_m l Z_{0a} \epsilon^{-j\beta_a l} = \frac{1}{2} G_m Z_{0a} \epsilon^{-j\beta_a l} \quad (13) \end{aligned}$$

where  $G_m$  is the total mutual conductance of tube and is calculated as  $G_m = g_m l$ .

In the following sections, we will discuss various problems such as impedance matching of the lines, differences of propagation velocities on the two lines, and line losses.

### 1.1.1. Effect of Anode Line Termination

It is two complicated to substitute into general Eqs. (7) the various values of termination impedance in order to observe termination effects on the anode line. Thus, we shall investigate these problems under the following conditions.

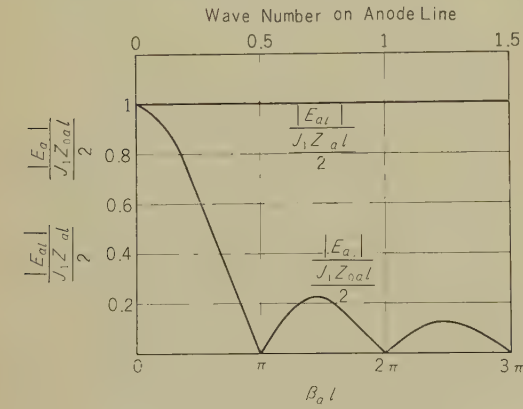
- 1) We examine the output voltage only in the followings.
- 2) Velocities of propagation on both lines, grid and anode, are equal.
- 3) Termination impedances of both ends of anode line are equal.
- 4) Termination of grid line is matched and no reflected wave exists.

From conditions (2), (3), and (4) we have

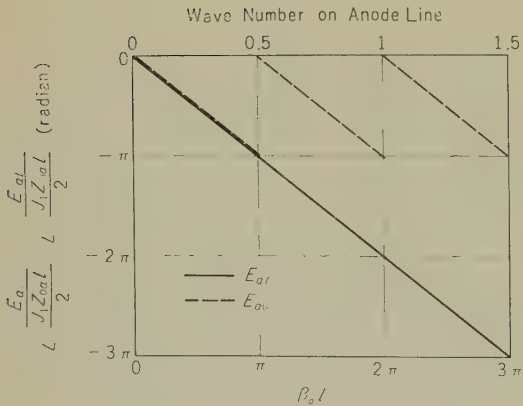
$$\gamma \rightarrow \Gamma, \quad X_0 = X_l = X, \quad J_2 = 0.$$

Substituting these conditions into Eqs. (7) and (10), we have the output voltage

$$E_{al} = \frac{\frac{J_1}{2} \cdot \frac{Z_{0a}}{\Gamma}}{\left(1 + \frac{X}{Z_{0a}}\right)^2 \epsilon^{\Gamma l} - \left(1 - \frac{X}{Z_{0a}}\right) \epsilon^{-\Gamma l}}$$



(a)-Amplitude.



(b)-Phase angle.

Fig. 2—Anode terminal voltage at ideal amplification.

$$\times \left\{ 2\Gamma l \frac{X}{Z_{0a}} \left( 1 + \frac{X}{Z_{0a}} \right) + \frac{X}{Z_{0a}} \left( 1 - \frac{X}{Z_{0a}} \right) (e^{-2\Gamma l} + 1) \right\}. \tag{15}$$

Here we calculate three examples of  $X/Z_{0a} = 1/2, 1$  and  $2$ , and show the results in Fig. 3. In Fig. 3, however, line loss was neglected and  $\Gamma$  was denoted as

$$\Gamma = j\beta_a. \tag{16}$$

Furthermore the output was represented in the form of the ratio of  $E_{al}$  of Eq. (15) to  $E_{aln}$  of Eq. (12).

The ratio  $Q_a = E_{al}/E_{aln}$  is given as follows:

$$Q_a = \frac{E_{al}}{E_{aln}} = \frac{\left\{ 2 \frac{X}{Z_{0a}} \left( 1 + \frac{X}{Z_{0a}} \right) - \frac{1}{j\beta_a l} \frac{X}{Z_{0a}} \left( 1 - \frac{X}{Z_{0a}} \right) \right\} e^{-j\beta_a l} + \frac{1}{j\beta_a l} \frac{X}{Z_{0a}} \left( 1 - \frac{X}{Z_{0a}} \right) e^{-j\beta_a l}}{\left( 1 + \frac{X}{Z_{0a}} \right)^2 e^{j\beta_a l} - \left( 1 - \frac{X}{Z_{0a}} \right)^2 e^{-j\beta_a l}} \tag{17}$$

In Fig. 3 the amplitude and the phase angle of  $Q_a$  vary periodically with increase of wave number on the anode line when the terminations are mismatched.

1.1.2. Effect of Grid Line Termination

The grid line termination is easily calculated

as a common transmission line. The current and voltage equations of the grid line are given by

$$\left. \begin{aligned} -dE_g &= Z_g I_g dz \\ -dI_g &= Y_g E_g dz \end{aligned} \right\} \tag{18}$$

where  $Z_g$  is series impedance and  $Y_g$  is parallel admittance.

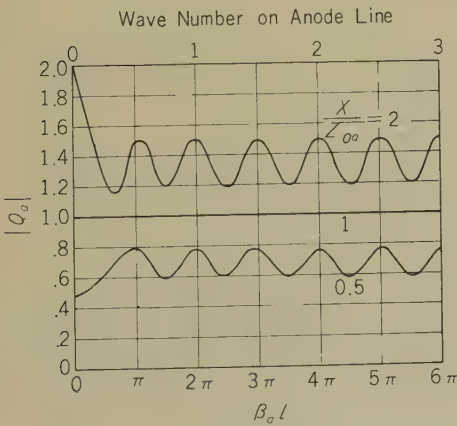
From Eq. (18), we have

$$\left. \begin{aligned} \frac{d^2 E_g}{dz^2} &= Z_g Y_g E_g \\ \frac{d^2 I_g}{dz^2} &= Z_g Y_g I_g \end{aligned} \right\} \tag{19}$$

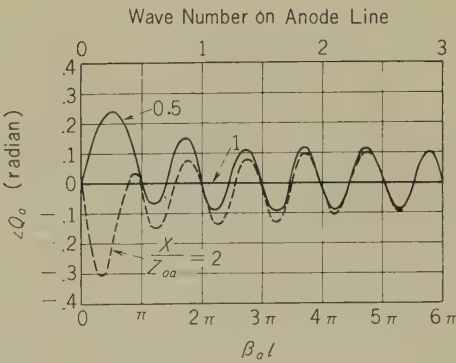
The solutions of Eq. (19) are

$$\left. \begin{aligned} E_g &= Z_{0g} (B_1 e^{-\gamma z} - B_2 e^{\gamma z}) \\ I_g &= B_1 e^{-\gamma z} + B_2 e^{\gamma z} \end{aligned} \right\} \tag{20}$$

where  $\gamma = \sqrt{Z_g Y_g}$ ,  $Z_{0g} = \sqrt{Z_g/Y_g}$ , and  $B_1, B_2$  are constants.



(a)-Amplitude.



(b)-Phase angle.

Fig. 3—Effect of matching of anode line on output voltage.

When the output termination impedance of the grid line is  $x_l$  as shown in Fig. 4,  $B_1$  and  $B_2$  are given as follows:

$$\left. \begin{aligned} B_1 &= \frac{Z_{0g} + x_l}{Z_{0g} \{ (Z_{0g} + x_l) - (Z_{0g} - x_l) \varepsilon^{-2\gamma l} \}} E_{g0} \\ B_2 &= \frac{Z_{0g} - x_l}{Z_{0g} \{ (Z_{0g} + x_l) \varepsilon^{2\gamma l} - (Z_{0g} - x_l) \}} E_{g0} \end{aligned} \right\} \quad (21)$$

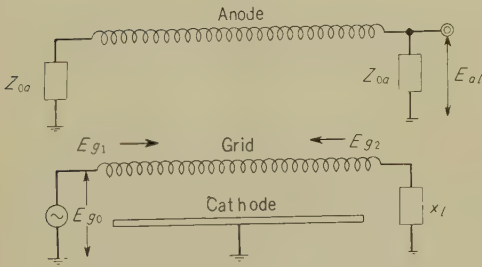


Fig. 4—Grid line termination.

Substituting  $B_1$  and  $B_2$  into Eqs. (20) comparing Eq. (20) with Eq. (1), we have

$$\left. \begin{aligned} E_{g1} &= Z_{0g} B_1 = \frac{Z_{0g} + x_l}{(Z_{0g} + x_l) - (Z_{0g} - x_l) \varepsilon^{-2\gamma l}} E_{g0} \\ E_{g2} &= -Z_{0g} B_2 \varepsilon^{\gamma l} = \frac{-(Z_{0g} - x_l) \varepsilon^{\gamma l}}{(Z_{0g} + x_l) \varepsilon^{2\gamma l} - (Z_{0g} - x_l)} E_{g0} \end{aligned} \right\} \quad (22)$$

To examine the effect of the grid line termination on the output voltage of the anode line, we substitute into Eqs. (7) the calculated values of Eqs. (20) for various values of  $x_l/Z_{0g}$ . To simplify the calculation, it is assumed here that the anode line termination is perfectly matched, the propagation velocities of both lines, anode and grid, are equal, and no losses exist on either lines.

From the above conditions, we have

$$X = Z_{0a}, \quad \Gamma = \gamma.$$

Then Eq. (7) is given as

$$E_a = \left( \frac{J_1 Z_{0a}}{2} z + \frac{J_1 Z_{0a}}{4\Gamma} - \frac{J_2 Z_{0a}}{4\Gamma} \right) \varepsilon^{-\Gamma z} - \left( \frac{J_2 Z_{0a}}{2} z \right)$$

$$+ \frac{J_1 Z_{0a}}{4\Gamma} \varepsilon^{-2\Gamma l} - \frac{J_2 Z_{0a}}{4\Gamma} - \frac{J_2 Z_{0a} l}{2} \varepsilon^{\Gamma z}. \quad (23)$$

And the output voltage  $E_{al}$  is

$$E_{al} = \frac{J_1 Z_{0a}}{2} l \varepsilon^{-j\beta_{al}} - j \frac{J_2 Z_{0a}}{4\beta_{al}} \varepsilon^{j\beta_{al}} (1 - \varepsilon^{-j2\beta_{al}}) \quad (24)$$

where  $\Gamma = j\beta_a$ .

To compare  $E_{al}$  of Eq. (24) with  $E_{aln}$  of Eq. (12),  $E_{al}$  is divided by  $E_{aln}$  and the ratio is denoted by  $\theta_g$ :

$$\theta_g = 1 - j \frac{1}{2} \frac{1}{\beta_{al}} \frac{J_2}{J_1} (1 - \varepsilon^{-j2\beta_{al}}). \quad (25)$$

From Eqs. (4) and (22),  $J_2/J_1$  is given as follows:

$$\frac{J_2}{J_1} = \frac{E_{g2}}{E_{g1}} \varepsilon^{-j\beta_{al}} = - \frac{Z_{0g} - x_l}{Z_{0g} + x_l} \varepsilon^{-j2\beta_{al}}. \quad (26)$$

Substituting Eq. (26) into Eq. (25), we have

$$\begin{aligned} \theta_g &= 1 + j \frac{1}{2\beta_{al}} \frac{Z_{0g} - x_l}{Z_{0g} + x_l} \varepsilon^{-j2\beta_{al}} (1 - \varepsilon^{-j2\beta_{al}}) \\ &= 1 + j \frac{1}{2\beta_{al}} \frac{1 - (x_l/Z_{0g})}{1 + (x_l/Z_{0g})} \varepsilon^{-j2\beta_{al}} (1 - \varepsilon^{-j2\beta_{al}}). \end{aligned} \quad (27)$$

Calculated results of Eq. (27) for the values of  $x_l/Z_{0g} = 1/2, 1, 2$  are shown in Fig. 5. Fig. 5 shows that variations of amplitude and phase of  $\theta_g$  diminishes gradually when the wave number increases.

### 1.1.3. Effect of Differences of Propagation Velocities of Anode and Grid Lines

In order to simplify the calculations, we assume that both lines are terminated with matched impedances respectively.

Substituting  $X_0 = X_l = Z_{0a}$  into Eqs. (7), we have

$$E_a = - \frac{Z_{0a}}{2} \left( J_1 \frac{1}{\Gamma - \gamma} + J_2 \frac{1}{\Gamma + \gamma} \right) \varepsilon^{-\Gamma z}$$



$$+J_1\Gamma Z_{0a}\frac{\epsilon^{-\gamma z}}{\Gamma^2-\gamma^2}-\frac{Z_{0a}}{2}\left(J_1\frac{\epsilon^{-\gamma l-\Gamma l}}{\Gamma+\gamma}\right. \\ \left.+J_2\frac{\epsilon^{\gamma l-\Gamma l}}{\Gamma-\gamma}\right)\epsilon^{\Gamma z}+J_2\Gamma Z_{0a}\frac{\epsilon^{\gamma z}}{\Gamma^2-\gamma^2}. \quad (28)$$

$$E_a=-\frac{1}{2}\frac{J_1Z_{0a}}{\Gamma-\gamma}\epsilon^{-\Gamma z}+\frac{J_1\Gamma Z_{0a}}{\Gamma^2-\gamma^2}\epsilon^{-\gamma z} \\ -\frac{1}{2}\frac{J_1Z_{0a}}{\Gamma+\gamma}\epsilon^{-\gamma l-\Gamma l+\Gamma z}. \quad (29)$$

The output voltage at  $z=l$  is

$$E_{al}=\frac{1}{2}J_1Z_{0a}\frac{1}{\Gamma-\gamma}(\epsilon^{-\gamma l}-\epsilon^{-\Gamma l}) \\ =\frac{1}{2}J_1Z_{0a}l\epsilon^{-\Gamma l}\frac{1}{(\Gamma-\gamma)l}(\epsilon^{\Gamma l-\gamma l}-1). \quad (30)$$

The ratio  $E_{al}/E_{aln}$  is denoted as  $P$  which is given as follows:

$$P=\frac{E_{al}}{E_{aln}}=\epsilon^{-\alpha_a l}\frac{\epsilon^{(\alpha_a+j\beta_a-\alpha_g-j\beta_g)l}-1}{(\alpha_a+j\beta_a-\alpha_g-j\beta_g)l} \quad (31)$$

where

$$\Gamma=\alpha_a+j\beta_a, \quad \gamma=\alpha_g+j\beta_g.$$

Examples for the following numerical values are calculated and they are shown in Fig. 6:

$$\left. \begin{aligned} \alpha_a l &= 0 & \alpha_g l &= 0, 1, 2 \\ \beta_g l &= (0.7, 0.85, 1, 1.15 \text{ and } 1.3) \times \beta_a l. \end{aligned} \right\} \quad (32)$$

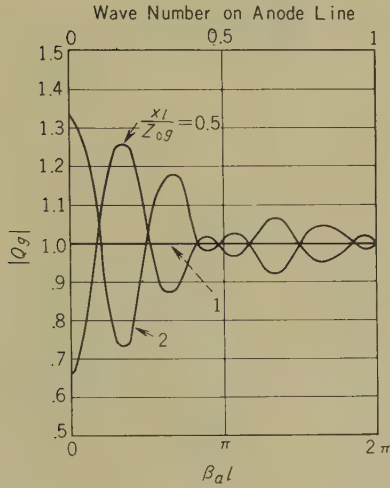
The curves for  $\alpha_g l=0$  are identical with those in a former report<sup>(3)</sup> which were calculated by a different method.

#### 1.1.4. Dispersion of Electron Beams

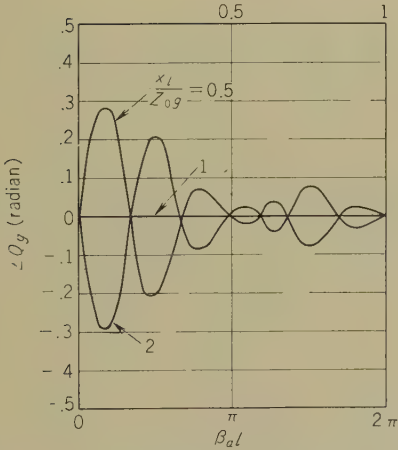
In the above discussion we assume that all electron paths are perpendicular to electrode axis  $z$ , and an electron departing from a position  $z$  on the cathode passes the grid line at  $z$ , and arrives at  $z$  on the anode line.

In a real tube, however, dispersion of electrons occurs, and electrons departing from one point  $z$  of the cathode are scattered and arrive over a band rather than a point on the anode line. This phenomenon lowers tube gain.

We shall discuss the effects of the dispersion



(a)-Amplitude.



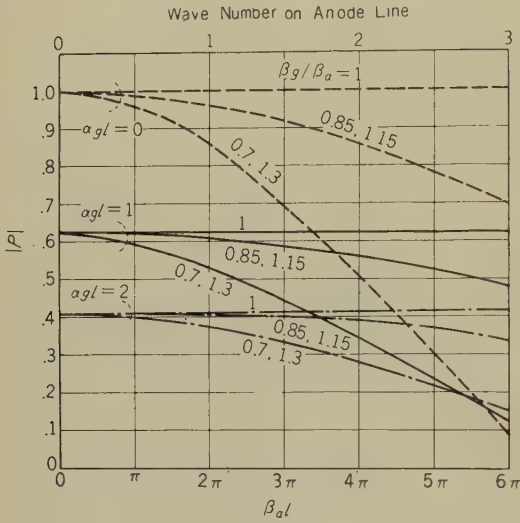
(b)-Phase angle.

**Fig. 5**—Effect of matching of grid line on output voltage.

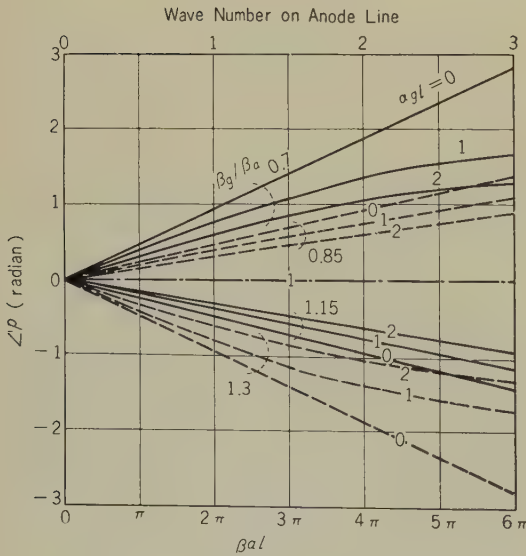
As the grid line termination is matched, no reflected wave exists on the line. Then substituting  $J_2=0$  into Eq. (28), we have

of electrons on the simplified model shown in Fig. 7.

We assume that electrons are dispersed over a small angle  $\delta$  after passing the grid



(a)-Amplitude.



(b)-Phase angle.

**Fig. 6**—Effect of grid loss and of difference of propagation velocities on anode and grid lines, on output voltage.

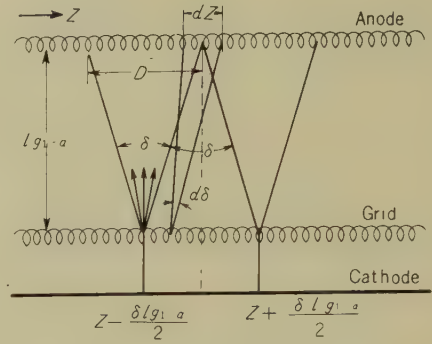


**Fig. 7**—Dispersion of electron beams.

line as represented in Fig. 7. If we remove our standpoint to a position on the anode line we shall see electrons which are injected from the range of the grid line over an angle  $\delta$ . Denoting the distance between grid and anode as  $l_{g1-a}$ , we have the range of the above mentioned grid line corresponding to a position  $z$  on the anode as follows.

$$z - \frac{\delta l_{g1-a}}{2} \sim z + \frac{\delta l_{g1-a}}{2}$$

To simplify the calculations, we assume here that the dispersion of the electrons is uniform throughout angle  $\delta$ , and that the matching of the lines and the propagation velocities of the lines are ideal. Then, on the grid line there exist only forward waves so that the electron currents modulated by the grid line are:

$$J_{g1} = g_m E_{g1} e^{-\Gamma z} \quad (33)$$

where

$$\Gamma = \gamma.$$

The injection current into the small length of the anode line  $dz$  at  $z$  is denoted as  $J'dz$ . On the other hand the electron current which goes towards  $dz$  at  $z$  on the anode line after passing a small length of the grid line  $dz$  in the range  $z \pm \frac{\delta l_{g1-a}}{2}$ , is represented as

$$J_{g1} \cdot \frac{d\delta}{\delta} \cdot dz. \quad (34)$$

Then,  $J'$  is calculated by the integration of

$J_{g1}(d\delta/\delta)dz$  over the range  $z \pm (\delta \cdot l_{g1-a}/2)$   
Then we have

$$J' = \int_{z - \frac{\delta \cdot l_{g1-a}}{2}}^{z + \frac{\delta \cdot l_{g1-a}}{2}} J_{g1} \cdot \frac{d\delta}{\delta} \quad (35)$$

Substituting  $d\delta \cdot l_{g1-a} = dz$ , we have

$$J' = \frac{g_m E_{g1}}{\delta \cdot l_{g1-a} \cdot \Gamma} \epsilon^{-\Gamma z} \left( \epsilon^{\frac{\delta \cdot l_{g1-a} \Gamma}{2}} - \epsilon^{-\frac{\delta \cdot l_{g1-a} \Gamma}{2}} \right). \quad (36)$$

The injection current when no dispersion of electrons occurs, has been given as

$$J = g_m E_{g1} \epsilon^{-\Gamma z}. \quad (37)$$

Comparing Eq. (36) with Eq. (37), we have the following effective mutual conductance  $g_m'$  when electron dispersion exists:

$$g_m' = g_m \frac{1}{\delta \cdot l_{g1-a} \cdot \Gamma} \left( \epsilon^{\frac{\delta \cdot l_{g1-a} \Gamma}{2}} - \epsilon^{-\frac{\delta \cdot l_{g1-a} \Gamma}{2}} \right). \quad (38)$$

When we consider a lossless line, we obtain the following relation by putting  $\Gamma = j\beta_a$ .

$$g_m' = g_m \cdot \frac{2}{D\beta_a} \sin \frac{D\beta_a}{2} \quad (39)$$

where  $D = \delta \cdot l_{g1-a}$ , which gives the dispersion length on the anode line as shown in Fig. 7.

In Fig. 8  $g_m'$  is represented. The abscissa of the figure gives the ratio of  $D$  to the wave length on the anode line  $\lambda_a$  which is calculated by the relation

$$\beta_a = \frac{2\pi}{\lambda_a}.$$

As shown in Fig. 8, lowering of the effective mutual conductance occurs when the dispersion of electron beams increases.

### 1.2. Calculation of Characteristic of the Helical Electrodes

In our distributed amplifier tubes helical grid line and anode line electrodes were used.

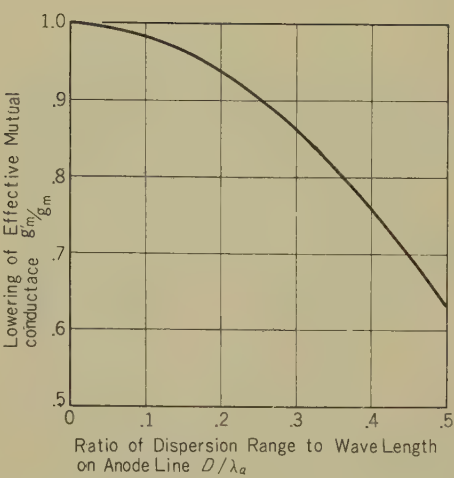


Fig. 8—Lowering of effective mutual conductance by dispersion of electron beams.

In order to design the tubes it is necessary to be able to calculate the characteristic impedances and the phase velocities of these lines. However, the construction of these helices are so complicated that it seems difficult to calculate these characteristics accurately. Thus, we have developed an approximate calculation method for practical design purposes and proved the method to be effective for grid and anode line design.

In Fig. 9 (a) the cross section of the grid helix is shown. As the construction of the anode helix takes nearly the same form, we shall discuss only the grid helix as follows.

As it is too difficult to calculate a flat helix like our grid, first we transform its cross section to the form shown in Fig. 9 (b).

In this transformation the contour length and the distances between the helix and the internal conductor are unchanged. The gap between the helix and the inner conductor is so small that the characteristics of helix will not greatly be changed by the above transformation. The calculation on the helix shown in Fig. 9 (b) is still not easy. Thus, we transform it to an equivalent transmission line form as shown in Fig. 9 (c).

In this case the currents on the helix pass the short lines through the vacuum and the short lines along the ceramics in turn. First



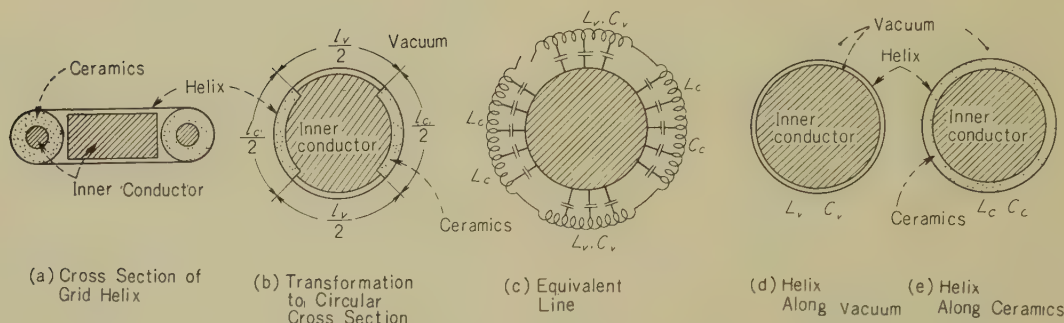


Fig. 9—Calculation of helix characteristics.

we compute the characteristics of a line which is in vacuum as shown in Fig. 9 (d). In Fig. 9 (d) the contour length and the gap between helix and inner conductor are maintained as before.

On the line shown in Fig. 9 (d), we determine the equivalent series inductance and parallel capacitance of the line in a vacuum. Next we calculate the characteristics of a line along the ceramics as shown in Fig. 9 (e). Then we determine the equivalent inductance and capacitance of this line.

We denote these inductances and capacitances of the two lines as follows.

$$\begin{aligned} L_v, C_v &: \text{Line in a vacuum} \\ L_c, C_c &: \text{Line along the ceramics} \end{aligned}$$

We compute the inductance and capacitance of the composite line shown in Fig. 9 (c) with the following procedures.

Composite inductance and capacitance are calculated by proportional addition of inductance or capacitance of the two lines according to the ratio of their lengths measured on the contour respectively.

Therefore,

$$\left. \begin{aligned} L_t &= \frac{l_v}{l_c + l_v} L_v + \frac{l_c}{l_c + l_v} L_c \\ C_t &= \frac{l_v}{l_c + l_v} C_v + \frac{l_c}{l_c + l_v} C_c \end{aligned} \right\} \quad (40)$$

Where  $L_t$  and  $C_t$  are inductance or capacitance of the composite line and  $l_v$  and  $l_c$  are the length of the line through the vacuum and along the ceramics respectively.

### 1.2.1. Electromagnetic Fields of a Cylindrical Helix

The analysis of a cylindrical helix has been developed by J. R. Pierce and others.<sup>(4)(5)</sup>

They gave the solutions of the electromagnetic waves of these helices assuming a helix of pitch angle  $\phi$  as a thin cylinder on which the current flows for only the direction of angle  $\phi$  measured from the circumference of cylinder.

In our analysis we use also Pierce's ideal cylinder mentioned above but there are some complications in our problems such as the existence of both inner and outer conductors around the helix.

This comes from the fact that the grid helix has the cathode sleeve in it and screen grid mesh around it. We calculate then the electromagnetic waves for the general case shown in Fig. 10.

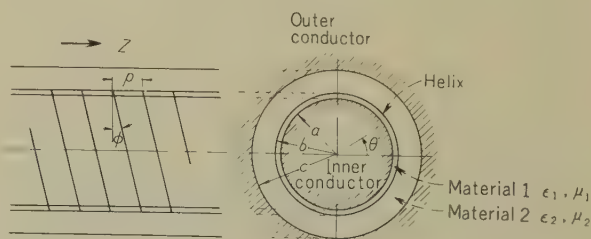


Fig. 10—Helix.

Here  $\epsilon_1$  : Dielectric constant of material 1 between helix and inner conductor.

- $\epsilon_1^*$ : Specific dielectric constant of material 1.  
 $\epsilon_2$ : Dielectric constant of material 2 between helix and outer conductor.  
 $\epsilon^*$ : Specific dielectric constant of material 2.  
 $\epsilon_0$ : Dielectric constant of vacuum.  
 $\mu_1$ : Permeability of material 1.  
 $\mu_2$ : " " " 2.  
 $p$ : Pitch of helix.  
 $\phi$ : Pitch angle of helix measured from contour of cylinder.

The general form of the waves in these cylinders is given by

$$\pi = \{A^0 I_0(\zeta r) + B^0 K_0(\zeta r)\} \epsilon^{j(\omega t - \beta z)} \quad (41)$$

where

- $I_0, K_0$ : 1st and 2nd kind modified Bessel functions  
 $A^0, B^0$ : Constants

$$\zeta^2 = \beta^2 + \omega^2 \epsilon \mu \quad (42)$$

- $\beta$ : Phase constant.  
 $\omega$ : Dielectric constant of medium.  
 $\mu$ : Permeability of medium.

Then the electric and the magnetic fields in mediums 1 and 2 are given as follows:

$$F_r^{(i)}, F_\theta^{(i)}, F_z^{(i)}, H_r^{(i)}, H_\theta^{(i)}, H_z^{(i)} \quad i=1, 2$$

where suffixes  $r, \theta$  and  $z$  represent radial, angular, and longitudinal coordinates respectively. If

$$\text{and } \left. \begin{aligned} \xi^2 &= \beta^2 - \omega^2 \epsilon_1 \mu_1 \\ \eta^2 &= \beta^2 - \omega^2 \epsilon_2 \mu_2 \end{aligned} \right\}, \quad (43)$$

Then:

$$F_r^{(1)} = j \frac{\beta}{\xi} \{A^1 I_1(\xi r) - B^1 K_1(\xi r)\} \epsilon^{j(\omega t - \beta z)}$$

$$F_\theta^{(1)} = j \frac{\omega \mu_1}{\xi} \{C^1 I_1(\xi r) - D^1 K_1(\xi r)\} \epsilon^{j(\omega t - \beta z)}$$

$$F_z^{(1)} = \{A^1 I_0(\xi r) + B^1 K_0(\xi r)\} \epsilon^{j(\omega t - \beta z)}$$

$$H_r^{(1)} = j \frac{\beta}{\xi} \{C^1 I_1(\xi r) - D^1 K_1(\xi r)\} \epsilon^{j(\omega t - \beta z)}$$

$$H_\theta^{(1)} = j \frac{\omega \epsilon_1}{\xi} \{A^1 I_1(\xi r) - B^1 K_1(\xi r)\} \epsilon^{j(\omega t - \beta z)}$$

$$H_z^{(1)} = \{C^1 I_0(\xi r) + D^1 K_0(\xi r)\} \epsilon^{j(\omega t - \beta z)}$$

$$F_r^{(2)} = j \frac{\beta}{\eta} \{A^2 I_1(\eta r) - B^2 K_1(\eta r)\} \epsilon^{j(\omega t - \beta z)}$$

$$F_\theta^{(2)} = -j \frac{\omega \mu_2}{\eta} \{C^2 I_1(\eta r) - D^2 K_1(\eta r)\} \epsilon^{j(\omega t - \beta z)}$$

$$F_z^{(2)} = \{A^2 I_0(\eta r) + B^2 K_0(\eta r)\} \epsilon^{j(\omega t - \beta z)}$$

$$H_r^{(2)} = j \frac{\beta}{\eta} \{C^2 I_1(\eta r) - D^2 K_1(\eta r)\} \epsilon^{j(\omega t - \beta z)}$$

$$H_\theta^{(2)} = j \frac{\omega \epsilon_2}{\eta} \{A^2 I_1(\eta r) - B^2 K_1(\eta r)\} \epsilon^{j(\omega t - \beta z)}$$

$$H_z^{(2)} = \{C^2 I_0(\eta r) + D^2 K_0(\eta r)\} \epsilon^{j(\omega t - \beta z)} \quad (44)$$

Where  $I_1$  and  $K_1$  are modified Bessel Functions and  $A^1, B^1, C^1, D^1, A^2, B^2, C^2$  and  $D^2$  are constants.

Here we assume the helix is a infinitesimally thin cylinder which has lossless conductivity in the direction of winding of wire and no conductivity in the perpendicular direction. According to the above nature of the helix, we have the following boundary conditions which are applicable to our problem.

- 1) On the surface of inner conductor, the tangential component of the electric field vanishes

at  $r=a$ ,

$$F_\theta^{(1)} = F_z^{(1)} = 0.$$

- 2) On the surface of the helix, the tangential component of the electric field is perpendicular to the winding
- at  $r=b$ ,

$$F_\theta^{(1)} \cos \phi + F_z^{(1)} \sin \phi = 0,$$

- 3) On the surface of helix, the tangential

component of the electric field is continuous  
at  $r=b$ ,

$$F_{\theta}^{(1)} = F_{\theta}^{(2)}, \quad F_z^{(1)} = F_z^{(2)}.$$

- 4) On the surface of helix, the tangential component of magnetic field in the direction of winding is continuous  
at  $r=b$ ,

$$H_{\theta}^{(1)} \cos \phi + H_z^{(1)} \sin \phi \\ = H_{\theta}^{(2)} \cos \phi + H_z^{(2)} \sin \phi.$$

- 5) On the surface of outer conductor, the tangential component of the electric field vanishes  
at  $r=c$ ,

$$F_{\theta}^{(2)} = F_z^{(2)} = 0.$$

From Conditions 1), 2), 3), and 5), we have following relations between the constants.

$$\left. \begin{aligned} B^1 &= -\frac{I_0(\xi a)}{K_0(\xi a)} A^1. \\ C^1 &= -\frac{\xi}{j\omega\mu_1} \tan \phi \frac{I_0(\xi b)K_0(\xi a) - I_0(\xi a)K_0(\xi b)}{I_1(\xi b)K_1(\xi a) - I_1(\xi a)K_1(\xi b)} \cdot \frac{K_1(\xi a)}{K_0(\xi a)} A^1 \\ D^1 &= -\frac{\xi}{j\omega\mu_1} \tan \phi \frac{I_0(\xi b)K_0(\xi a) - I_0(\xi a)K_0(\xi b)}{I_1(\xi b)K_1(\xi a) - I_1(\xi a)K_1(\xi b)} \cdot \frac{I_1(\xi a)}{K_0(\xi a)} A^1 \\ A^2 &= \frac{I_0(\xi b)K_0(\xi a) - I_0(\xi a)K_0(\xi b)}{I_0(\eta b)K_0(\eta c) - I_0(\eta c)K_0(\eta b)} \cdot \frac{K_0(\eta c)}{K_0(\xi a)} A^1 \\ B^2 &= -\frac{I_0(\xi b)K_0(\xi a) - I_0(\xi a)K_0(\xi b)}{I_0(\eta b)K_0(\eta c) - I_0(\eta c)K_0(\eta b)} \cdot \frac{I_0(\eta c)}{K_0(\xi a)} A^1 \\ C^2 &= -\frac{\eta}{j\omega\mu^2} \tan \phi \frac{I_0(\xi b)K_0(\xi a) - I_0(\xi a)K_0(\xi b)}{I_1(\eta b)K_1(\eta c) - I_1(\eta c)K_1(\eta b)} \cdot \frac{K_1(\eta c)}{K_0(\xi a)} A^1 \\ D^2 &= -\frac{\eta}{j\omega\mu^2} \tan \phi \frac{I_0(\xi b)K_0(\xi a) - I_0(\xi a)K_0(\xi b)}{I_1(\eta b)K_1(\eta c) - I_1(\eta c)K_1(\eta b)} \cdot \frac{I_1(\eta c)}{K_0(\xi a)} A^1. \end{aligned} \right\} \quad (45)$$

From condition 4), we have

$$\tan^2 \phi \left[ \frac{\epsilon_1}{\xi} \{I_1(\xi b)K_0(\xi a) + I_0(\xi a)K_1(\xi b)\} \right.$$

$$\begin{aligned} & - \frac{\epsilon^2}{\eta} \{I_0(\xi b)K_0(\xi a) - I_0(\xi a)K_0(\xi b)\} \\ & \times \frac{I_1(\eta b)K_0(\eta c) + I_0(\eta c)K_1(\eta b)}{I_0(\eta b)K_0(\eta c) - I_0(\eta c)K_0(\eta b)} \Big] \\ & = \{I_0(\xi b)K_0(\xi a) - I_0(\xi a)K_0(\xi b)\} \\ & \times \left\{ \frac{\eta}{\mu_2} \frac{I_0(\eta b)K_1(\eta c) + I_1(\eta c)K_1(\eta b)}{I_1(\eta b)K_1(\eta c) - I_1(\eta c)K_1(\eta b)} \right. \\ & \left. - \frac{\xi}{\mu_1} \frac{I_0(\xi b)K_1(\xi a) + I_1(\xi a)K_0(\xi b)}{I_1(\xi b)K_1(\xi a) - I_1(\xi a)K_1(\xi b)} \right\}. \end{aligned} \quad (46)$$

Substituting the relations of (43) into (46), we can compute  $\beta$  and we can obtain complete solutions of the electromagnetic waves of the helix. To make the calculation easier, we introduce here some assumptions which are valid in a practical tube.

First we can assume that

$$\xi \approx \eta \approx \beta \quad (47)$$

because the pitch of the grid and the anode helices of our tubes is very small.

Secondly we consider a helix having no surrounding shield. The screen grid of the tube is set much farther than the cathode



from the grid helix and the neglect of screen grid will have little effect on the field around the helix.

Then we set  $c \rightarrow \infty$

( $c$  = radius of outer cylinder).

Thirdly the medium 2 in Fig. 10. is considered to be a vacuum and the permeability of medium 1 is also identical with that of a vacuum. We then have,

$$\left. \begin{aligned} \epsilon_1 &= \epsilon_1^* \epsilon_0 \\ \epsilon_2 &= \epsilon_0 \\ \mu_1 &= \mu_2 = \mu_0. \end{aligned} \right\} \quad (48)$$

Substituting the above formulae into Eq. (46) we obtain a simplified equation for  $\beta$

$$\begin{aligned} & \frac{\omega^2 \epsilon_0 \mu_0}{\beta^2 \tan^2 \phi} \\ &= \frac{I_0(\beta b) K_1(\beta a) + I_1(\beta a) K_0(\beta b)}{I_1(\beta a) K_1(\beta b) - I_1(\beta b) K_1(\beta a)} - \frac{K_0(\beta b)}{K_1(\beta b)} \\ & \quad \epsilon_1^* \frac{I_1(\beta b) K_0(\beta a) + I_0(\beta a) K_1(\beta b)}{I_0(\beta a) K_0(\beta b) - I_0(\beta b) K_0(\beta a)} - \frac{K_1(\beta b)}{K_0(\beta b)}. \end{aligned} \quad (49)$$

From Eq. (49), we obtain the value of  $\beta$ . With this  $\beta$  we calculated the constants newly from Eqs. (45).

The electromagnetic fields of the cylindrical helix can be calculated completely from Eqs. (44) and (49)'. In the following section we will consider the equivalent current and voltage on this helix and from them we will calculate the inductance and the capacitance of the equivalent transmission lines of the helix.

### 1.2.2. Equivalent Current and Voltage on Helix; Inductance and Capacitance of Equivalent Line

The equivalent voltage of helix line  $E$  is defined as the integral of the radial component of the electric field from the surface of the inner conductor to the helix surface. we calculate it from Eq. (44),

$$\begin{aligned} E &= \int_b^a F_r^{(1)} dr = \int_b^a j \left\{ I_1(\beta r) \right. \\ & \quad \left. + \frac{I_0(\beta a)}{K_0(\beta a)} K_1(\beta r) \right\} A^1 dr \cdot e^{j(\omega t - \beta z)} \\ &= \frac{j}{\beta} \left\{ I_0(\beta r) - \frac{I_0(\beta a)}{K_0(\beta a)} K_0(\beta r) \right\}_b^a A^1 \cdot e^{j(\omega t - \beta z)} \\ &= \frac{j}{\beta} \{ I_0(\beta b) K_0(\beta a) - I_0(\beta a) K_0(\beta b) \} \\ & \quad \times \frac{A^1}{K_0(\beta a)} \cdot e^{j(\omega t - \beta z)}. \end{aligned} \quad (50)$$

$$\left. \begin{aligned} B^1 &= -\frac{I_0(\beta a)}{K_0(\beta a)} A^1 \\ C^1 &= -\frac{\beta}{j\omega\mu_0} \tan \phi \frac{I_0(\beta b) K_0(\beta a) - I_0(\beta a) K_0(\beta b)}{I_1(\beta b) K_1(\beta a) - I_1(\beta a) K_1(\beta b)} \cdot \frac{K_1(\beta a)}{K_0(\beta a)} A^1 \\ D^1 &= -\frac{\beta}{j\omega\mu_0} \tan \phi \frac{I_0(\beta b) K_0(\beta a) - I_0(\beta a) K_0(\beta b)}{I_1(\beta b) K_1(\beta a) - I_1(\beta a) K_1(\beta b)} \cdot \frac{I_1(\beta a)}{K_0(\beta a)} A^1 \\ A^2 &= 0 \\ B^2 &= \frac{I_0(\beta b) K_0(\beta a) - I_0(\beta a) K_0(\beta b)}{K_0(\beta a) K_0(\beta b)} A^1 \\ C^2 &= 0 \\ D^2 &= \frac{\beta}{j\omega\mu_0} \tan \phi \frac{I_0(\beta b) K_0(\beta a) - I_0(\beta a) K_0(\beta b)}{K_0(\beta a) K_1(\beta b)} A^1 \end{aligned} \right\} \quad (49)'$$

The current is calculated as follows.

$$\begin{aligned}
 I &= p(H_z^{(1)} - H_z^{(2)})_{r=b} \\
 &= p \left[ \frac{-\beta}{j\omega\mu_0} \tan \phi \left\{ \frac{I_0(\beta b)K_0(\beta a) - I_0(\beta a)K_0(\beta b)}{I_1(\beta b)K_1(\beta a) - I_1(\beta a)K_1(\beta b)} \right\} \left\{ \frac{K_1(\beta a)}{K_0(\beta a)} I_0(\beta b) + \frac{I_1(\beta a)}{K_0(\beta a)} K_0(\beta b) \right\} \right. \\
 &\quad \left. - \frac{\beta}{j\omega\mu_0} \tan \phi \frac{I_0(\beta b)K_0(\beta a) - I_0(\beta a)K_0(\beta b)}{K_0(\beta a)K_1(\beta b)} K_0(\beta b) \right] A^1 e^{j(\omega t - \beta z)} \\
 &= -p \frac{\beta}{j\omega\mu_0} \tan \phi \{ I_0(\beta b)K_0(\beta a) - I_0(\beta a)K_0(\beta b) \} \\
 &\quad \times \left[ \frac{I_0(\beta b)K_1(\beta a) + I_1(\beta a)K_0(\beta b)}{I_1(\beta b)K_1(\beta a) - I_1(\beta a)K_1(\beta b)} \frac{1}{K_0(\beta a)} + \frac{K_0(\beta b)}{K_0(\beta a)K_1(\beta b)} \right] A^1 e^{j(\omega t - \beta z)}
 \end{aligned} \quad (51)$$

Using the voltage and current calculated above, we define the characteristic impedance of the helix

$$Z_0 = \frac{E}{I} \quad (52)$$

The  $Z_0$  is represented as follows.

$$\begin{aligned}
 Z_0 &= \frac{\omega\mu_0}{p\beta^2 \tan \phi} \\
 &\quad \times \frac{I_0(\beta b)K_1(\beta a) - I_1(\beta a)K_1(\beta b)}{I_0(\beta b)K_1(\beta b) + I_1(\beta b)K_0(\beta b)} \cdot \frac{K_1(\beta b)}{K_1(\beta a)} \\
 &= \frac{\omega\mu_0 b}{p\beta \tan \phi} \frac{K_1(\beta b)}{K_1(\beta a)} \cdot \{ I_1(\beta b)K_1(\beta a) \\
 &\quad - I_1(\beta a)K_1(\beta b) \}.
 \end{aligned} \quad (53)$$

As shown in Fig. 11, we consider a transmission line equivalent to the helix where series inductance and parallel capacitance are represented as  $L$  and  $C$  respectively. The current-voltage equations of this line are written as follows

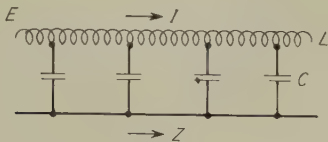


Fig. 11—Equivalent line.

$$\begin{aligned}
 -\frac{dE}{dz} &= j\omega LI \\
 -\frac{dI}{dz} &= j\omega CE
 \end{aligned} \quad (54)$$

where  $E$  is voltage and  $I$  is current. Then we have

$$\begin{aligned}
 L &= -\frac{1}{j\omega} \cdot \frac{1}{I} \frac{dE}{dz} \\
 C &= -\frac{1}{j\omega} \cdot \frac{1}{E} \frac{dI}{dz}
 \end{aligned} \quad (55)$$

On the other hand, we have from Eqs. (50) and (51),

$$\begin{aligned}
 -\frac{dE}{dz} &= j\beta E \\
 -\frac{dI}{dz} &= j\beta I
 \end{aligned} \quad (56)$$

From Eqs. (55) and (56), line inductance  $L$  and capacitance  $C$  are given immediately.

$$\begin{aligned}
 L &= \frac{\beta}{\omega} \frac{E}{I} = \frac{\beta}{\omega} Z_0 \\
 C &= \frac{\beta}{\omega} \frac{I}{E} = \frac{\beta}{\omega} \frac{1}{Z_0}
 \end{aligned} \quad (57)$$

If we calculate inductances and capacitances of the two lines of Fig. 9(d) separately by Eq. (57), we can compute the inductance and

the capacitance of the composite line of Fig. 9(c) by the proportional addition of the two lines according to Eq. (40) of the preceding section.

### 1.2.3. Electron Modulation of Helix Type Grid

If we examine the Eq. (44) precisely, we shall find that the electro-magnetic field of the helix concentrates in the neighborhood of the helix at high frequencies.

This can be deduced directly from Eqs. (44) and we show an example of calculated results in Fig. 12.

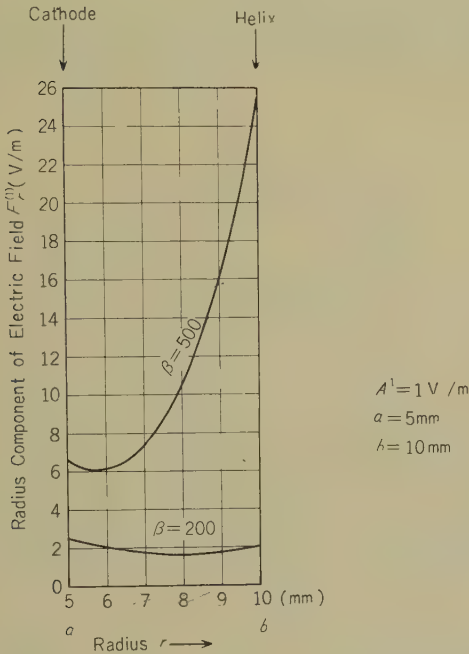


Fig. 12—Concentration of electric field in the neighborhood of helix.

This means the electric field at the cathode surface becomes small and modulation of electrons becomes weak when frequency increases. We compute this decreased modulation of electrons as follows:

We have a formula which gives the relation between the cathode current density  $J_c$  and electric field on the cathode surface  $F_c$ .

$$J_c = K F_c^{3/2} \quad (58)$$

where  $K$  is a constant.

If we consider the superposed field of the  $d-c$  component  $F_0$  and the small  $a-c$  component  $\Delta F$ , we have an  $a-c$  component of cathode current

$$\Delta J = \frac{3}{2} K F_0^{1/2} \Delta F. \quad (59)$$

If an  $a-c$  signal whose amplitude is constant but whose frequency is varied from low to high is applied to the grid helix the modulated current density will become small at high frequencies as can be easily deduced from Eqs. (44) and (59).

In the following we examine the radial component of the electric field at the cathode surface as a function of frequency.

The  $a-c$  electric field at the cathode surface is given by

$$\begin{aligned} \Delta F &= (F_r^{(1)})_{r=a} = j \{ A^1 I_1(\beta a) - B^1 K_1(\beta a) \} \epsilon^{j(\omega t - \beta z)} \\ &= j \left\{ I_1(\beta a) + \frac{I_0(\beta a)}{K_0(\beta a)} K_1(\beta a) \right\} A^1 \epsilon^{j(\omega t - \beta z)} \end{aligned} \quad (60)$$

On the other hand, voltage applied to the grid helix was given by Eq. (50)

$$\begin{aligned} E &= \frac{j}{\beta} \{ I_0(\beta b) K_0(\beta a) - I_0(\beta a) K_0(\beta b) \} \\ &\times \frac{A^1}{K_0(\beta a)} \epsilon^{j(\omega t - \beta z)} \end{aligned} \quad (61)$$

To examine the  $a-c$  field with unit voltage on the grid, we divide  $\Delta F$  by  $E$ . Then we have

$$\begin{aligned} \frac{\Delta F}{E} &= \frac{I_1(\beta a) K_0(\beta a) + I_0(\beta a) K_1(\beta a)}{I_0(\beta b) K_0(\beta a) - I_0(\beta a) K_0(\beta b)} \cdot \beta \\ &= \frac{1}{a} \cdot \frac{1}{I_0(\beta b) K_0(\beta a) - I_0(\beta a) K_0(\beta b)}. \end{aligned} \quad (62)$$

Before we examine the frequency dependency of Eq. (62), we calculate the value at zero



frequency.

Substituting  $\beta=0$  into Eq. (62), we have

$$\left\{ \frac{\Delta F}{E} \right\}_{\beta \rightarrow 0} = \frac{1}{a} \frac{1}{\log b/a}. \tag{63}$$

This corresponds to  $d$ - $c$  field at the cathode surface of a cylindrical electrode diode. The ratios of  $a$ - $c$  field of Eq. (62) to the  $d$ - $c$  field of Eq. (63) are plotted in Fig. 13 for the following examples:  $a:b=0.8:1$  and  $0.5:1$  where  $a$  and  $b$  are radii of cathode cylinder and grid helix respectively.

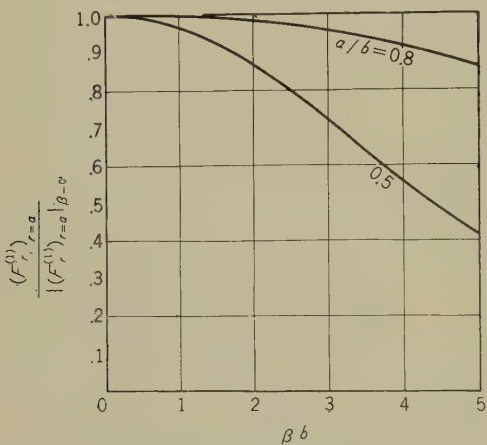


Fig. 13—Lowering of electric field at cathode surface in high frequency region.

In the case of  $a:b=0.5:1$ , considerable lowering of the  $a$ - $c$  field occurs in the high frequency region but in the case of  $a:b=0.8:1$ , lowering effect is negligibly small, as in our practical tube the ratio of  $a/b$  is greater than 0.8, we can neglect then the frequency dependency of the cathode surface field mentioned above.

2. Examples of Experimental Tubes

In preceding section the amplification theory of the distributed amplifier tube and the calculation procedure of the characteristics of the helical electrodes which are used in the distributed amplifier tube are discussed. In this section a few examples of experi-

mental tubes made in our laboratory are presented. One tube amplifies over the frequency band of zero to 150 Mc/s.

In Fig. 14 a photograph of a sample tube is shown.

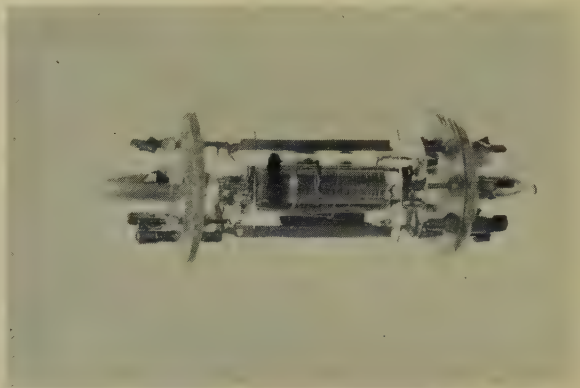


Fig. 14—Tube of Section 2.2.

2.1. Experimental 30 Mc Bandwidth Tube

2.1.1. Construction

As its cross section in Fig. 15 shows, the tube is a coaxial type tetrode with the cathode in the center, about which the control grid helix, the screen grid mesh and the anode helix are placed. (The general construction is same as that shown in reference (3)) Principal dimensions of the tube and electrodes are as follows:

Total length of envelope :	95 mm
Diameter of envelope :	44 mm
Cathode : Oxide coated	
Length	50 mm
Emission Area	4.8 cm <sup>2</sup>
Grid Helix : Length	40 mm
Wire diameter	0.03 mm
Pitch	0.15 mm
Total wire length	10 m.
Anode Helix : Length	40 mm
Wire Diameter	0.2 mm
Pitch	0.289 mm
Total wire length	10 m.

2.1.2. Static Characteristics

In Fig. 16 Static Characteristic curves are shown.

2.1.3. Amplification

In Fig. 17 the amplifier circuit is shown. For the purpose of cancelling the effects of the stray capacitances of the tube output leads, a low-pass filter circuit is connected at each line terminal. In this way a matching of lines is accomplished.

However the cutoff frequency of these low-pass filters limits the bandwidth of the

amplifiers.

The measured amplification gain versus frequency is plotted in Fig. 18. The gain is generally flat in the amplification band and drops abruptly above 30 Mc/s.

The values of the coils of the grid and the anode line termination networks are determined from the following equation.

$$\sqrt{\frac{L}{2C_s}}=K \tag{64}$$

where  $C_s$  is stray capacitance and  $K$  is the image impedance of the low pass filter.

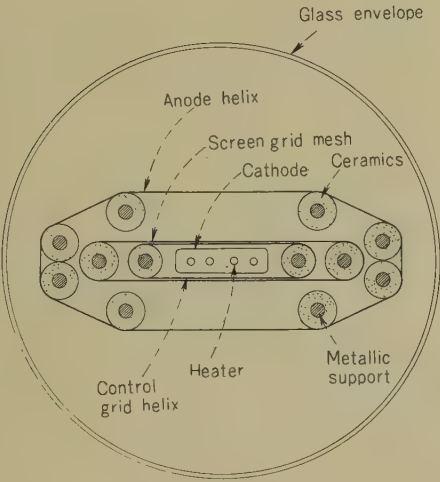


Fig. 15—Cross section of experimental tube.

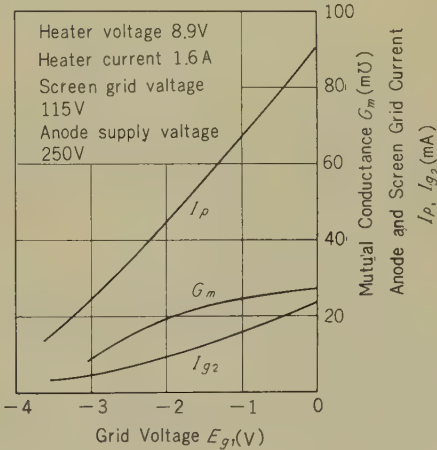


Fig. 16—Static characteristics of experimental tube of Section 2.1.

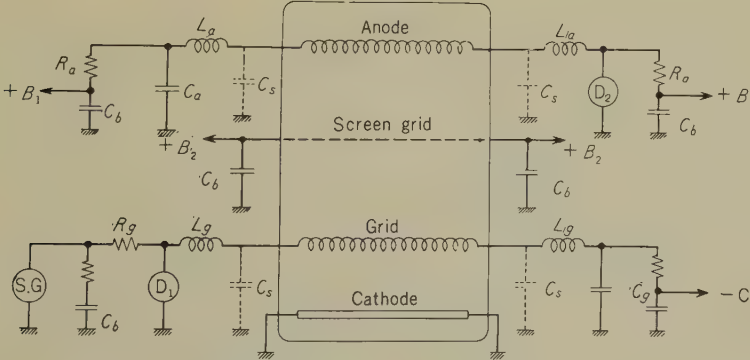
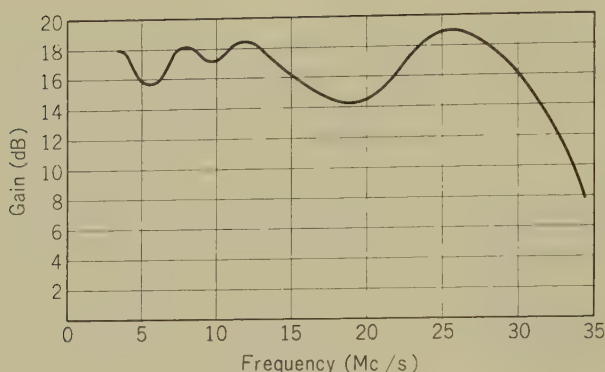


Fig. 17—Circuit for measuring gain of tube.



**Fig. 18**—Gain of the tube of Section 2.1.

On the other hand the cutoff frequency  $f_c$  of the low pass filter is given as follows.

$$f_c = \frac{1}{\pi \sqrt{2LC_s}} = \frac{1}{2\pi C_s K} \quad (65)$$

As the grid and anode line impedances are both about  $1000 \Omega$ , we substitute  $K=1000\Omega$  and  $C_s=2.5 \text{ pF}$  into Eqs. (64) and (65). Then we have

$$L=5\mu H \quad (=L_a=L_g)$$

where  $L_a$  is the inductance of the anode coil,  $L_g$  is the inductance of the grid coil, and  $f_c=63.7 \text{ Mc/s}$ .

## 2.2. Experimental 150 Mc Bandwidth Tube

### 2.2.1. Design Improvement

The cutoff frequencies of the anode and the grid lines were increased. The stray capacitances of the output leads were decreased from  $2.5 \text{ pF}$  to approximately  $1.4 \text{ pF}$ . Then the impedance of the anode line was decreased to  $450 \text{ ohms}$  and the impedance of the grid line was decreased to  $200 \text{ ohms}$ . With these improvements, the cutoff frequencies of the anode line was calculated to be  $250 \text{ Mc}$  and that of the grid line to be  $495 \text{ Mc}$ .

### 2.2.2. Construction

To lower the impedance of a helical line, the pitch of the winding must be enlarged.

In the case of the grid line, however, the enlargement of winding pitch results in a fall of mutual conductance.

To satisfy these two contradictory requirements, a triply wound helix is employed. Principal dimensions of the electrodes are as follows.

Envelope and Cathode : Identical to preceding tube.

Grid Helix : Length 37 mm  
Wire diameter 0.03 mm  
Pitch of winding 0.45 mm  
(triple helix)

Distance of adjacent wires

$$\frac{0.45}{3} = 0.15 \text{ mm}$$

Total Wire Length : 3 m.

Anode Helix : Length 35 mm

Ribon cross section

$$0.15 \times 0.05 \text{ mm}$$

Pitch 0.84 mm

Total Ribon Length 3 m.

### 2.2.3. Static Characteristics

In Fig. 19, Static Characteristics are shown.

### 2.2.4. Amplification

#### 2.2.4.1. Gain

The circuit is the same as that in Fig. 17 except for the following parameter values.

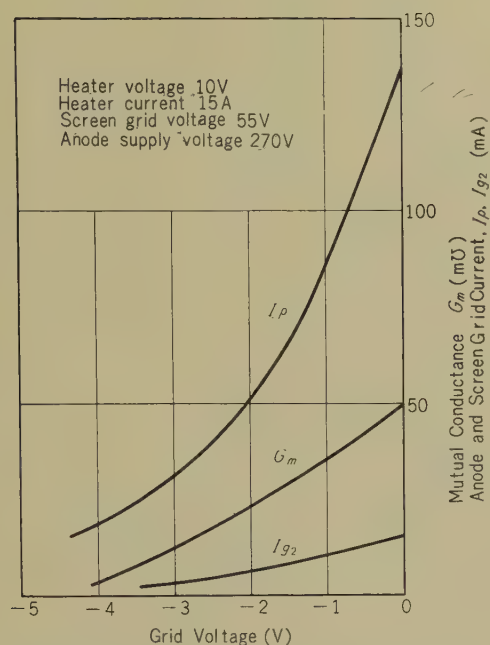


Fig. 19—Static characteristics of tube of Section 2.2.

Anode line matching resistance  $R_a$  450  $\Omega$   
Grid line matching resistance  $R_g$  200  $\Omega$   
Anode Termination Filter Inductance

$$L_a = 0.56 \mu\text{H}$$

Grid Termination Filter Inductance

$$L_g = 0.13 \mu\text{H}$$

Anode Stem Stray Capacitance 1.4 pF

Grid Stem Stray Capacitance 1.6 pF

Anode Filter cutoff Frequency 250 Mc

Grid Filter cutoff Frequency 495 Mc

In Fig. 20 (a) gain versus frequency curve is plotted. Fig. 20 (a) shows that the amplification band of this tube is extended to 150 Mc/s.

The gain characteristics will be discussed in detail in section 3.

### 2.2.4.2. Phase

The phase difference between the grid input voltage and the anode output voltage was measured for the frequency range from 500 kc/s to 50 Mc/s, with phase measuring equipment. The results are shown in Fig. 20 (b). It is supposed that the irregular variation observed in the low frequency region was caused by using a bypass capacitor too small for such low frequencies.

## 3. Analysis of Experimental Results

The analysis of the experimental results, especially the tube with a 150 Mc bandwidth, is presented here. The line losses, propagation characteristics of the helical lines, and the amplification characteristics are discussed.

### 3.1. Line Losses

The anode line has negligibly small loss because it is a helix wound with thick molybdenum wire. On the contrary, the grid helix has considerable losses. This results not only from the thin winding wire but also because of the increase of the conductance component caused by the electron transit angle in the

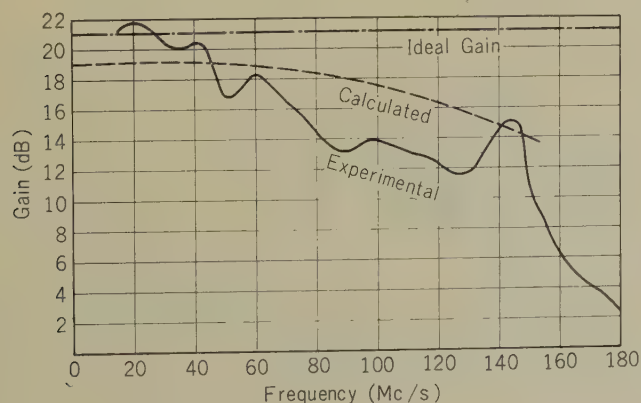


Fig. 20 (a)—Gain of the tube Section 2.2.



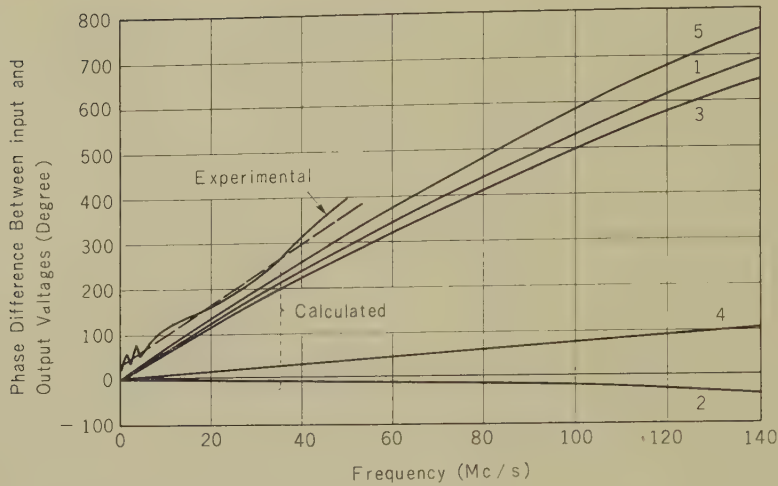


Fig. 20 (b)—Phase difference between input and output voltages of the tube of Section 2.2.

high frequency region.

First, we measured experimentally the grid line loss with the circuit shown in Fig. 17. The crystal voltmeters are connected to the input and output terminals of line. The loss which is calculated by the ratio of the output signal to that of input, is plotted in Fig. 21.

On the other hand the line loss was calculated from the following formula.

$$\alpha_g l = 0.5 \left( \frac{R_g}{Z_{0g}} + G_g Z_{0g} \right) l \quad (66)$$

where  $\alpha_g$ ,  $R_g$  and  $G_g$  are attenuation constant, series resistance, and parallel conductance of grid line.

### 3.1.1. Series Resistance

The series resistance of the total length of the grid wire at room temperature is  $62 \, \Omega$ . This resistance, however, increases to  $190 \, \Omega$  at the operating temperature.

These values increase further in the high frequency region because of the skin effect. This increase is estimated as 10 % at 150 Mc/s by calculation. Then we compute the loss of 1st term of Eq. (66) as follows.

at low frequency

$$0.5 \times \frac{R_g}{Z_{0g}} l = 0.5 \times \frac{190}{200} = 0.475$$

at 150 Mc/s

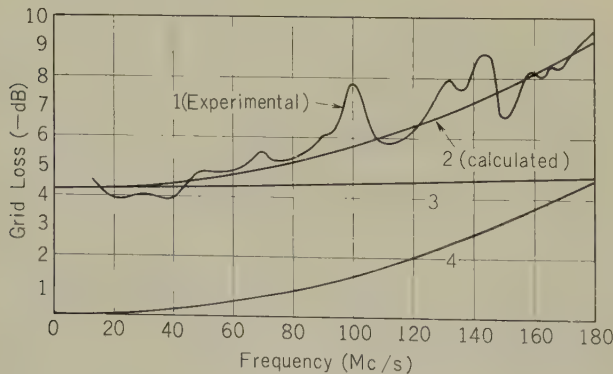


Fig. 21—Grid loss of the tube of Section 2.2.

$$0.5 \frac{R_g}{Z_{0g}} l = 0.5 \times \frac{1.1 \times 190}{200} = 0.522$$

The curve 3 in Fig. 21 represents the loss due to the 1st term of Eq. (66).

### 3.1.2. Parallel Conductance

The input conductance density per unit length of grid helix due to electron transit angle is generally given as follows. (6)

$$G_{ge} l = 2G_m f^2 T_{c-g1}^2 \quad (67)$$

where  $T_{c-g1}$  is cathode-grid electron transit time.

The transit time  $T_{c-g1}$  is given by the following expressions for the condition of zero initial velocity of electron emission.

$$\left. \begin{aligned} T_{c-g1} &= \frac{3l_{c-g1}}{v_d} \\ v_d &= 5.93 \times 10^5 \sqrt{E_d} \end{aligned} \right\} \quad (68)$$

where  $l_{c-g1}$  is grid-cathode distance and  $E_d$  is anode voltage of equivalent diode.

Substituting the values of experimental tube,  $l_{c-g1} = 150 \mu$  and  $E_d = 0.86V$ , we have  $v_d = 3.6 \times 10^5$  and  $T_{c-g1} = 1.26 \times 10^{-9}$  sec. We can compute now the loss due to 2nd term of Eq. (66), when we substitute the calculated results of Eq. (68), for each frequency. The curve 4 in Fig. 21 shows the loss due to 2nd term of Eq. (66). By superposing the curves 3 and 4 in Fig. 21, we have the calculated total loss of grid shown by curve 2 in Fig. 21. The fit of the experimental data with the calculated curve seems to be good.

### 3.2. Propagation Characteristics of Lines

Here we compare the measured line characteristics with the results calculated according to the theory of Section 1. First we give the experimental results.

#### 3.2.1. Measured Characteristics of Grid and Anode Lines

The phase constant is measured by the

method shown in Fig. 22 in which the voltmeter and ammeter are connected to the input terminal of the line and the output of the line is grounded.

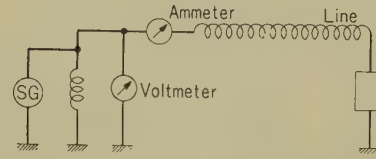


Fig. 22—Circuit for measuring phase constant of line.

The input impedance  $Z_{in}$  of such a line which can be measured by the voltmeter and ammeter varies with frequency by the following formula.

$$Z_{in} = \frac{E_{in}}{I_{in}} = \frac{Z_0}{\cot \beta l} \quad (69)$$

where  $E_{in}$  and  $I_{in}$  are input voltage and current respectively,  $Z_0$  is line characteristic impedance and  $\beta$  is phase constant of line.

In Figs. 23 (a) and (b), the measured data for the anode and grid lines respectively are shown.  $\beta$  of the grid helix increases with heating of the cathode and further increases with increase in cathode current. It is supposed that this variation of  $\beta$  is caused by the increasing parallel capacitance of the grid line with the expansion of the cathode sleeve and with the increase in cathode current.

Curve 4 in Fig. 23 (b) is plotted for the condition of matched output termination. It is observed that the best matching resistance for the two lines are as follows:

Anode line	450
Grid line	200

#### 3.2.2. Calculated Characteristics of Anode and Grid Lines

##### 3.2.2.1. Calculation of Characteristics of Grid Line

The cross-section of the gride helix is transformed to circular form shown in Fig. 24 (a). In this transformation the contour and gap



	208	206
Wave length on helix (m)	$4.09 \times 10^{-2}$	$2.07 \times 10^{-2}$

follows:

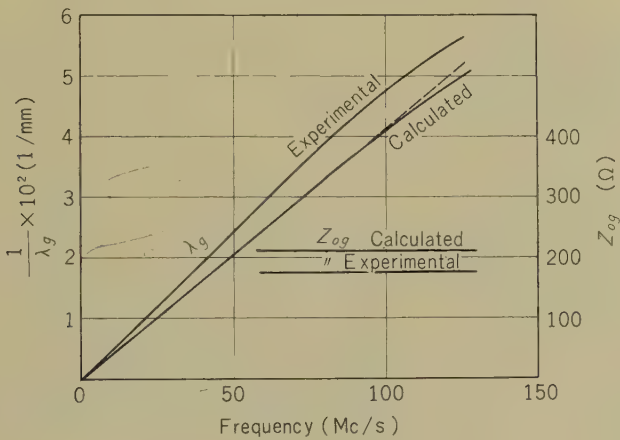
	at 60 Mc	at 100 Mc
Series inductance (H/m)	$3.27 \times 10^{-4}$	$2.60 \times 10^{-4}$
Parallel capacitance (F/m)	$6.9 \times 10^{-10}$	$7.86 \times 10^{-10}$
Characteristic impedance ( $\Omega$ )	688	575
Wave length on helix (m)	$3.5 \times 10^{-2}$	$2.21 \times 10^{-2}$

In Fig. 25 (a), the calculated and experimental results of helix characteristics are plotted. The coincidence of both results seems good.

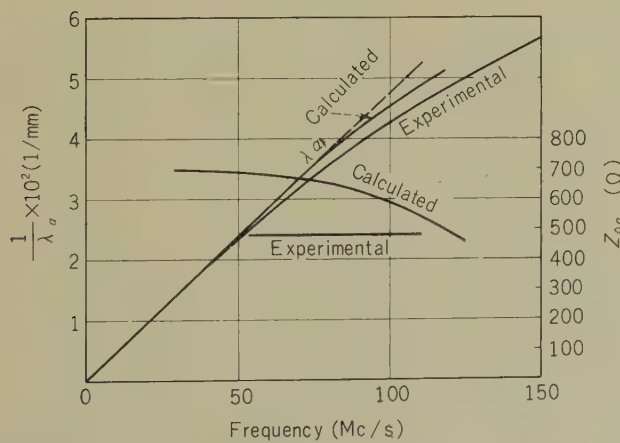
3.2.2.2. Calculation of Characteristics of Anode Line

The form of the anode helix is more complicated than that of the grid helix. However, the characteristics are calculated, in the same manner as those of the grid. The examples of final results of calculation are shown as

In Fig. 25 (b), the calculated and experimental results are plotted and the agreement of both results seems good.



(a)-Grid helix.



(b)-Anode helix.

Fig. 25—Wave length on the helix and helix characteristic impedance of tube of Section 2.2.



### 3.3. Amplification

#### 3.3.1. Effect of the Line Loss and the Difference of Propagation Velocities on Tube Gain

We have noted the loss of the grid line and the phase constants on both anode and grid lines in preceding paragraphs. Here we calculate the lowering of gain due to the above factors.

The loss of the grid helix is represented in Paragraph 3.1. The difference of phase velocities of both lines are shown in Paragraph 3.2. Now we know the propagation constants of both lines at every frequency (because phase constants vary nonlinearly as shown in Fig. 25).

The attenuation constant of the grid line and ratio of the phase constant of the grid line to that of the anode line are shown in Fig. 26. Here we assume the anode attenuation constant is zero.

Substituting the results shown in Fig. 26 into Fig. 6 we can calculate the decrease of gain from the figure. However before this substitution we must calculate the ideal gain which should be obtained from this tube. This is given by Eq. (13), by substituting  $G_m = 50 \text{ mU}$  and  $Z_{0a} = 450 \Omega$ .

Then we have the ideal gain  $N_0$

$$N_0 = 21 \text{ dB}$$

The line of ideal gain  $N_0$  in Fig. 20 (a) represents this value.

Multiplying the lowering factor which is calculated using Fig 6, to the ideal gain  $N_0$ , we have the calculated gain which is represented in Fig. 20 (a). In above calculation, the factor of dispersion of electron beams was neglected.

#### 3.3.2. Effect of Various Factors on Phase Shift

In Fig. 20 (b) measured phase difference between the input voltage and that of output is shown. We consider here the phase shift in the process of amplification of this tube. The factors which contribute to phase shift of the signal are as follows.

- 1) Signal transmission time on the line.
- 2) Electron transit time.
- 3) Phase distortion resulting from the difference of phase velocities on both lines.

Curve 1 in Fig. 20 (b) represents the phase shift obtained by calculation of factor 1 by Eq. (12). Because of the nonlinear variation of phase constant versus frequency, curve 1 does not become linear. The phase shift of factor 3 is calculated by using Fig. 26 in the same manner as described in Section 3.3.1. Curve 2 in Fig. 20 (b) represents this calculated result and curve 3 is given by superposition of curve 1 and 2.

The phase shift of factor 2 is calculated as follows. The electron transit time from cathode to control grid is  $1.26 \times 10^{-9} \text{ sec.}$  as

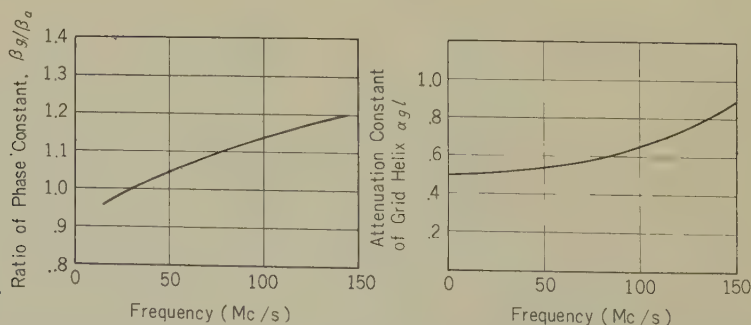


Fig. 26—Ratio of phase constants of grid and anode, and attenuation constant of grid line of tube of Section 2.2.

shown in section 3.1.2. The transit-time  $T_{g1-g2}$  from control grid to screen grid is computed by the following formula:

$$T_{g1-g2} = \frac{2l_{g1-g2}}{\sqrt{\frac{2eE_{dg2}}{m}}} \quad (70)$$

where the voltage of the control grid plane is assumed to be 0, and between control grid and screen grid

- $l_{g1-g2}$  : distance,
- $E_{dg2}$  : screen grid voltage,
- $e$  : electron charge,
- $m$  : electron mass

Substituting  $E_{dg2} = 55 \text{ V}$  and  $l_{g1-g2} = 0.44 \times 10^{-3} \text{ m}$ , we have  $T_{g1-g2} = 2 \times 10^{-10} \text{ sec}$ .

The transit time  $T_{g2-a}$  from screen grid to anode is calculated by the following formula.

$$T_{g2-a} = \frac{2l_{g2-a}}{\sqrt{\frac{2e}{m}}} \cdot \frac{1}{\sqrt{E_{da}} + \sqrt{E_{d2}}} \quad (72)$$

- where  $l_{g2-a}$  : distance between screen grid and anode
- $E_{da}$  : anode voltage

substituting  $E_{da} = 235 \text{ V}$  and  $l_{g2-a} = 4.5 \times 10^{-3} \text{ m}$ , we have  $T_{g2-a} = 6.7 \times 10^{-10} \text{ sec}$ . Then the total transit time  $T_t$  becomes  $T_t = 2.13 \times 10^{-9} \text{ sec}$ .

Curve 4 in Fig. 20 (b) represents the phase shift due to this transit time. By superposing curves 3 and 4 we obtain curve 5 which represents total phase shift. The agreement of calculated and experimental results seems good.

### Conclusion

First, theoretical considerations on the gain of distributed amplifier tubes and on the matching of line elements has been carried out.

Secondly, the lowering effect of gain caused by line losses, propagation velocity difference of grid and anode lines, and electron beam scattering has been discussed.

Thirdly, the procedure for designing helical

electrodes has been shown.

Two experimental tubes have been examined and their construction and measured characteristics have been shown in detail. One of these tubes gave the amplification band from zero to 150 Mc/s. In the last part, an analysis of function of experimental tubes has been executed by the comparison between the experimental results and the theory. The agreement between experiment and theory was good.

In the following, we wish to describe the future subjects of the distributed amplification tube. As we have seen in the analysis of experimental results, the frequency band limitation of the trial tubes was caused by the cutoff frequency of output termination networks.

To remove this frequency limitation, it will be necessary, for example, to make a output lead of coaxial line type.

Furthermore, the gain versus frequency characteristics of experimental tubes was lowered at high frequency region for the reason of grid line loss principally. To improve this sloped characteristics, it will be necessary, for example, to introduce proper positive feed-back system.

### Acknowledgment

The author takes this opportunity to express his gratitude to his many associates in the Model Shop Section. Special thanks are extended to Mr. T. Okawara, Mr. H. Huketa, and Mr. Y. Matuura for their cooperation, and also to Mr. Z. Kiyasu and Dr. M. Kuwata for their beneficial discussions.

### References

- (1) W. S. Percival "Improvements in and relating to electron discharge devices", British Pat. Spec. No. 464977, 1937.
- (2) I. A. D. Lewis "Analysis of a Transmission-Line Type of Thermionic-Amplifier Valve", *P. I. E. E.*, **100**, Part IV, No. 5, 1953-10.
- (3) T. Kojima "Unnonvean, Tube electronique a large bande," *Londe Electrique*, **39**, 392, 1959-11.
- (4) J. R. Pierce "Traveling-wave Tubes", Van Nostrand, 1950.

- (5) K. Udagawa Electr. Comm. Lab. Tech. Journ., N. T. T., 2, 3, 1953,  
 (6) K. R. Spangenberg *Vacuum Tubes*, McGraw-Hill Co., 1948.

## Appendix

Comparison between Distributed Amplifiers and Distributed Amplifier Tubes.

### 1. Amplification Frequency Upper Limit

The upper frequency limit of the distributed amplifier comes from that of tubes used. The frequency limit of tube operation comes from the lead inductance effect.

Input conductance due to the cathode lead inductance is given by,

$$G_{inL} = \omega^2 G_m L_K C_{g1-K} \quad (1)$$

Where  $G_{inL}$  : Input conductance  
 $G_m$  : Mutual conductance  
 $L_K$  : Cathode lead inductance  
 $C_{g1-K}$  : Capacitance between cathode and grid

Input capacitance increase due to the cathode lead inductance is given by,

$$C_{g1-K} = C_{g1-K,0} \frac{1}{1 - \omega^2 C_{g1-K,0} L_K} \quad (2)$$

Where  $C_{g1-K,0}$  : Low frequency capacitance between cathode and grid.

From Eqs. (1) and (2), we obtain the increase of input capacitance and conductance at high frequency. Especially, input capacitance increases rapidly when frequency approaches

the resonant frequency. For the above reasons distributed amplifiers constructed with common receiving tubes have an upper limitation of amplification band which estimated 300 – 400 Mc/s by best tube.

On the contrary, the distributed amplifier tube has no lead inductance, thus, free from any troubles proper to it and in principle it has no limitation of amplification band.

### 2. Simplicity of Operation

The adjustment of distributed amplifiers composed of many common tubes is not easy. On the contrary the distributed amplifier tube needs no adjustment.

### 3. easiness of Realization of High Gain

As shown in Section 1, the gain of distributed amplification is proportional to the anode line characteristic impedance. This impedance of common distributed amplifier, however, can not be made very large because the cutoff frequency of the anode line, which is composed of tandem low pass filter, determines the maximum anode line impedance at given output capacitance of tubes. On the contrary the anode line impedance of distributed amplifier tube can be designed large enough to get sufficient high gain with one tube.

### 4. Dimensions

The dimensions of the distributed amplifier tube is remarkably smaller than that of a distributed amplifier of the same gain-bandwidth characteristics.

\* \* \* \*



# The Magnetic Circuit of Telephone Receiver\*

Ryozo ARAKI† and Tatsuo SHIMAMURA†

*In designing the electromagnetic driving system of the telephone receiver, it is necessary that we should be able to estimate the force factors, the magnetic attractive force, etc., from the dimensions, the shapes, and the materials of the magnetic circuit. There has not been, however, sufficient information available in the past; therefore we have obtained the necessary data through systematic experiments. This paper describes the outline of these experiments, and besides, an example of design to which the results of these experiments are applied is given.*

## Introduction

The development of a new type telephone set is now in progress in this country; and therefore, the development of receivers is now going on. Due to the fact, however, that fundamental research has not advanced sufficiently, little is known today about the effect of dimensions, materials and shapes on the characteristics of the magnetic circuit of receivers. Therefore we have obtained experimentally data necessary for the design of the concentric type magnetic circuit, the type of magnetic circuit considered most suitable to manufacture in this country, and which is also used in the present standard R4 receiver. For an outline of the design of the receiver including the vibrating system to which the results of these experiments have been applied, please refer to a previous paper.<sup>(1)</sup>

Finally we give an example of design and show that we should increase the coupling coefficient\*\* of the magnetic circuit and increase the electromechanical coupling factor\*\*\* in order to obtain higher efficiency from the receiver.

## 1. Design of Experiments

The experiments were carried out using an orthogonal array  $L_{27} (3^{13})$ ; and the force factor A, magnetic attractive force F, etc. of 27 magnetic circuits as shown in Fig. 1 were measured. The factors thus considered are shown in Table I. These factors, with the exception of the factor (f), relate to the construction of the magnetic circuit, and it is necessary to know their effect on the characteristics of the magnetic circuit. Besides these factors, there are other factors to be considered, but they are excluded because their effects on the characteristics are small or are already known. For example, although it is a concentric type magnetic circuit the ring armature type magnetic circuit was excluded from these experiments. This was because the ring armature magnetic circuit is disadvantageous, as the magnetic attractive force F is too large for the case where the magnetic gap length is zero, thus special devices are required to prevent the adhesion of the diaphragm to the pole pieces.

For these factors, the main effect of frequency (factor f) has been obtained through three measurements for each magnetic circuit, and the main effect of armature thickness (factor I) through the measurement of three magnetic circuits. The dimensions of the pole pieces are important as they affect the armature mass, and the diameter of the armature

\* Published in the Journal of the Institute of Electrical Communication Engineers of Japan, Vol. 43, No. 8, p. 894-900, 1960.

† Station Apparatus Research Section.

\*\* This term has the same meaning as when applied to transformers.

\*\*\* This term has the same meaning as when applied to piezoelectric transducers.



can be shortened without reducing voice coil space if the outer pole piece is bent. The outer pole pieces were all 1 mm thick, and the outer diameter of the unbent outer pole pieces were 17.5 mm. Barium ferrite was used as the permanent magnet and was demagnetized to the extent that the force factor became maximum at  $g=0.15$  mm. If it is thus demagnetized, the characteristics, it seems, are not much affected by the dimensions and the materials of the magnet. The material of the armatures were all permendur melted in vacuum. The use of permendur melted in vacuum is helpful to increase the force factor. The dimension of the beveling of the pole face edge is  $0.5\text{ mm} \times 0.5\text{ mm}$  and the number of turns and d.c. resistance of the voice coil is 500 turns and 30 ohms.

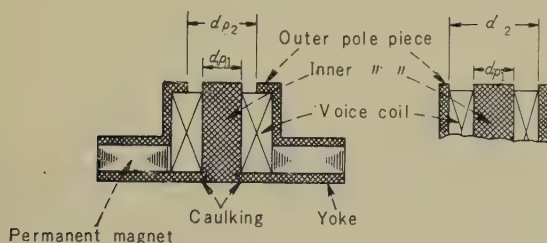


Fig. 1—Concentric type magnetic circuit (armature removed).

## 2. Measurements

The magnetic circuit was coupled to an electrostatic transducer, and the force factor  $A$  of the magnetic circuit was measured by the reciprocity method. Fig. 2 shows the apparatus, to the top of which was fitted a micrometer in order to adjust the distance between the armature and the pole faces. The armature is attached to the center of the diaphragm of the electrostatic transducer. Diaphragm impedance necessary to calculate force factor by the reciprocity principle has been obtained by measuring the variation of the resonant frequency of the diaphragm caused by added mass. The center of the diaphragm is a rigid disc, its resonant frequency being approximately 1,800 c.p.s.. Magnetic

attractive force  $F$  was simultaneously obtained by measuring, with this apparatus, the variation of the capacity of the electrostatic transducer. The diaphragm was changed as necessary so that displacement of diaphragm by magnetic attractive force would remain within 0.01 mm.

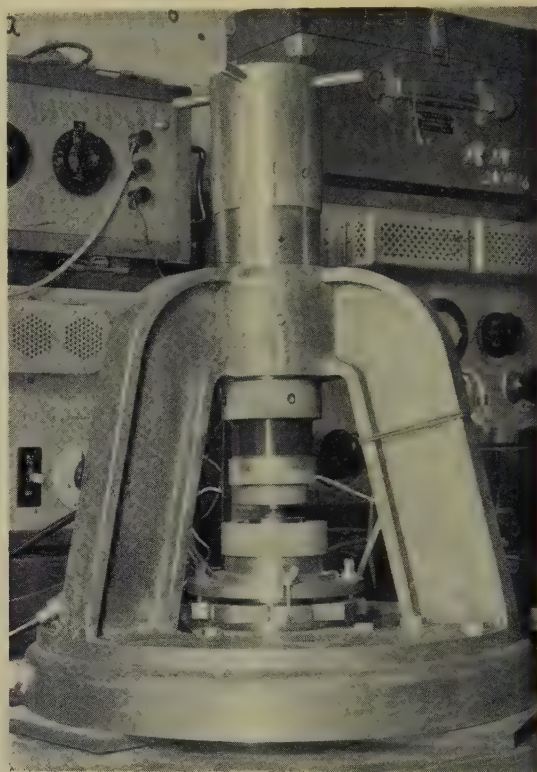


Fig. 2—Apparatus for force factor measurement.

The advantages of this apparatus are: (1) frequency and gap length characteristics of force factor, etc. can be readily measured; (2)  $F$  and electrical impedance etc. can be measured simultaneously with  $A$ , with the magnetic circuit remaining on the apparatus, and thus these gap length characteristics can be compared with each other. Fig. 3 gives an example, where it is easily observed that  $A$  and the negative stiffness  $s_n = -(\partial F / \partial g)$  reach their maximum at the same gap length  $g_m$ . In the figure,  $F^{-1/2}$  is used to obtain  $F_0$  ( $F$  at  $g=0$ ). It is further noted that the

straight line of  $F^{-1/2}$  bends near the gap length  $g_m$ . The levels of the factors of the magnetic circuit shown in the Fig. 3 are  $A_2, B_3, C_2, D_1, E_3, F_3, G_1, H_3$ . ( $A_2$  means  $dp\ 2/dp\ 1=1.86$ . See Table 1.)

3. Experimental Results

To design the receiver, the designer should know what effects the factors in Table I will have on  $A, A/\sqrt{Zd}$  ( $Zd$ : damped impedance),  $F_0, F_{0.15}$  ( $F$  at  $g=0.15$  mm) and  $s_n$ . In Table II are shown the main effects of factors found to be significant on the characteristics at  $g=0.15$  mm. In this table, only the factors found to be significant are shown, and interactions among them are negligible. The table may be used in estimating  $A/\sqrt{Zd}$ , etc. from the levels of the factors of the magnetic circuit to be considered. The estimate corresponding to each level may be obtained by multiplying or adding the respective values in the table to  $m$ ; e.g. in Fig. 3,  $20\log(A/\sqrt{Zd})$  at 1,000 c.p.s. will be estimated as follows:

+2.24+0.73+1.33+1.70+6.25=12.25 dB

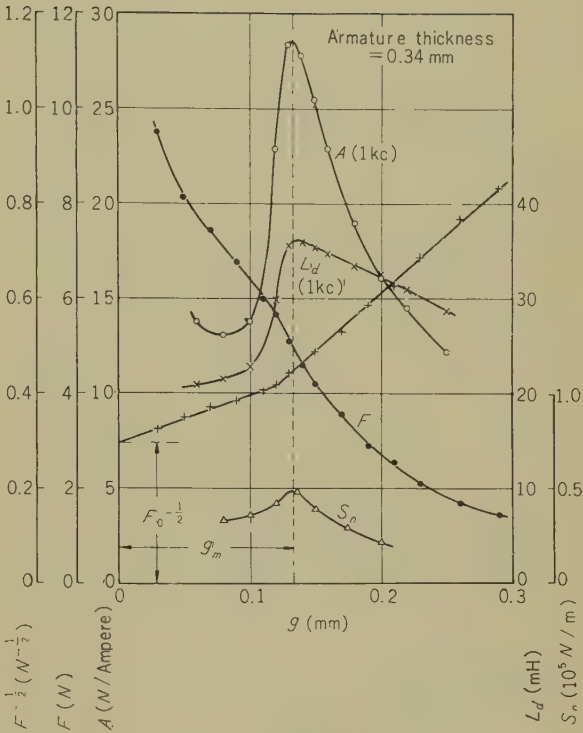


Fig. 3—Typical gap length characteristics of the driving system.

Table 1  
FACTORS AND LEVELS OF MAGNETIC CIRCUIT EXPERIMENT

Factors		Levels		
		1	2	3
$d_{p2}/d_{p1}$	A	2.19	1.86	1.57
$d_{p1}$	B	6 mm	5 mm	7 mm
Outer Pole Piece	C	Bent	Not bent	Bent
Outer Diameter	D	$d_{p2}+2$ mm	$d_{p2}$	$d_{p2}$
Inner //		0	0	$d_{p1}-2$ mm
Inner Pole Piece and Yoke	E	Caulked	One block	Caulked
Voice Coil Length (net)	F	5 mm	7 mm	7 mm
Pole Face	G	Not beveled	Beveled	Not beveled
Materials	H	45 Permalloy	1% Si Iron	45 Permalloy
of {Inner Pole Piece Outer // // }		Pure iron	Pure iron	
Thickness of Armature	I	0.40 mm	0.34 mm	0.26 mm
Frequency	f	180 c/s	1,000 c/s	2,500 c/s

Table 2

MAIN EFFECTS OF FACTORS

The estimates corresponding to each level will be obtained by multiplying or adding each figure to  $\bar{m}$ .

(a) Force Factor

$\bar{m}=13.34\text{ N/Ampere}$   
1% Confidence Interval:  $\times 0.69\sim\times 1.44$

Factors	Levels		
	1	2	3
B	$\times 1.035$	$\times 0.832$	$\times 1.161$
D	$\times 1.248$	$\times 0.832$	$\times 0.963$
H	$\times 1.066$	$\times 0.723$	$\times 1.297$
I	$\times 1.081$	$\times 1.000$	$\times 0.749$
f	$\times 1.292$	$\times 1.007$	$\times 0.768$

(b)  $20\log(A/\sqrt{Z_a})$

$\bar{m}=+2.24\text{ dB, re }1\text{N}/\sqrt{\text{Watt}}$   
1% Confidence Limits:  $\pm 2.71\text{ dB}$

Factors	Levels		
	1	2	3
B	+0.25	-0.98	+0.73
D	+1.33	-1.42	+0.09
H	+0.55	-2.25	+1.70
I	+0.74	0	-2.43
f	+6.25	-0.55	-5.71

(c)  $F_0$

$\bar{m}=11.94\text{ N}$   
1% Confidence Interval:  $\times 0.72\sim\times 1.39$

Factors	Levels		
	1	2	3
B	$\times 1.035$	$\times 0.820$	$\times 1.178$
D	$\times 0.952$	$\times 0.754$	$\times 1.393$
I	$\times 1.096$	$\times 1.000$	$\times 0.510$

(d)  $F_{0.15}$

$\bar{m}=4.45\text{ N}$   
1% Confidence Interval:  $\times 0.83\sim\times 1.21$

Factors	Levels		
	1	2	3
B	$\times 0.978$	$\times 0.895$	$\times 1.143$
D	$\times 0.944$	$\times 0.944$	$\times 1.119$
I	$\times 1.213$	$\times 1.000$	$\times 0.592$

(e)  $s_n$

$m=0.378\times 10^5\text{ N/m}$   
1% Confidence Interval:  $\times 0.83\sim\times 1.21$

Factors	Levels		
	1	2	3
D	$\times 1.033$	$\times 0.759$	$\times 1.276$
E	$\times 1.069$	$\times 0.875$	$\times 1.069$
I	$\times 1.119$	$\times 1.000$	$\times 0.484$

which agrees with the actual value of 12.36 dB within confidence limits.

From the above results, we may reach the following conclusion regarding the respective factors in Table 1:

(A)  $d_{p2}/d_{p1}$ : This, not being significant for any characteristics, should be small to make the armature diameter short, so long as the leakage flux between inner and outer pole pieces is not too large.

(B)  $d_{p1}$ : As the diameter of the inner pole piece becomes larger,  $A$ ,  $A/\sqrt{Z_d}$ , and  $s_n$  increase. However, as armature mass increases accordingly, these effects should be carefully weighed considering the vibrating system. The previous paper<sup>(1)</sup> shows that the specific response† of the receiver does not change very much for  $d_{p1}$  within the range of 5~7 mm, but small  $d_{p1}$  is convenient to prevent

† In this country, the term “specific response” is used to denote the sensitivity of the telephone receiver. The definition is as follows:

specific response  $k_R=20\log p/\sqrt{P}$ ,  
where  $p$ : induced sound pressure  
 $P$ : electrical apparent input power.



the adhesion of the diaphragm to the pole pieces.

(C) Though the outer pole piece is bent, characteristics are not much affected. Thus, securing the voice coil by bending as above and to decreasing  $d_{p2}/d_{p1}$  and armature mass are helpful in obtaining higher sensitivity.

(D) It is not desirable to bore a comparatively large hole in the center of the armature or to make the outer diameter equal to  $d_{p2}$ .

(E) Characteristics will not be very different whether the inner pole piece and the yoke are made into a block or fixed by caulking.

(F) Coil length, either 5 mm or 7 mm, does not have a major effect on the characteristics of the magnetic circuit.

(G) As the effect of the pole face beveling is little, it is better, judging from the point of view of manufacturing not to bevel the pole face.

(H)  $A$  and  $A/\sqrt{Z_d}$  are much affected by the pole piece materials, while  $F$  and  $s_n$  are not. It is thus more advantageous to make both the inner and outer pole pieces of 45 permalloy or, to reduce costs, to make the latter only of pure iron.

(I) The thicker the armature is, the more  $A$ ,  $A/\sqrt{Z_d}$  and  $s_n$  increase. The mechanical vibrating system, however, should be taken into consideration, as the armature mass will increase correspondingly. The previous paper<sup>(1)</sup> shows that the thicker the armature is, the more the specific response will increase.

(J) Frequency:  $A/\sqrt{Z_d}$  is nearly proportional to the reciprocal of the square root of the frequency. Thus, the frequency response should be compensated by the mechano-acoustic vibrating system.

4. Comparison of Some Examples of Receivers with the Ideal Receiver

An example of a design where the results shown in the foregoing paragraphs as well as in the previous paper<sup>(1)</sup> are applied is given in Table III, together with a comparison with the present standard R4 receiver. The example, however, is a paper design and not an actual case of manufacture. Therefore the

receiver actually used for the new type telephone set will be different in respect to cost and stability, and the specific response will be lower than the value in Table III. In order to know how the example should be improved, in comparison with the R4 receiver, we shall work out sample calculations below. As is generally known, the specific response<sup>(2)</sup> of the ideal receiver is

$$k_{R0} = \frac{p}{\omega} = \sqrt{\frac{\kappa}{\omega V_{-2}}} \tag{1}$$

- where
- $p$ : Sound pressure induced in acoustic load chamber (microbar)
  - $\omega$ : Input apparent power (watt)
  - $k$ : Bulk modulus of the air
  - $V_{-2}$ : Volume of the acoustic load chamber

And, the specific response of receiver at low frequencies will be:

$$k_R = k_{R0} \cdot \sqrt{\frac{Z_d}{Z}} \cdot \sqrt{\frac{\omega L_d}{Z_d}} \cdot \frac{A}{\sqrt{s_n L_d}} \cdot \sqrt{\frac{s_n}{s_a}} \times \frac{\sqrt{s_a s_{-2}}}{s_0'} \cdot \frac{V_{-2}}{V_f} \tag{2}$$

Table 3

COMPARISON BETWEEN THE PRESENT STANDARD R4 RECEIVER AND EXAMPLE

(a) Specific Response and Losses at 180 c/s (dB)

	the R4 Receiver	Example
$k_{R0}$	93.21	93.21
$\sqrt{Z_d/Z}$	} -0.88	-1.03
$\sqrt{\omega L_d/Z_d}$		-1.40
$A/\sqrt{s_n L_d}$	-2.79	-2.25
$\sqrt{s_n/s_a}$	-9.24	-2.07
$\sqrt{s_a s_{-2}}/s_0'$	-6.66	-2.15
$V_{-2}/V_f$	-5.26	-4.57
$R_R$	68.37	79.74

Specific Response: dB, re  $1\mu\text{b}/\sqrt{\text{Watt}}$ .



(b) Design Factors and Constants

	the R4 Receiver	Example
Thickness of the Armature (mm)	0.34	0.40
Diameter of the Armature (mm)	16.5	12.5
$d_{p1}$ (mm)	7	6
$d_{p2}$ (mm)	13.0	10.5
Material of the Armature	Permendure	Permendure Melted in Vacuum
Material of the Inner Pole Piece	45 Permalloy	45 Permalloy
Material of the Outer Pole Piece	Pure Iron	45 Permalloy
$A$ (N/Ampere)	18.5	31.21
$L_d$ (mH)	32.5	35.0
$s_n$ ( $10^5$ N/m)	0.20	0.467
$Z$ (Ohm)	45.0	54.7
Armature Mass (g)	0.60	0.403
Stiffness of the Diaphragm, $s_a$ ( $10^5$ N/m)	1.68	0.752
Effective Mass of the Diaphragm,* (g)	1.20	0.575
Total Volume of the Fore Chamber, $V_f$ (cm <sup>3</sup> )	11.0	10.16
Total Volume of the Rear Chamber, (cm <sup>3</sup> )	16.5	12.19

\* Armature mass is included.

where

- $Z$ : Free impedance of the receiver
- $Z_d$ : Damped impedance of the receiver
- $L_d$ : Damped inductance of the receiver
- $s_n$ : Negative stiffness
- $A$ : Force factor
- $s_a$ : Stiffness of the diaphragm
- $s_{-2}$ : Stiffness of the acoustic load chamber
- $V_f$ : Total volume of the fore chamber
- $s_0' = s_a - s_n +$  (stiffness of the fore and rear chambers)

No factors in eq. (2), except  $\sqrt{s_a s_{-2}}/s_0'$ , are larger than 1.  $A/\sqrt{s_n L_d}$  and  $\sqrt{s_n/s}$  are called the coupling coefficient of magnetic circuit and the electromechanical coupling factor, respectively. Table 3 shows examples of these factors.

From this it follows that the defects of the present standard R4 receivers are that the electromechanical coupling factor and  $\sqrt{s_a s_{-2}}$

$/s_0'$  are too small, as effective mass and  $s_a$  of the diaphragm are large. In the example, however, losses are approximately the same amount, and no serious defects are noticeable. That is, compared with the R4 receiver, the principal improvements are that the armature is lighter in weight, and thus the effective mass and the  $s_a$  of the diaphragm are made small. Further as a magnetic circuit of larger  $s_n$  was used,  $s_a$  and  $s_n$  near the value of  $s_{-2}$ . It may be said in short that it is required to increase both the coupling coefficient of magnetic circuit,  $A/\sqrt{s_n L_d}$  and the electromechanical coupling factor  $\sqrt{s_n/s_a}$ .

Conclusion

In this paper it is shown how the characteristics of the driving system of a practical receiver are affected by the dimensions, the materials and the shapes of the magnetic

circuit. Although this report is brief, it is being published because no other data of this type is available in prints.

#### Acknowledgement

The authors wish to acknowledge the valuable suggestions and the advice kindly given by Dr. T. Hayasaka, Dr. K. Masuzawa, Dr. G. Ito and Mr. Shinohara regarding the design

of these experiments.

#### References

- (1) G. Ito and R. Araki, "Design of the Telephone Transmitter and the Receiver," *Reports of the E.C.L., N.T.T.* **7**, 7, pp. 218-227, July, 1959.
- (2) E.E. Mott and R.C. Miner, "The Ring Armature Telephone Receiver," *B.S.T.J.*, **30**, pp. 110-140, Jan., 1950.

\* \* \* \*

U.D.C. 665.335.5.067 : (621.315.615 : 621.319.4)

## Refining of Castor Oil for Capacitor Dielectrics\*

Masaaki KATAGIRI† and Katunari KODATI†

*The authors developed a simple method of refining castor oil by using active clay and active alumina. Castor oil refined by this method has good electrical properties suitable for capacitor dielectrics.*

## Introduction

There is a general tendency to make communications equipment more compact and more durable; therefore, capacitors using liquid impregnating materials are being used in place of capacitors using solid or semi-solid impregnants. Castor oil is an especially attractive liquid impregnating material because of its high dielectric constant. But not method of refining castor oil for use as a capacitor dielectric has been published in Japan.

The authors assumed that the impurities in unrefined castor oil consist of free fatty acid, water and compounds with OH radicals; and developed a simple refining method using active clay and active alumina which are not corrosive to metal.

Castor oil refined by this method has a small acid value and good electrical properties, and contains only a small amount of compounds with OH radicals.

The results have shown that the above assumption was valid.

## 1. Properties of Commercially Available Castor Oil

The authors used eleven samples taken from commercially available unrefined castor oils. The chemical and electrical properties

of these samples are shown in Table 1 and in Fig. 1-Fig. 3.

Table 1

CHEMICAL PROPERTIES OF CASTOR OIL

Sample	Acid Value	Saponification Value	Iodine Number	Acetyl Value
1	0.88	182.4	85.99	143.7
2	0.35	181.2	84.2	142.9
3	0.44	179.8	85.5	142.8
4	0.42	181.3	85.8	145.1
5	0.40	180.5	85.8	146.8
6	0.45	182.5	85.2	144.3
8	0.30	182.1	85.2	144.6

The acid value of castor oil is an important indicator of its degree of oxidation and of the amount of free fatty acid contained in it. The acid values of these samples ranged from 0.3 to 0.8. The volume resistivity and the dielectric constant are functions of temperature. The minimum value of loss tangent at 1 kc/s was observed near 20°C.

\* MS in Japanese received by the Electrical Communication Laboratory, April 30, 1960. Originally published in the *Kenkyū Zituyōka Hōkoku (Electrical Communication Technical Journal)*, N.T.T., Vol. 9, No. 5, pp. 125-138, 1960.

† Plastics Application Research Section.

2. Refining Castor Oil

The authors assumed that the impurities in crude castor oil consisted of free fatty acid, mucilage, protein, dusts, OH compounds, colored impurities, ash, water, etc. Most of these impurities are be removed in conventional refining processes. However, even after conventional refining there still remains a small quantity of impurities which deteriorate the electrical properties of castor oil.

The authors refined commercial castor oil by using active clay and or active alumina. The effect of the refining was evaluated chiefly in terms of electrical properties,

2.1. The Effects of the Use of Active Clay

Clay which had been activated at  $135 \pm 5^\circ$

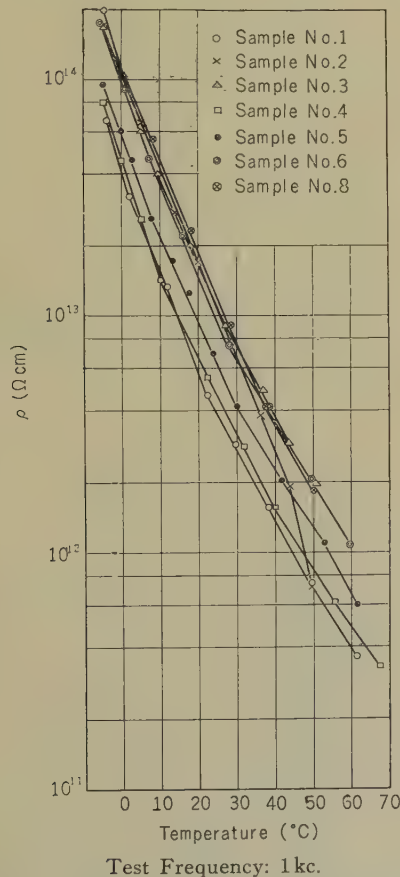


Fig. 1—Volume resistivity of commercial castor oil.

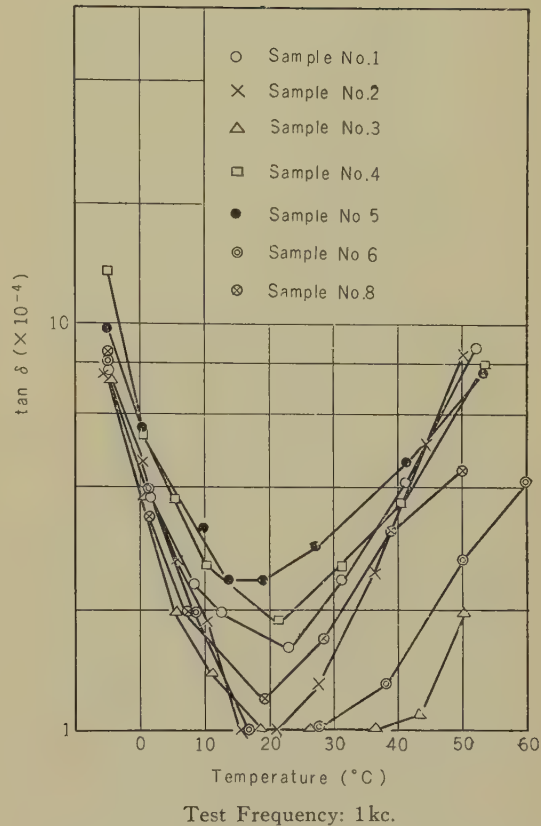


Fig. 2—Dielectric loss tangent of commercial castor oil.

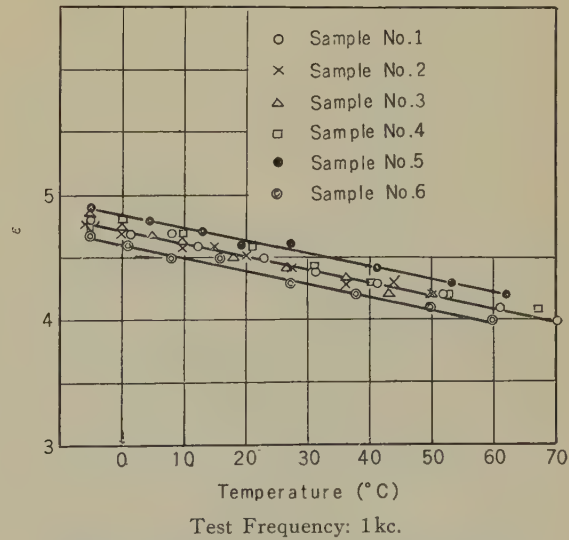
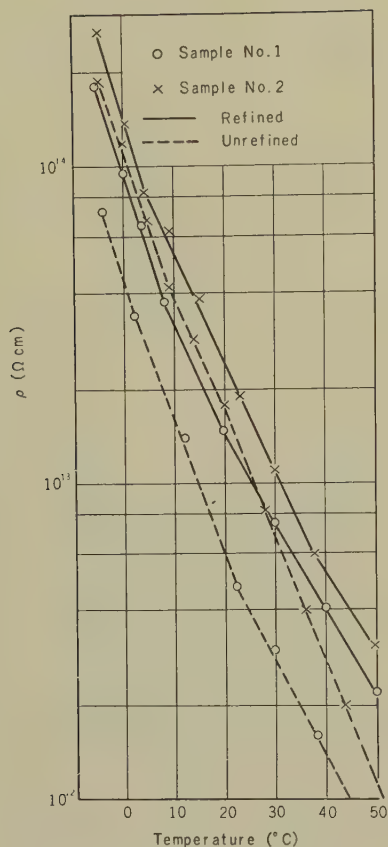


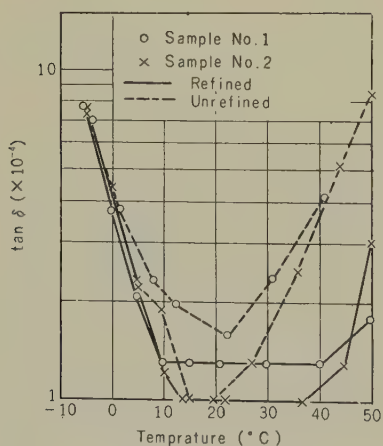
Fig. 3—Dielectric constant of commercial castor oil.





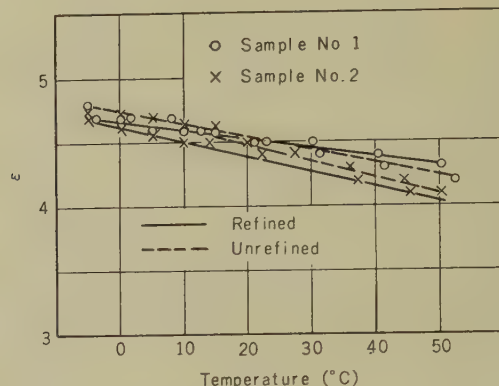
Test Frequency: 1 kc.

Fig. 4—Volume resistivity (using active clay).



Test Frequency: 1 kc.

Fig. 5—Dielectric loss tangent (using active clay).



Test Frequency: 1 kc.

Fig. 6—Dielectric constant (using active clay).

C for three hours was mixed with samples No. 1 and No. 2, by ten percent of the samples in weight. These mixtures were heated and stirred in a temperature range from 80 to 100°C for one hour. The effects of this refining process are shown in Fig. 4–Fig. 6.

## 2.2. The Effects of the Use of Active Alumina

The apparatus for this method of refining is illustrated in Fig. 7.

The amount of active alumina was about 100 grams and the amount of castor oil treated was 1 l/hour. The castor oil was heated

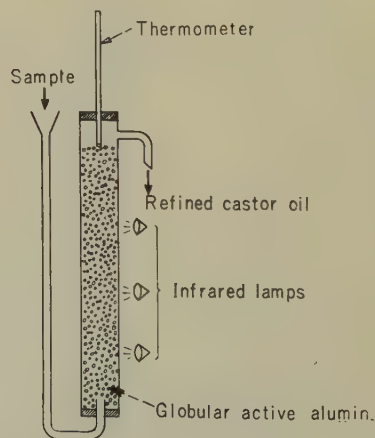


Fig. 7—Percolation method.

by infrared lamps to 80–85°C during the process of refining. In this method, the castor oil was refined twice. Its electrical properties are shown in Fig. 8–Fig. 10.

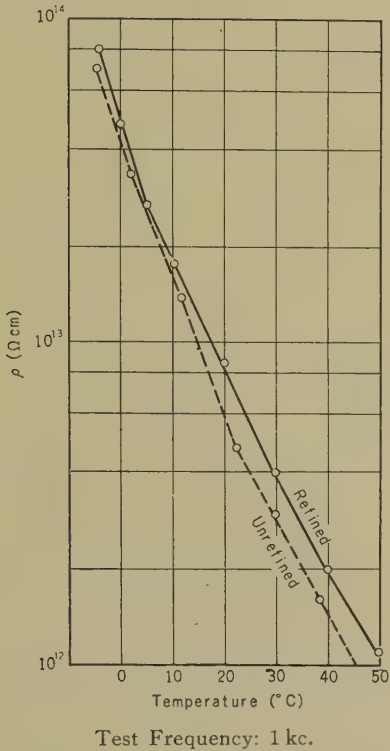


Fig. 8—Volume resistivity (using active alumina).

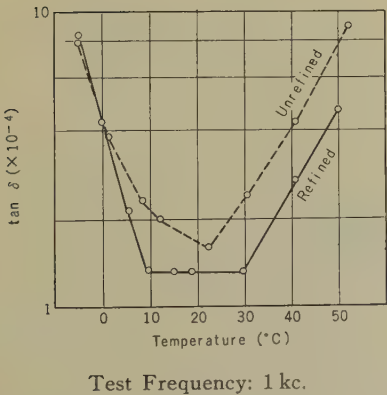


Fig. 9—Dielectric loss tangent (using active alumina).

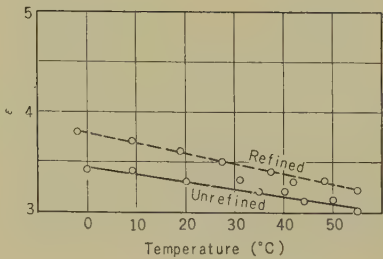


Fig. 10—Dielectric constant (using active alumina).

2.3. The Effects of the Use of Both Active Clay and Active Alumina

Both activated clay and alumina were mixed with samples No. 1, No. 2, No. 4 and No. 5, by ten percent of the samples in weight respectively. These mixtures were heated and stirred at a temperature from 70 to 80°C for an hour, and then filtered. The effects of his refining process are illustrated in Fig. 11–Fig. 13.

From many experiments, the authors found that the following conditions were very good:

- active clay..... 10 %
- active alumina ..... 10 %
- temperature for treatment... 70° C
- time of treatment.....one hour.

Table 2 indicates the electrical properties of the castor oil refined by this method.

2.4. Comparison of the Methods

Fig. 14 shows the electrical properties of sample No. 1, and Table 3 indicates the chemical properties of each sample.

From the above Figure and Table, the method of using both active clay and alumina is known to be most effective.

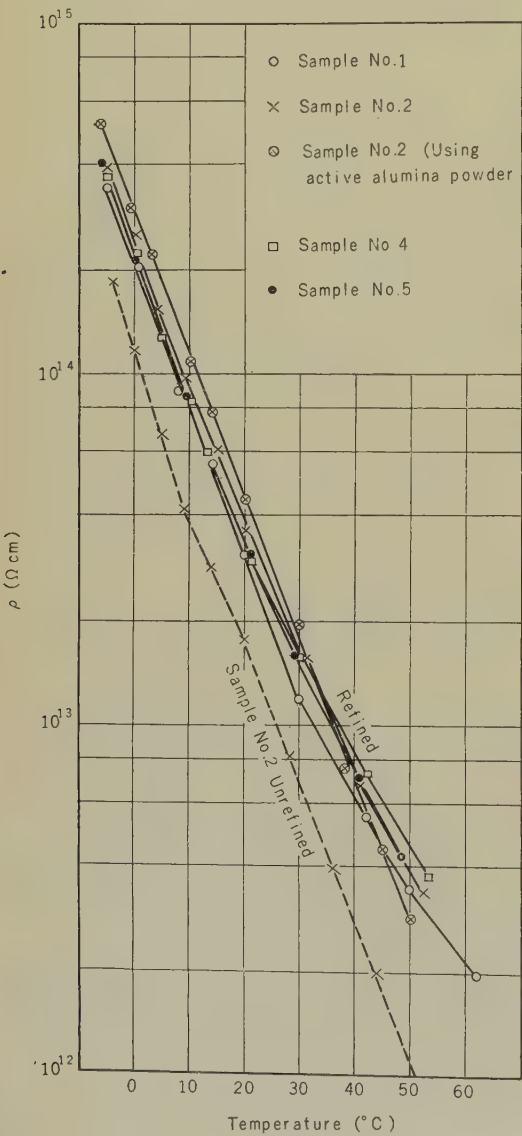
3. Deterioration by Heating

Many samples, both refined and unrefined, were heated under the following conditions:

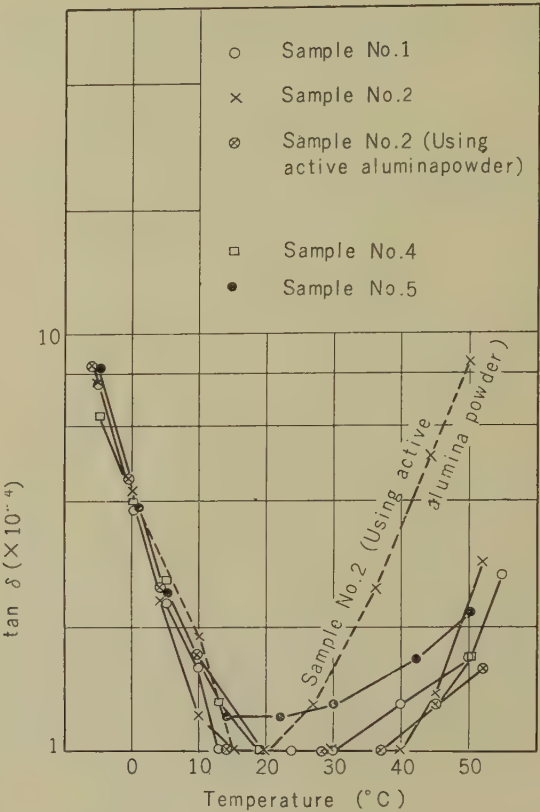
pressure ..... 1-2 mm Hg  
temperature .....  $105 \pm 3^{\circ}\text{C}$   
time of heating ..... three hours.

The results are shown in Fig. 15-Fig. 17.

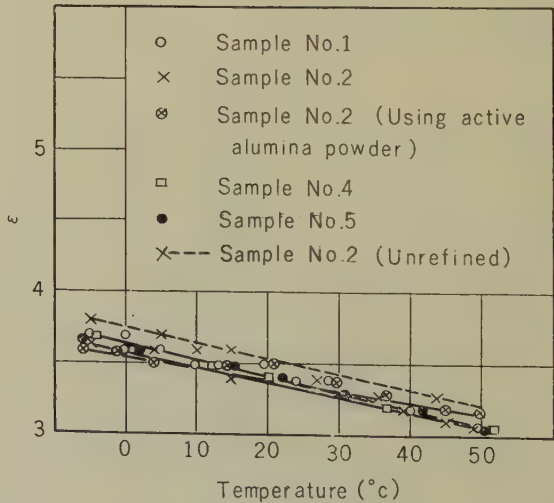
The samples No. 9 and No. 10 were heated for 6-12 hours under the same pressure. None of the samples deteriorated during the first three hours, but after six hours the deterioration was remarkable.



Test Frequency: 1kc.  
**Fig. 11**—Volume resistivity (using both active clay and alumina).



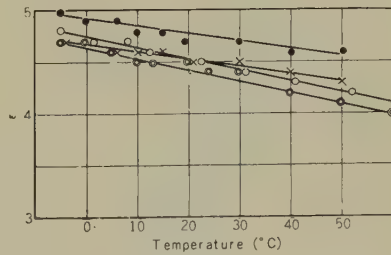
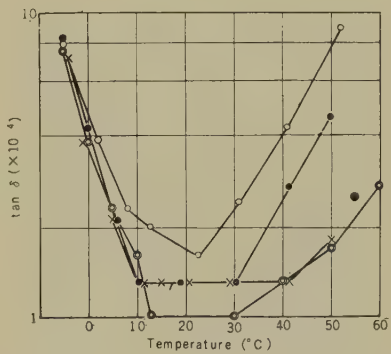
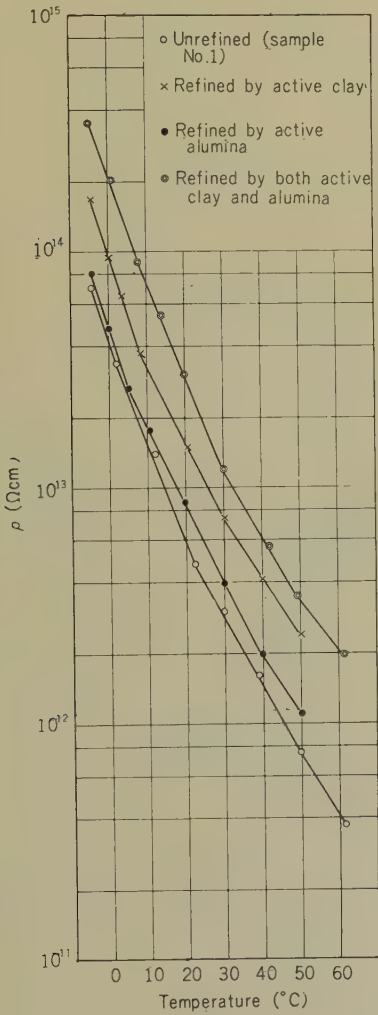
Test Frequency: 1kc.  
**Fig. 12**—Dielectric loss tangent (using both active clay and alumina).



Test Frequency: 1kc.  
**Fig. 13**—Dielectric constant (using both active clay and alumina).

Table 2  
ELECTRICAL PROPERTIES OF (REFINED) CASTOR OIL

Temp. (°C)	Acid Value		Volume Resistivity (Ω cm)		Dielectric Loss Tangent (×10 <sup>-4</sup> ) (1 kc)		Dielectric Constant (ε) (1 kc)	
	Unrefined	Refined	Unrefined	Refined	Unrefined	Refined	Unrefined	Refined
0	0.35~0.45	0.16~0.35	×10 <sup>13</sup> 4.0~9.0	×10 <sup>14</sup> 2.0 <	4~5.5	4.5>	4.8	4.6<
30			×10 <sup>12</sup> 3.0~8.0	×10 <sup>13</sup> 1.5 <	1~3.0	1.5>	4.4	4.3<
60			×10 <sup>11</sup> 4.0~9.0	×10 <sup>12</sup> 2.0 <	4~1.2	5 >	4.1	4.0<



Test Frequency: 1kc.

Fig. 14—Electrical properties of castor oil.



Table 3

CHEMICAL PROPERTIES OF CASTOR OIL

Sample	Acid Value		Saponification Value		Iodine Number		Acetyl Value		Refined Method
	Unrefined	Refined	Unrefined	Refined	Unrefined	Refined	Unrefined	Refined	
2	0.35	0.35	181.2	183.6	84.2	89.1	142.9	132.6	Both active clay and alumina
6	0.45	0.17	182.5	182.5	85.8	87.35	146.8	139.7	Same as above
8	0.30	0.16	182.5	181.5	85.2	86.81	144.6	145.1	Same as above
3	0.44	0.44	179.8	181.2	85.5	84.2	142.8	142.9	Active alumina only
2	0.35	1.00	181.2	181.1	84.2	88.3	142.9	133.0	Active clay only

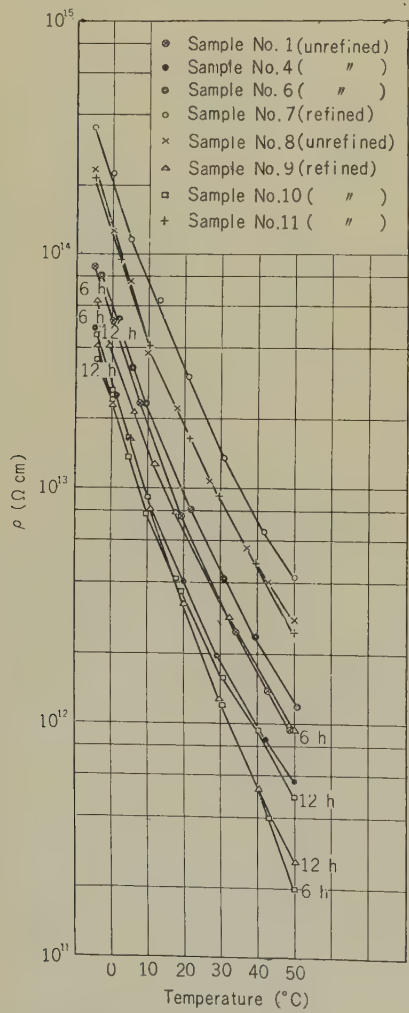


Fig. 15—Volume resistivity by heating.

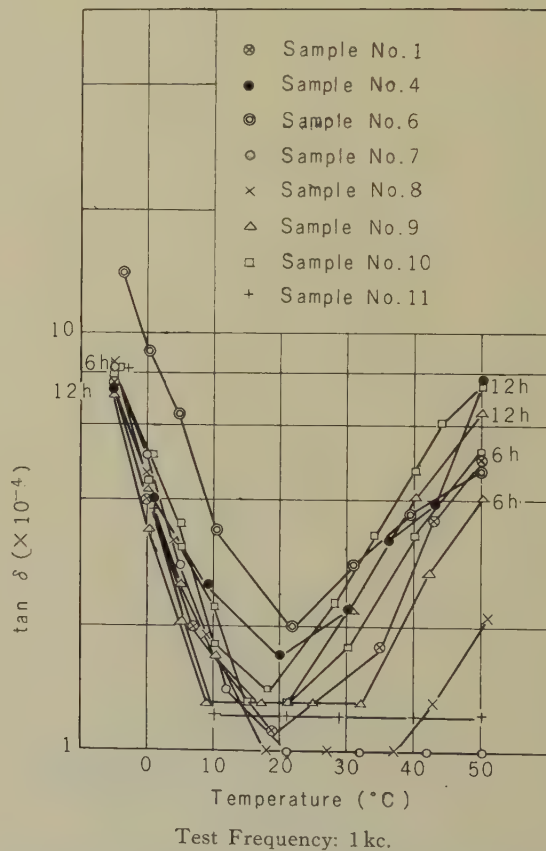


Fig. 16—Dielectric loss tangent by heating.

Table 4

IMPREGNATION OF CAPACITOR PAPER WITH REFINED CASTOR-OIL

Electrical Properties	Capacitor Paper Dry (105° C 3 Hours)	Refined Castor Oil (Sample No. 2)	Capacitor Paper Impregnated with Refined Castor Oil at 105°C for 3 Honrs)	Capacitor Paper Impregnated with Refined Castor Oil (75 %) and CCl <sub>4</sub> (25 %) at Room Temperature
Volume Rstivity (Ω-cm)	2. 4-4. 4×10 <sup>16</sup>	3. 7×10 <sup>13</sup>	5. 7×10 <sup>13</sup> -2. 9×10 <sup>14</sup>	3. 1×10 <sup>13</sup> -1. 2×10 <sup>14</sup>
Dielectric Loss Tangent (1 kc)	0. 0051-0. 0057	0. 010	0. 0074-0. 0109	0. 0076-0. 0127
Dielectric Constant (1 kc)	1. 4	4. 4	4. 4-4. 5	3. 3-3. 8

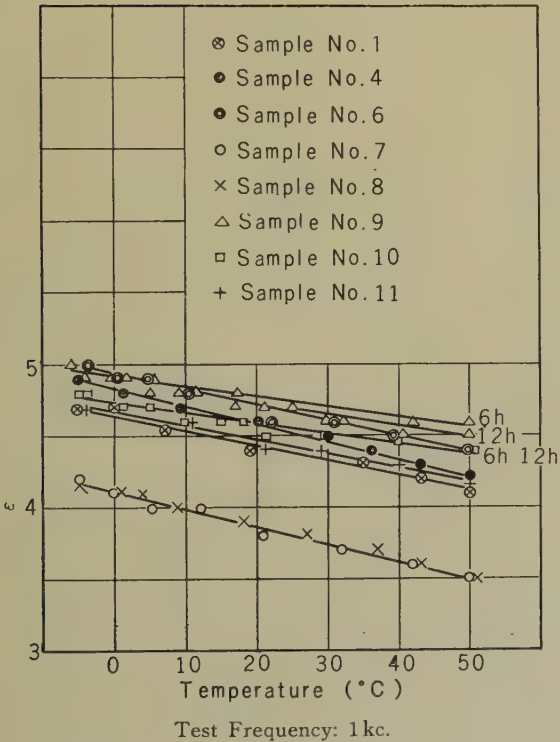


Fig. 17—Dielectric constant by heating.

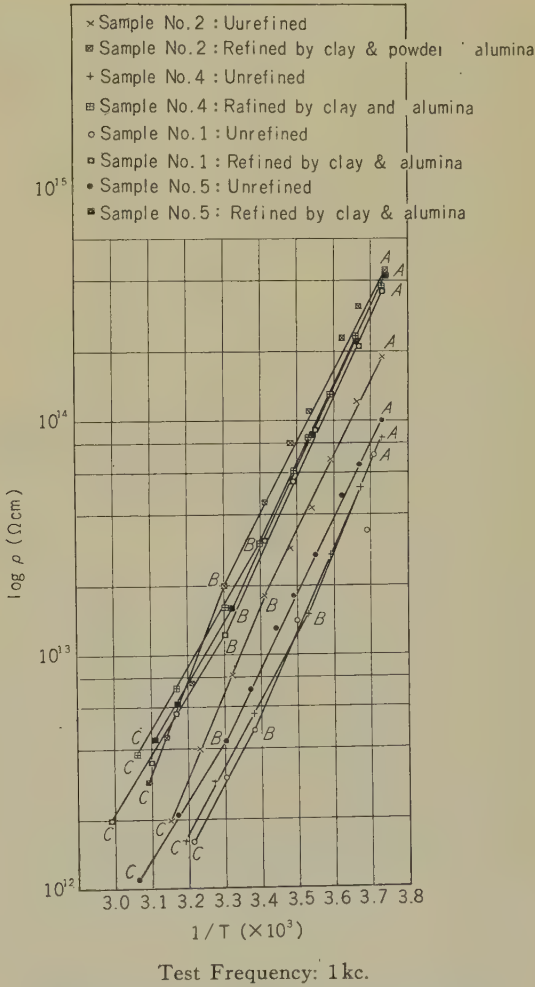


Fig. 18—Relation between resistivity and temperature.

#### 4. Impregnation of Capacitor Paper with Castor Oil

The properties of capacitor paper which had been impregnated with refined castor oil did not deteriorate even when heated to 150° C for three hours under 1–2 mm Hg pressure.

To decrease viscosity and to improve impregnating characteristics, refined castor oil was diluted with  $\text{CCl}_4$  at room temperature. The properties of capacitor paper which was impregnated with this liquid did not deteriorate. The detailed results are shown in Table 4.

#### Discussion

1) When castor oil is refined with active clay only, it obtains good electrical properties, but its acid values increase. Such changes are attributed to the fact that OH compounds are removed and a dehydration reaction of the castor oil takes place. This explanation holds valid particularly from the fact that both the acetyl value and the iodine number decrease.

2) When both active clay and active alumina are used, the refining effect is remarkable. It is thought that the active clay dehydrates, the active alumina absorbs free water; thus, they promote glycerine ester formation in the castor oil and restrain the formation of free fatty acid which might be produced by the active clay at the same time.

The decrease of OH compounds can be recognized also from infrared spectra analysis.

3) The relation between  $\log \rho$  and  $1/T$  is expressed by a refracted straight line, showing a transition point between 20°C and 30° C. This is probably because the molecules of castor oil have hydrogen bonds at temperatures below the transition point. The results are shown in Fig. 18, where  $\rho$  denotes the volume resistivity, and  $T$  signifies the absolute

temperature.

4) The apparent activation energy (or volume resistivity) of refined castor oil, calculated from Arrhenius' equation, is indicated in Table 5. The maximum value is 18,265 cal./mol.

**Table 5**  
ACTIVATION ENERGY OF CASTOR OIL

Sample	Activation Energy (cal./mal.)	
	A-B	B-C
No. 1	Unrefined	16, 218
	Refined	12, 836
No. 2	Unrefined	11, 482
	Refined	15, 712
No. 4	Unrefined	14, 629
	Refined	16, 788
No. 5	Unrefined	14, 880
	Refined	18, 265
No. 5	Unrefined	17, 227
	Refined	13, 076
No. 5	Unrefined	15, 284
	Refined	12, 071
No. 5	Unrefined	14, 535
	Refined	11, 284
No. 5	Unrefined	15, 454
	Refined	12, 424

We must choose castor oil with large activation energy.

#### Conclusion

The best method of refining castor oil studied here can be easily applied to industrial production making use of commonplace materials. Castor oil refined by this method is an excellent capacitor impregnant, and is extremely useful in the manufacture of small highly stable capacitors.

678.742.02 : 621.926

# Degradation of Polyethylene by Mastication\*

Hiroshi NOMURA† and Yuji YAMASHITA†

*The polyethylene hydrocarbon is considered to be ruptured into radical fragments by mastication. In order to investigate the degradation mechanism, Alathon 10 polyethylene is milled with an 8 inch open roll at temperatures of 110°, 140° and 160° C. On the basis of a mechanism which involves the formation and the decomposition of hydroperoxide, the rate formula is derived and supported both by infrared analysis and by viscosity measurements in tetralin at 130° C. For each run, it is shown that  $\ln (1/\bar{P}_t - 1/\bar{P}_0) = kt + A$ , where  $\bar{P}$  is the average degree of polymerization,  $t$  is the mastication time, and  $k$ ,  $A$  constants, respectively. Apparent activation energy corresponding to a change in  $\bar{P}$  is about 1.6 kcal. mol<sup>-1</sup>. The number of chain scissions per molecule increases exponentially with the increase of  $t$ , where as after 3.5 hours of mastication considerable quantities of gel are formed. In regard to the absence of the limiting chain length even after 3 hours of mastication, polyethylene differs from both polyvinyl-chloride and rubber. The degradation may be mainly caused by oxidation, rather than shearing force.*

## Introduction

It is well known that mastication alters the molecular structure of polymers by chemical modification. Although considerable attention has been paid to the effect of this modification on electrical and mechanical properties, comparatively little is known of the chemical processes that take place. An understanding of mechanisms, however, points the way towards using mastication to improve polymer properties.

It is now generally recognized that the long molecular chain is ruptured into radical fragments by mastication. The polymer radicals resulting can undergo mutual combination and interaction with oxygen and other additives. As a result, a process comprising degradation, grafting, or crosslinking may occur.

The main emphasis of this work was directed to a basic study of graft copolymerization of polyethylene with other compounds by mastication; and this work is therefore relevant to the mechanism of chain scission

in the presence of oxygen.

## 1. Experimental

### 1.1. Material

High pressure polyethylene (Alathon 10) was obtained from a commercial source. The preliminary experiments on the material, purified by the xylene-methanol solvent system, showed that the antioxidant in the sample would not affect the results of further experiments.

Tetralin as a solvent for the viscosity measurements was distilled in vacuum, and the boiling point of fraction used was 48°–50°C at 2 mm Hg.

### 1.2. Mastication of Polyethylene

An 8 inch open roll was used. The slower roll rotated at 12 RMS, and the ratio of rotation speeds was 4:5. A flow of constant temperate oil kept the average temperatures of the roll surfaces at 110°, 140° and 160°C. At each temperature, 200 gram samples of polyethylene were milled for different periods of time.

\* MS in Japanese received by the Electrical Communication Laboratory, May. 28, 1960.

† Plastics Application Research Section.



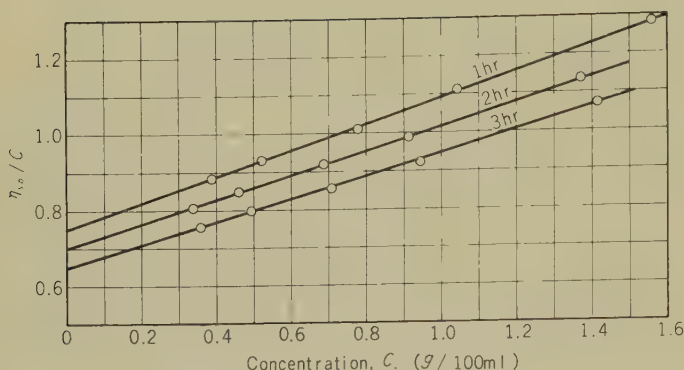


Fig. 1— $\eta_{sp}/C$  vs.  $C$  plot of viscosity data for samples milled at  $140^{\circ}\text{C}$ . Values on lines indicate the length of time of mastication.

### 1.3. Viscosity Measurements

The samples were immersed in tetralin in ampules which were flushed with nitrogen and then sealed. These ampules were shaken occasionally while being kept at  $100^{\circ}\text{C}$  for 24 hours. Then, the solutions were filtered with a sintered glass filter (No. 3). Ubbelohde type viscometers were used to determine the specific viscosity,  $\eta_{sp}$ , of the sample in tetralin at  $130^{\circ}\text{C}$ . Allowance was made for the kinetic energy of flow, which caused an error in the limiting viscosity number,  $[\eta]$ , by 1 per cent. A nitrogen atmosphere was maintained in the viscometer to prevent the oxidation of the polymer solution.

The data was in agreement with the Huggins equation<sup>1)</sup>,

$$\eta_{sp}/C = [\eta] + k' [\eta]^2 C$$

where  $C$  and  $k'$  represent the volume concentration of the polymer and Huggins' constant, respectively.

Typical plots of  $\eta_{sp}/C$  versus  $C$  are shown in Figure 1.

### 1.4. Infrared Absorption Spectrum Measurements

Infrared absorption studies were made using an automatic recording Hitachi Model EPI-2.

### 1.5. Comparative Experiments with Air Oven

In order to examine the effect of oxidative

degradation of polyethylene through mastication in air, specimens of polyethylene in the form of 0.1 mm thick films were heated in an air oven at  $140^{\circ}\text{C}$  for different periods of time. The viscosity and the infrared absorption of these films were also measured by the same methods mentioned above.

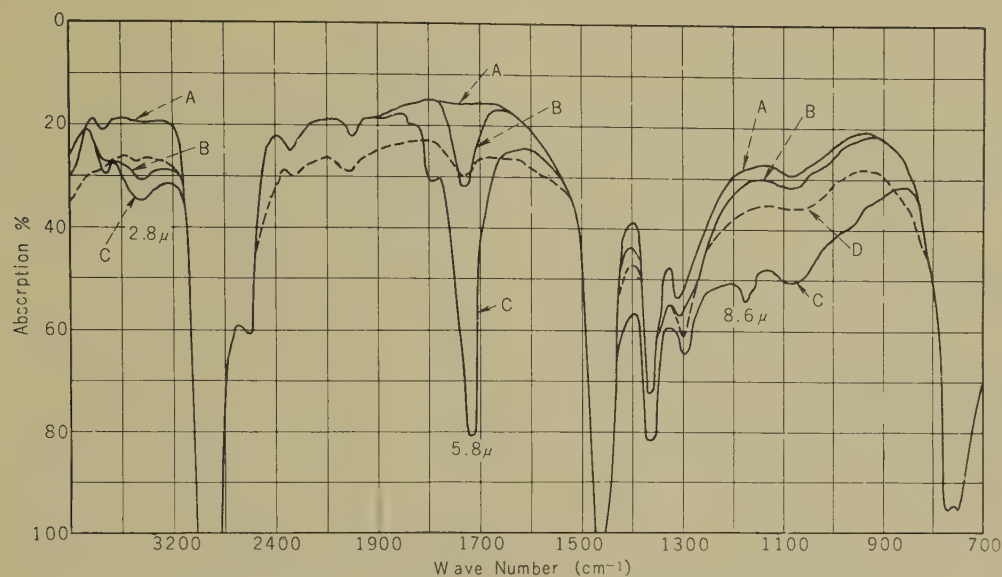
## 2. Results

Experimental results are summarized in Table 1. The value of the limiting viscosity number,  $[\eta]$ , decreases with increase in temperature or with increase in time of mastication.

The values of Huggins' constant,  $k'$  at each temperature did not change greatly with the mastication time, but those at  $160^{\circ}\text{C}$  increased markedly as compared with the value for the original sample. Molecular weight,  $M$ , and degree of polymerization,  $\bar{P}(=M/28)$ , were estimated from  $[\eta]$  of the sample, using the following relationship:<sup>2)</sup>

$$[\eta] = 5.10 \times 10^{-4} \bar{M}_n^{0.725}$$

Infrared absorption spectra are shown in Figure 2, which indicate that the absorptions at  $2.8\mu$  and at  $5.8\mu$ , assigned to the OH bond and the CO bond respectively, increase with the mastication time. From the difference in absorbance at these bonds between milled and unmilled samples at  $140^{\circ}\text{C}$ , the effect of mastication on oxidation may more or less be seen. It may be noticed that in the case of a sample milled for 3 hours at



Sample A: original; B and C: milled for 3 hours at 140° and 160° C respectively; D: heated for 3 hours at 140° C in air oven.

Fig. 2—Effect of mastication on infrared spectrum of polyethylene.

Table 1  
DEGRADATION OF POLYETHYLENE:

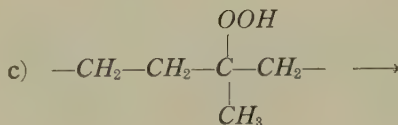
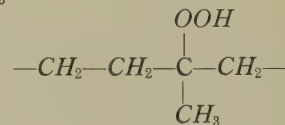
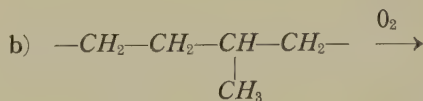
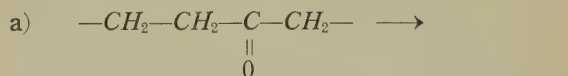
Mastication		[ $\eta$ ]	$k'$	$\overline{P}_t$
Temp. (°C)	Time (hr.)			
—	0	0.89	0.49	1057
	1	0.86	0.49	1000
	2	0.83	0.47	957
	3	0.78	5.50	968
110	1	0.85	0.46	986
	2	0.80	0.49	911
	3	0.74	0.48	818
140	1	0.83	0.77	957
	2	0.75	0.66	836
	3	0.66	0.80	700
160	1	0.85	0.47	986
	2	0.83	0.49	968
	3	0.76	0.48	850
140*	1	0.85	0.47	986
	2	0.83	0.49	968
	3	0.76	0.48	850

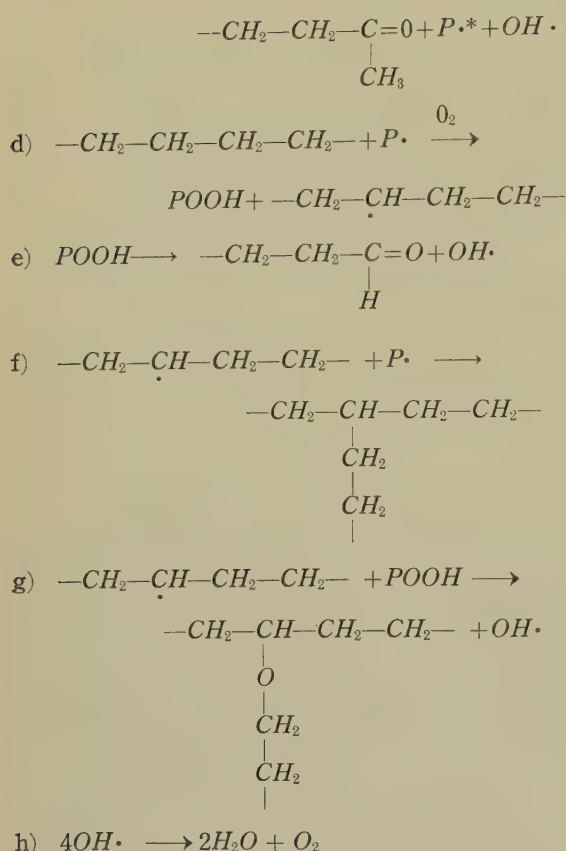
\* This series of samples was obtained from thermal oxidation at 140° C.

160°C, the formation of the COC bond is recognized from the specific absorption at 8.6  $\mu$ .

### 3. Discussion

From the results obtained, the mechanism of reactions which involve the formation and decomposition of hydroperoxide may be considered as follows:





The reactions a) and b) can occur at weak points of the polymer chain; a) is assigned to the chain scission both with shearing force and heat, and b) to the formation of hydroperoxide by thermal oxidation. The reaction c) corresponds to the decomposition of hydroperoxide into polymer radical,  $P\cdot$ , and other fragments. It was confirmed with infrared absorption spectra that intermediate and final fragments with OH or CO bonds were produced other than in the positions of these characteristic bonds in the polymer chain. In this sort of reaction, it is well known that water vapor is generated as is shown in reaction h). After a considerable time of mastication, branching and crosslinking reactions predominate, and then cause a gelation of the polymer chain, as shown in reactions (f and g). As a matter of fact, the sample milled for 3.5 hours at 160°C contained a considerable quantity of a fraction insoluble in

\*  $P\cdot$ : Represents a polymer radical,  $\text{--CH}_2\text{--CH}_2\cdot$ .

tetralin at 130°C, and was eliminated in further experiments, since the reaction can not be followed by viscosity measurement. From the fact that in the case of a sample milled at 160°C, Huggins' constant,  $k'$ , has a high value and the existence of the COC bond as shown in reaction g) is confirmed from the infrared absorption spectrum, these branching reactions may be expected for the gelation mechanism.

The process of main-chain scission was followed by determining the change in degree of polymerization,  $\bar{P}$ , with increase in the time of mastication. When the total number of bonds between the ethylene units in given system,  $L$ , changes from  $L_0$  to  $L_t$  after  $t$  hours of mastication, it may be assumed that the following relationship is maintained through reactions a) and c), comprising the degradation process:

$$-\frac{dL_t}{dt} = S_t L_t \quad (1)$$

where  $S_t$  denotes the number of scissions per molecule per hour. Integrating equation (1), it follows that

$$\ln L_t - \ln L_0 = - \int_0^t S_t dt. \quad (2)$$

The left hand side of this equation can be transformed, in agreement with Tobolsky<sup>(3)</sup> and Smets<sup>(4)</sup> work, by substituting and expanding the logarithms (See Appendix):

$$\ln L_t - \ln L_0 = \frac{1}{\bar{P}_t} - \frac{1}{\bar{P}_0} \quad (3)$$

where  $\bar{P}_0$  and  $\bar{P}_t$  are, respectively, the degree of polymerization at the beginning of the reaction ( $t_0$ ) and the degree of polymerization at the moment ( $t$ ).

If  $S_t$  varies exponentially with  $t$ ,

$$S_t = S_0 \exp kt \quad (4)$$

where  $S_0$  and  $k$  are constants. Combining equations (2), (3), and (4),

$$\ln \left( \frac{1}{\bar{P}_t} - \frac{1}{\bar{P}_0} \right) = kt + \ln \left( \frac{S_0}{k} \right). \quad (5)$$

If the above assumptions are valid, then the rate constant,  $k$ , can be evaluated graphically by plotting  $\log (1/\bar{P}_t - 1/\bar{P}_0)$  versus  $t$ . The results obtained for milled polyethylene at different temperatures are consistent with a linear relationship within the experimental error, as shown in Fig. 3.

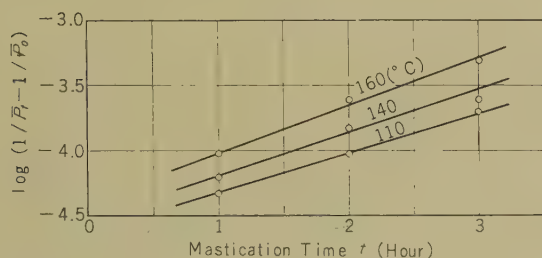


**Fig. 3**—Relationship between degree of polymerization and mastication time. Values on the curves indicate mastication temperature.

From the slope of these lines the values of  $k$  at different temperatures are found and recorded in the second column of Table 3.

In order to confirm again the assumption of the exponential dependence of  $S_t$  on mastication time  $t$ , the values of  $S_t$  were calculated directly, using the ratio of the limiting viscosity number for the original material to that for the milled sample,  $[\eta]_0 / [\eta]_t$ .

Matsumoto<sup>5b</sup> has shown that the number of chain scissions varies approximately with the limiting viscosity number according to the following relation,

$$S_t = 2 \left( \frac{[\eta]_0}{[\eta]_t} - 1 \right); \quad (6)$$

and the relation is independent of the molecular weight distribution and the molecular weight-viscosity relationship of the material. The values of  $S_t$  calculated from the  $[\eta]$  values in Table 1 are shown in Table 2, and then according to Eq. (4) the values of  $\log S_t$  are plotted against  $t$  in Fig. 4. The corresponding  $k$  values are given in the third column of Table 3.

In spite of the assumptions and approximations mentioned above, there is a remarkable

**Table 2**

NUMBER OF SCISSIONS PER MOLECULE PER HOUR,  $S_t$ ,\* BY MASTICATION

Temp. (°C)	Time (hours)		
	1	2	3
110	0.07	0.14	0.28
140	0.09	0.22	0.40
160	0.14	0.37	0.70

\*  $S_t$ : Calculated from viscosity data, using the relation,<sup>(5)</sup>  $S_t = 2\{([\eta]_0/[\eta]_t) - 1\}$ .

**Table 3**

DEGRADATION RATE CONSTANTS

Mastication Temp. (°C)	$k \times 10^{-1}$ (mol. <sup>-1</sup> /hour <sup>-1</sup> )	
	from Fig. 3	from Fig. 4
110	6.90	6.76
140	7.91	7.96
160	8.83	8.46

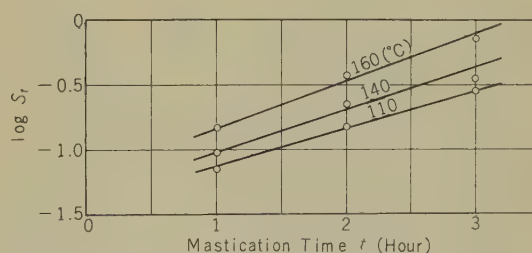


**Fig. 4**—Relationship between number of scissions and mastication time. Values on the curves indicate mastication temperature.

agreement between the two series of  $k$  values.

Consequently, it may be concluded that the number of chain scissions increases exponentially as time increases under the present conditions of mastication. On the other hand, it has been reported that neither natural rubber<sup>(6)</sup> nor polyvinylchloride<sup>(7)</sup> degrades be-



low a certain degree of polymerization, that is, below the so-called limiting chain length.

This phenomenon is considered to be caused by two factors: first, a shortened polymer chain will no longer be destroyed by constant shearing force; and second, as time goes on, radical fragments will tend to combine with each other again. In the case of polyethylene, the possibility must be admitted that molecular breakdown at the temperatures used mainly result from oxidative degradation rather than from the shearing force. This possibility may also be deduced from the fact that the extent of degradation increases as the temperature of mastication increases, whereas it is expected that, in general, a smaller shear would be encountered at higher temperature because of the decreased polymer viscosity.

There is another matter to be noted as to the activation energy of reaction. A plot of  $\log k$  versus the reciprocal of the absolute temperature is shown in Fig 5. There appears to be a linear dependence of  $\log k$  on  $1/T^\circ\text{K}$ . The slope of the line, following the Arrhenius equation, gives an apparent activation energy of about  $1.6 \text{ kcal}\cdot\text{mol}^{-1}$ . This value is considerably smaller than either the value of  $21 \text{ kcal}\cdot\text{mol}^{-1}$  for the simple thermal oxidation of polyethylene<sup>(8)</sup> or that of  $11 \text{ kcal}\cdot\text{mol}^{-1}$  for chain rupture by capillary flow of molten polyethylene in the absence of oxygen<sup>(9)</sup>. The present values does not comprise the parts for diffusion of oxygen and for actual oxidation, and, therefore, seems to be based on a change in degree of polymerization caused by oxidative degradation.

In order to explain the net effect of shear-

ing force on chain scission, further experiments on mastication in inactive atmospheres will be necessary.

### Conclusion

The degree of polymerization of polyethylene decreases with mastication in air with:

- a) increase in temperature
- b) increase in time

Therefore, there is no limiting chain length under the present conditions of mastication.

The number of chain scissions per molecule increases exponentially with increase in time, and therefore, the rate of degradation is represented by the following relationship,

$$\ln\left(\frac{1}{P_t} - \frac{1}{P_0}\right) = kt + A$$

where  $P_0$  and  $P_t$  are, respectively the degree of polymerization at the beginning of the reaction and at the moment  $t$ ; and  $k$  and  $A$  are constants. Apparent activation energy corresponding to the change in  $P$  is about  $1.6 \text{ kcal}\cdot\text{mol}^{-1}$ . The degradation here seems to be caused by oxidation rather than by shearing force.

### Appendix

Where the number of the polymer comprising  $P$  ethylene units changes from  $[P_0]$  to  $[P_t]$  after  $t$  hours; assuming  $N$  to be the total number of ethylene unit in given system, the ratio of the corresponding number of link,  $L_0/L_t$ , is given by the following equation,

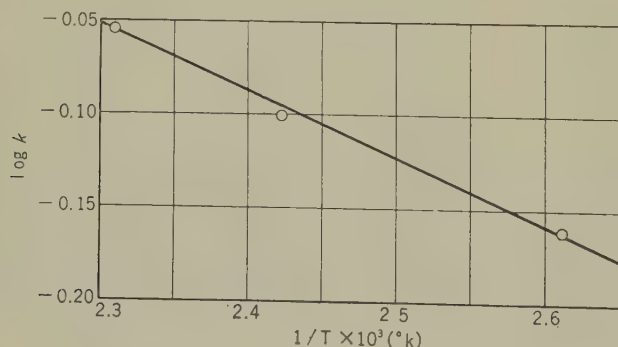


Fig. 5—Temperature dependence of degradation rate constants.  $k$  values, obtained from Eq. (5) and Fig. 3.

$$\frac{L_0}{L_t} = (N - [\bar{P}_0]) / (N - [\bar{P}_t]) = \frac{\left(1 - \frac{[\bar{P}_0]}{N}\right)}{\left(1 - \frac{[\bar{P}_t]}{N}\right)} \quad (\text{App. 1})$$

From the definition of number average degree of polymerization,  $\bar{P} = N/[\bar{P}]$ , it can be seen that

$$\frac{L_0}{L_t} = \frac{\left(1 - \frac{1}{\bar{P}_0}\right)}{\left(1 - \frac{1}{\bar{P}_t}\right)} \quad (\text{App. 2})$$

By substituting Eq. (App. 2) into the left hand side of Eq. (2), expanding the logarithms with respect to  $1/\bar{P}$ , and neglecting all terms except the first term, we can write

$$\ln L_t - \ln L_0 = -\frac{1}{\bar{P}_t} + \frac{1}{\bar{P}_0}$$

#### References

- (1) M. L. Huggins, *J. Am. Chem. Soc.*, **64**, p. 2761 (1942).
- (2) L. H. Tung, *J. Polymer Sci.*, **20**, p. 495 (1956).
- (3) Mark and Tobolsky, *Physical Chemistry of High Polymeric Systems*, p. 462 (1950), Interscience, New York-London.
- (4) G. Tasset and G. Smets, *J. Polymer Sci.*, **12**, p. 517 (1954).
- (5) M. Matsumoto, *Chem. High Polym.*, **6**, p. 77 (1949), (in Japanese).
- (6) D. J. Angier and W. F. Watson, *J. Polymer Sci.*, **20**, p. 235 (1956).
- (7) K. Goto et. al., *Chem. High Polym.*, **10**, p. 263 (1953), **10**, p. 459 (1953), (in Japanese).
- (8) S. Kawamatsu, *ibid*, **16**, p. 353 (1959).
- (9) H. A. Pohl and J. K. Lund, *SPE Journal*, **15**, p. 390 (1959).

\* \* \* \*

# Papers Contributed to Scientific and Technical Journals by the Members of the Laboratory\*

## Papers Published in Other Publications of the Electrical Communication Laboratory

U.D.C. 534.1:621

The Analysis of Frame Vibrating Systems

*Motonobu YONEKAWA*

Kenkyû Zituyôka Hôkoku (Electr. Comm. Labor. Techn. Journ.), NTT, **9**, 6, p. 635-680, 1960

The free and forced vibration problems of a portal frame composed of uniform beams are analyzed by making use of both the stiffness matrix of beams and electrical network analogies.

U.D.C. 534.13.539.4

621.395.623.34

Stresses and Deformations on Conical Vibrating Plate

*Kazuo IKEGAYA*

Kenkyû Zituyôka Hôkoku (Electr. Comm. Labor. Techn. Journ.), NTT, **9**, 6, p. 681-689, 1960

Stress on and the resulting deformation of conical vibrating plates caused by an axial force are analyzed. Various aspects, including the magnitudes, of the stress and deformation concentrations at the inner and outer edges are discussed.

U.D.C. 546.289:620.197.2]:539

An Investigation of Surface Treatment of Single-Crystal Germanium

*Kazumasa ONO and Katuhisa FURUSHO*

Kenkyû Zituyôka Hôkoku (Electr. Comm. Labor. Techn. Journ.), NTT, **9**, 6, p. 691-698, 1960

Surface oxidation of single-crystal germanium by mixtures of HF and HO was investigated. Oriented GO films are obtained by treatment with the vapor of the mixtures.

U.D.C. 621.315.619

Laminate base materials for Communication Equipment Use

*Masaaki KATAGIRI*

Kenkyû Zituyôka Hôkoku (Electr. Comm. Labor. Techn. Journ.), NTT, **9**, 5, p. 571-584, 1960

Development of new papers for laminates which are made from cotton flock and flax having large crystalline regions and a high degree of polymerization in the cellulose is described.

---

\* Reprints may be available upon request to the author.

U.D.C. 621.372.832.6.029.65

48 Gc Center-Excited Type Hybrid

*Shin-ichi IIGUCHI*

Kenkyû Zituyôka Hôkoku (Electr. Comm. Labor. Techn. Journ.), NTT, **9**, 5, p. 565-570, 1960

A new type of hybrid for use as a component of a band separation filter for circular  $TE_{11}$  waves has been devised. This hybrid has been designed theoretically and investigated experimentally. The conversion loss is less than 1 dB.

U.D.C. 621.374:621.375.3

Core matrix driver Employing Amplifiers

*Zunzi YAMATO and Yasunobu SUZUKI*

Kenkyû Zituyôka Hôkoku (Electr. Comm. Labor. Techn. Journ.), NTT, **9**, 5, p. 537-564, 1961

A high frequency magnetic amplifier with high efficiency, high  $S/N$ , and high output power was designed to derive a large scale memory matrix in a parametron device.

U.D.C. 621.385.635

Matching between Traveling-Wave Tube Helix and Waveguide

*Tomoyuki UNOTORO*

Kenkyû Zituyôka Hôkoku (Electr. Comm. Labor. Techn. Journ.), NTT, **9**, 6, p. 639-648, 1960

Matching circuit between helix and waveguide has been investigated by a statistical analysis of the orthogonal array layout of experiments. Relations between impedance of the circuit and dimensions of this structure have also been observed. The final design has 20% bandwidth at 11 kMc.

U.D.C. 621.385.64.001

On the Energy Build-up in Magnetrons

*Daijiro KOBAYASHI*

Kenkyû Zituyôka Hôkoku (Electr. Comm. Labor. Techn. Journ.), NTT, **9**, 5, p. 649-652, 1960

The previously published "A new analysis of magnetrons" has been extended to the energy build-up in magnetrons. The variation of PPM noise of magnetrons as a function of load conditions is made clear by the use of this theory.

U.D.C. 621.395.623.001

The Design of a New Telephone Receiver

*Kenro MASUZAWA and Kiyoshi TAJIMA*

Kenkyû Zituyôka Hôkoku (Electr. Comm. Labor. Techn. Journ.), NTT, **9**, 5, p. 447-474, 1960

Design expressions for the response of a telephone receiver were formulated, many interesting characteristics in practical structures were experimentally obtained, and the results obtained were applied to the design of a new telephone receiver.

U.D.C. 621.395.636.1-56.001.4

Design of a Governor for Telephone Dials

*Tetsuo KUDO*

Kenkyû Zituyôka Hôkoku (Electr. Comm. Labor. Techn. Journ.), NTT, **9**, 5, p. 497-536, 1960

A method of designing telephone-dial fly-bar type governors which have good regulation and long life is discussed. Determination of the position of the friction piece is very important.



U.D.C. 621.359.66 : 621.314.21 : 538.551

Telephone Circuit Employing a 3-Core Transformer

*Hiroyasu MIURA*

Kenkyû Zituyôka Hôkoku (Electr. Comm. Labor. Techn. Journ.), NTT, **9**, 5, p. 475-495, 1960

A telephone circuit using a 3-core transformer which combines the merits of a bridge and those of a booster is described.

U.D.C. 621.397.8.001.5

Dielectric-Coated Waveguide Fabrication and Characteristics

*Ken-ichi NODA* and *Kazuo YAMAGUCHI*

Kenkyû Zituyôka Hôkoku (Electr. Comm. Labor. Techn. Journ.), NTT, **9**, 6 p. 621-638, 1960

Several methods of fabricating dielectric-coated waveguide are considered, and the characteristics obtained are theoretically and experimentally investigated. A low loss bond results when polyethylene tube is bonded to the inner surface of a waveguide.

**Papers Published in Publications of Scientific and Technical Societies**

U.D.C. 261.395.34.004.5.001.2

A Theory of Maintenance of Automatic Telephone Exchanges

*Toshimichi AMANO*

Journ. Inst. Electr. Comm. Engr. Jap., **43**, 6, p. 685-691, June 1960

In this paper, a general method of evaluating the effect of faults in automatic exchanges is presented and probability of calls encountering faults is calculated.

U.D.C. 537.312.6-72 : 546.682'86

The Change in Electron Mobility in Indium Antimonide at Low Electric Field

*Yasuo KANAI*

Journ. Phys. Soc. Jap., **15**, 5, p. 830-835, May 1960

The change in electron mobility in indium antimonide at low electric field was measured by the bridge method at 77, 201, and 297° K. The effect of transverse magnetic field upon the change in electron mobility was also measured.

U.D.C. 537.56 : 537.52

Non-linear Effects on Electron-Plasma Oscillations

*Masao SUMI*

Journ. Phys. Soc. Jap., **15**, 6, p. 1086-1093, June 1960

Non-linear effects in the excitation of electron-plasma oscillations are investigated by considering a non-linear term in the Boltzmann equation as a perturbation. Behaviors of higher harmonics and the saturation limit are discussed.

U.D.C. 621.375.9 : 621.372.632

Lower Side Band Frequency Converter Type Parametric Amplifier

*Tōru OKAJIMA and Manyang CHUNG*

Journ. Inst. Electr. Comm. Engr. Jap., **43**, 6, p. 691-694, June 1960

Results of experiments on a lower side band frequency converter type parametric amplifier are described. The input frequency is 900 Mc/s. the output frequency (the so-called idling frequency) is 6000 Mc/s, and the pump frequency is 6900 Mc/s. The characteristics of the amplifier are:

- ① the noise figure is 1.5 to 2.1 dB, ② the amplification gain is 14 dB for 15 Mc bandwidth (1 dB down).

U.D.C. 621.396.62 : 621.391.883.22

New Method of Measuring the Noise Figure of the First Stage of a Receiver

*Tōru OKAJIMA*

Journ. Inst. Electr. Engr. Soc. Jap., **43**, 6, p. 695-698, June 1960

A new method to accurately estimate the value of the first stage noise figure in the over-all receiver noise figure is proposed.

An equivalent circuit to show the principle of this measuring method is illustrated. Y-factor is proportional to the ratio of the output noise power at the switch positions.

U.D.C. 678.742.012 : 536.41.08 + 541.64

Re-appreciation of the Second Order Transition Phenomena in Polyethylene

*Ryuichi NAKANE*

Journ. Phys. Soc. Jap., **15**, 6 p. 1040-1048, 1960

Among the phenomena which were hitherto treated as the second order transition of polyethylene there exist at least two different phenomena; the end point of the crystallinity change at  $-30^{\circ}\text{C}$ , and the true second order transition at  $-55^{\circ}\text{C}$ .

\* \* \* \*









## CONTENTS

Analysis of Polar Relay .....	297
<i>Yasuo Tomita</i>	
Dielectric-Coated Waveguide Construction and Characteristics .....	309
<i>Ken'ichi NODA and Kazuo YAMAGUCHI</i>	
Mode Conversion in the Excitation of $TE_{01}$ Waves in a $TE_{01}$ Mode Transducer (Rectangular→Sector Portion→Circular).....	324
<i>Shin'ichi IIGUCHI</i>	
Magnetic Gate Circuits Controlled by High Frequency Signals.....	335
<i>Ichiro ENDO and Kikunobu KUSUNOKI</i>	
Distributed Amplifier Tube .....	343
<i>Takuya KOJIMA</i>	
The Magnetic Circuit of Telephone Receiver.....	369
<i>Ryozo ARAI and Tatsuo SHIMAMURA</i>	
Refining of Castor Oil for Capacitor Dielectrics.....	376
<i>Masaaki KATAGIRI and Katunari KODATI</i>	
Degradation of Polyethylene by Mastication .....	385
<i>Hiroshi NOMURA and Yuji YAMASHITA</i>	
Papers Contributed to Scientific and Technical Journals by the Members of the Laboratory .....	392